STM IMAGING OF STRONG ORBITAL-SELECTIVE CORRELATIONS IN FeSe

A Dissertation

Presented to the Faculty of the Graduate School

of Cornell University

in Partial Fulfillment of the Requirements for the Degree of

Doctor of Philosophy

by

Andrey Kostin

May 2018

© 2018 Andrey Kostin
ALL RIGHTS RESERVED

STM IMAGING OF STRONG ORBITAL-SELECTIVE CORRELATIONS IN FeSe

Andrey Kostin, Ph.D.

Cornell University 2018

High temperature superconductivity is typically found in the vicinity of a magnetically ordered phase. The parent state of iron-based superconductors is most often a collinear antiferromagnet that breaks the tetragonal symmetry of the high temperature phase. Such a magnetically ordered state is accompanied by an orthorhombic lattice distortion and the nematic ordering of electronic degrees of freedom. Intriguingly, FeSe is an iron-based superconductor that realizes nematic ordering in the absence of any long range magnetic order. A recent scanning tunneling microscopy (STM) experiment deduced the superconducting gap structure of FeSe [1] suggesting that in this material orbital selectivity plays a significant role in superconducting pairing. Within a multi-orbital Hubbard model for iron-based superconductors, such orbital selectivity is expected and driven by a sizable Hund's coupling. In this thesis, I use STM to visualize quasiparticle interference patterns in the unusual nematic state of FeSe. The analysis of these patterns demonstrates that the quasi-particle weight is significantly larger for the d_{yz} orbitals than for the d_{xz} and d_{xy} orbitals. This establishes the existence of strong orbital-selective correlations in FeSe. Additionally, I identify significant directionality in the atomic structure of local density of states images in FeSe at low temperature. This is a novel method for visualizing nematicity in iron-based superconductors.

BIOGRAPHICAL SKETCH

Andrey Kostin was born in the Russian city of Tomsk. Tomsk, known as the educational center of Siberia with no less than 6 state universities. After spending his early childhood there, Andrey moved to the beautiful Siberian city of Barnaul to begin his education in a local elementary school. His early interests while attending primary school included art, mathematics and the Russian language, but mathematics soon materialized as his prime passion. He continued to cultivate his love of problem-solving throughout elementary school in Tomsk and the nearby Siberian city of Barnaul before circumstances transported him rather suddenly from Russia to Canada at the age of twelve.

There Andrey lived in the beautiful city of Vancouver on the Pacific coast of Canada and attended local high school. When he was not contemplating the many unsolved mysteries of mathematics and natural sciences, Andrey's primary non-academic interest was chess in which he achieved the rank of expert. It is a passion that he continues to pursue to this day.

Upon graduating high school, Andrey was admitted to the Applied Science Faculty of the University of British Columbia to study engineering. After the first year of general engineering studies, he chose to major in Engineering Physics (Electrical Engineering option) with a minor in Honors Mathematics. The degree work - consisting of mostly a mixture of physics, math and electrical engineering courses - suited Andrey's academic interests well. The five year degree also included sixteen months of work experience. Andrey characterized sensors for neutrino detectors at TRIUMF (Canadian cyclotron facility), worked on applying modern control theory to the design of next generation particle accelerators at the UBC physics department, and developed image processing algorithms for high dynamic range content at Dolby Canada.

Invigorated by his studies thus far, Andrey decided to continue his higher education by entering the PhD program in physics at Cornell, where he joined professor J.C. Séamus Davis' lab to study experimental hard condensed matter physics. There he used two of the best low temperature Scanning Tunneling Microscopes in the world to investigate cuprate and iron-based superconductors.

I dedidate my thesis to my parents and grandmother whose support really helped me during my studies.

ACKNOWLEDGEMENTS

There are many people that helped me tremendously in my studies at Cornell. First and foremost, I would like to acknowledge my advisor Séamus Davis. He has a unique perspective on solid state physics coming from his ^{3}He background. I would describe him as a visionary whose current interests primarily lie in the most fundamental open questions in superconductivity. It is always great fun to debate with him in the research process.

Next, I have to acknowledge my best friend Peter Sprau. I first met Peter in the fall of 2012 when we worked as teaching assistants for the same class. He made an impression on me of a very reliable and honest person. We quickly became friends and remained very close throughout my PhD. In January of 2015, I started to work with Peter on STM projects. The collaboration proved to be very fruitful and enjoyable for me. Peter is a great experimentalist, and his experience really helped me finish my thesis work.

Another close friend that deserves special mention is Stephen Edkins. Steve joined the Davis lab in the fall of 2013, and I worked closely with him for just over a year. I was always envious of his encyclopedic knowledge of condensed matter physics that he acquired during his studies at Cambridge University and the University of Saint Andrews. Steve was one of the smartest peers I met at Cornell, and our collaboration pushed me to be better. Additionally, he was my roommate for almost 4 years during my stay in Ithaca, and I consider him a very close friend that helped me get through the tough parts of my graduate studies.

I would like to acknowledge my newest collaborator in the Davis lab, Yi Xue Chong. His enthusiasm is infectious, and this makes working with him very enjoyable. He is a very capable young experimentalist who is very good at solving puzzles. I wish him the best of luck in the rest of scientific career.

Over the years I have benefited from interacting with many other researchers in the Davis group. Here I mention Mohammad Hamidian, Inés Firmo, Freek Massee, Ethan Kassner, Rahul Sharma, Azar Eyvazov and Ritika Dusad. Mohammad Hamidian, in particular, was my first teacher of STM and cryogenic techniques.

As an experimentalist, I found over the years that collaborations with the theory colleagues were essential for producing high quality physics papers. Theoretical ideas from Brian Andersen, Peter Hirschfeld, and Andreas Kreisel were widely used in this thesis. Particularly I would like to thank Andreas Kriesel for his patience while explaining physics concepts to me over Skype.

I would like to acknowledge the Cornell physics faculty. I particularly enjoyed attending lectures given by Paul McEuen, Veit Elser and Eun-Ah Kim.

Finally, I want to thank my family and all my friends for their support throughout my PhD. I would not have been able to do this all by myself.

TABLE OF CONTENTS

LIST OF ABBREVIATIONS

FeSC := Iron-based Superconductor
STM := Scanning Tunneling Microscope / Microscopy
SDW := Spin Density Wave
SI-STM := Spectroscopic Imaging - Scanning Tunneling Microscope
RVB := Resonating Valence Bond Theory
CAFM := Collinear Antiferromagnetism
FT := Fourier Transform
DOS := Density of States
LDOS := Local Density of States
JDOS := Joint Density of States
IDOS := Energy Integrated Density of States
BQPI := Bogoliubov Quasiparticle Interference
ARPES := Angle-Resolved Photoemission Spectroscopy
INS := Inelastic Neutron Scattering
QO := Quantum Oscillations
CEC := Constant-Energy-Contour
BZ := Brillouin Zone
NMR := Nuclear Magnetic Resonance
FOV := Field of View
LF := Lawler-Fujita

LIST OF FIGURES

CHAPTER 1

INTRODUCTION

One of the most fundamental questions in the field of iron-based superconductors (FeSCs) is whether the conduction electrons in these materials are strongly or weakly correlated [2]. This question is intimately connected with the problem of identifying the pairing mechanism producing superconductivity in these systems.

The weak correlation perspective emphasizes that the parent state of FeSCs is a metal and thus falls under the purview of Fermi liquid theory [3]. At low temperatures, in the presence of any attractive interaction, a Fermi liquid state becomes unstable, and electrons near Fermi surface form pairs and condense into a superconducting state. The effective interaction is mediated by an exchange of collective bosonic excitations. In FeSCs, the relevant excitations are generally thought to be spin fluctuations described by the itinerant theory of magnetism [4]. In particular, due to an approximate nesting of the hole and electron pockets, the spectrum of the spin fluctuations is peaked at the wavevector consistent with the observed collinear antiferromagnetic order (CAFM).

Alternatively, bad metal behavior of the parent state of FeSCs is considered to be an indication that it is proximate to a Mott insulator state. This would imply that FeSCs are in the strongly correlated regime. Most popular mechanism for the emergence of superconductivity in a strongly correlated system in the vicinity of a antiferromagnetic Mott phase is the resonating valence bond (RVB) theory [5]. In RVB theory it is proposed that the ground state of the parent Mott insulator is a charge incompressible spin liquid of neutral singlet pairs with a finite (Mott Hubbard) gap for charge excitations [6]. Upon doping, these

pairs acquire charge, and the system transforms from an insulator into a superconductor. Unlike in the itinerant theory, the magnetism is assumed to be local in nature, and the antiferromagnetic superexchange between the neighboring spins is the pairing glue. Although this mechanism should be most appropriate for copper-based superconductors (cuprates) where electron correlations are undoubtably strong, it is also discussed in context of FeSCs [7] where the starting point is a multiband t-J_1-J_2 model [8]. In this model the magnetism is described by the nearest neighbor (NN) J_1 and next nearest neighbor (NNN) J_2 antiferromagnetic interactions (mediated by ligand ions) between the local moments on Fe ions. In FeSCs, the CAFM order implies that the NNN interaction is dominant and drives pairing.

The remaining possibility is that FeSCs reside in the intermediate regime between the strong and weak coupling. The multi-orbital nature of these materials allows for orbital-selective physics and, in particular, the coexistence of itinerant electrons and localized moments as separate degrees of freedom [3]. The hybrid theory of superconductivity emphasizes this coexistence of weakly correlated Fermi liquid and Mott state of local moments and postulates that itinerant electrons pair by exchanging the collective magnon mode of the local moments.

Interestingly, both weak coupling [9] and strong coupling [10] approaches predict the same s± structure for the superconducting order parameter in FeSCs consistent with many experiments [11]. This implies that purely determining the superconducting order parameter symmetry experimentally is not enough to identify the relevant relevant theory of superconductivity. This is where the experiments capable of identifying the nature and strength of electron correlations in FeSCs would be valuable. This thesis discusses how scanning tunneling

microscopy (STM) measurements can provide such information.

The following introductory chapter is split into three parts. Firstly I give a very brief overview of iron-based superconductors. Then I proceed to discuss properties of electronic correlations in the parent state of iron-based superconductors. Lastly, I focus on a notable member of FeSC family, FeSe, and review its most intriguing features to motivate the studies presented in this thesis.

1.1 Iron-based superconductors

In 2006 the group of Hideo Hosono reported superconductivity in iron-based layered material LaFePO [12]. Later in 2008 the same group made a major breakthrough by synthesizing $LaO_{1-x}F_xFeAs$ with a superconducting transition temperature T_c = 26 K [13]. Subsequently many more iron-based superconductors (FeSCs) with high T_c were discovered, and a new family of high temperature superconductors was born. Except for a handful of exceptions (MgB_2 and some A15 superconductors), until then high transition temperatures were restricted to the cuprates. Despite substantial progress in the study of cuprates, the field of high temperature superconductivity still had many fundamental questions without universally accepted answers. Comparative study of the two different families of high T_c superconductors held a promise of elucidating systemic features that are essential for high transition temperatures [14].

There are a number of crystal structures that are known to support iron-based superconductivity, the most common of which are shown in Fig. 1.1. All of these structures share fundamental FeX trilayer (where X designates a pnictogen (As/P) or chalcogen (S/Se/Te) atom), and they are classified by their

stoichiometry. For example, FeSe, NaFeAs, $BaFe_2As_2$, and LaOFeAs belong '11', '111', '122', and '1111' families respectively.

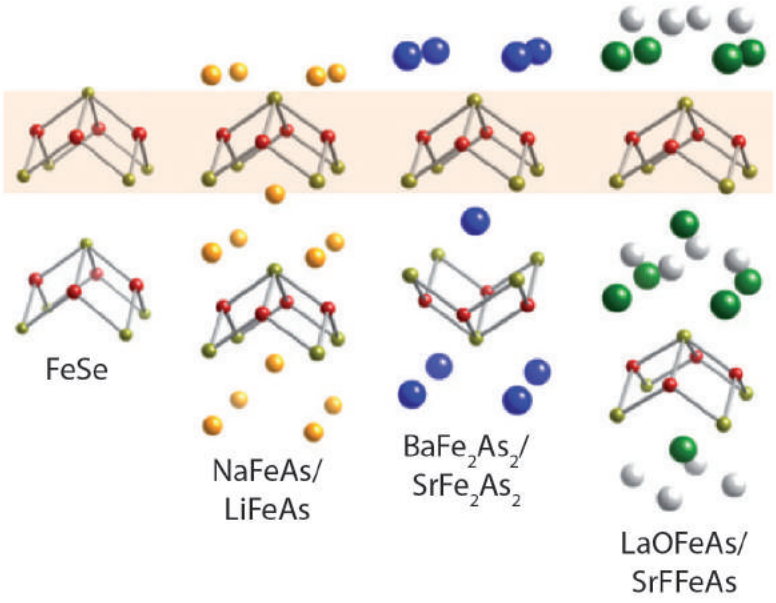

Figure 1.1: Families of iron-based superconductors. Crystal structures of four common families of FeSC are shown. Shaded stripe marks FeX trilayer. Adapted from [15].

In conventional superconductors, where electron pairing is phonon mediated, superconductivity and magnetism are considered to be antithetical forms of order [14, 16]. With the discovery of 'exotic' superconductivity in close proximity to magnetically ordered phases, this view has shifted. For example, the parent state of cuprate superconductors is a Néel antiferromagnet where the spins on adjacent Cu atoms are aligned antiparallel to each other. The superconductivity emerges from doping this antiferromagnetic state with either holes or electrons. Likewise, neutron diffraction measurements on FeSCs have identified magnetically ordered states. The most common parent state, found in the majority of '111', '122' and '1111' materials [17], is a spin stripe ordering where spins are ferromagnetically arranged along one direction and antiferromagnet-

ically along the other (Fig. 1.2). The typical values for the ordered moment for iron spins are in the range $0.80 - 0.94\mu_B$ for the '122' family and $0.25 - 0.80\mu_B$ for the '1111' family [17]. Among the '111' family, the ordered moment is much smaller ($0.09\mu_B$) in NaFeAs and there is no magnetic ordering in LiFeAs.

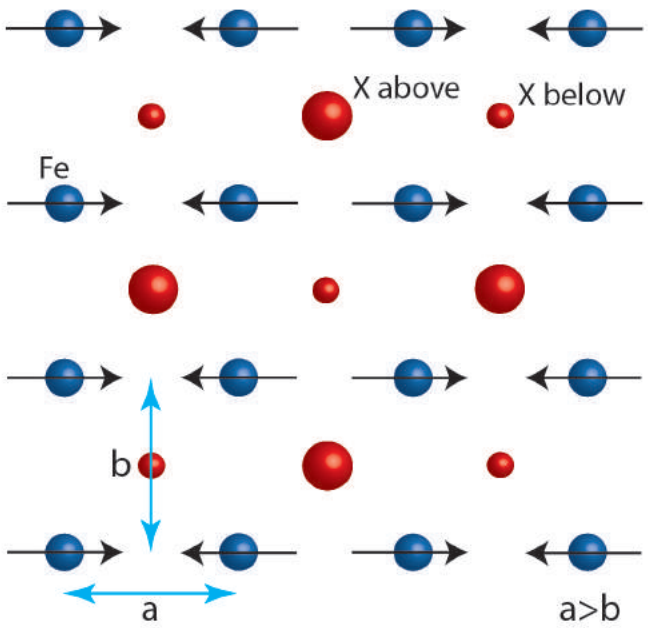

Figure 1.2: Common collinear spin arrangement in the parent compounds of FeSC. FeX tri-layer shows the spin configuration for the most common SDW state of FeSCs. The spins are aligned along the longer orthorhombic axis [18]. The orthorhombic distortion is small, and $\frac{a-b}{a+b}$ is on order of 10^{-3}.

The corresponding generic phase diagram (Fig. 1.3) shows the interplay for magnetism and superconductivity [14]. Upon cooling, the undoped parent compound undergoes a tetragonal to orthorhombic structural transition. Since the measured anisotropies in electronic properties are much larger than the anisotropy of the lattice parameters, it is believed that this transition is driven by electronic rather than lattice degrees of freedom [19]. Since the time reversal symmetry is preserved and the rotational symmetry is broken, this state is called *nematic* in analogy to the terminology used for liquid crystals. Upon further

cooling, the mentioned magnetically ordered phase - termed *spin density wave* (SDW) - is stabilized. Superconductivity emerges from the SDW state with sufficient charge doping.

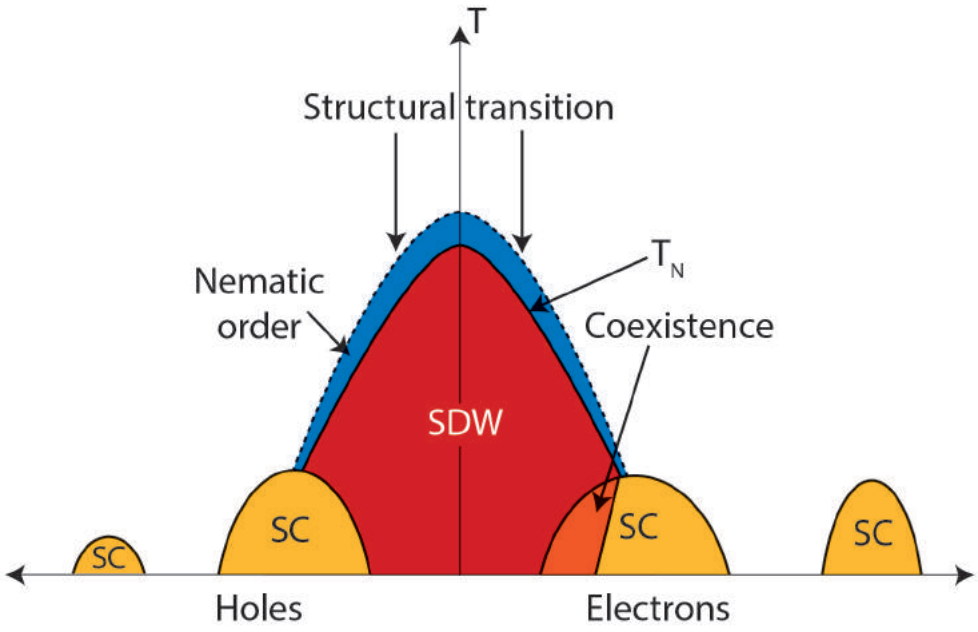

Figure 1.3: Generic phase diagram of FeSC. Reproduced from [14].

Understanding the superconducting state in FeSCs requires examination of the associated electronic structure. Fig. 1.4B shows a typical two dimensional cross section of the Fermi surface for FeSCs in the 'unfolded' 1 Fe Brillouin zone [20]. There are one or two hole-like bands at the Brillouin Zone (BZ) center (Γ), and there is an electron-like band at the X point. Sometimes there is another hole-like band at the BZ corner.

Since the superconducting phase exists in close proximity to the magnetically ordered state both in cuprates and FeSCs, most popular theories of 'exotic' superconductivity use collective density-wave excitations in the spin channel as the pairing glue [14, 21]. Even though the direct Coulomb interaction between

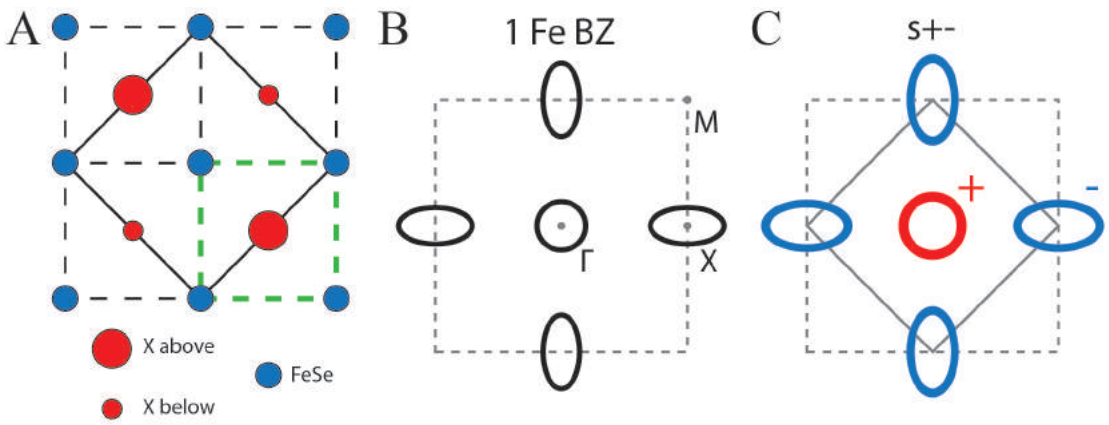

Figure 1.4: Schematic of a typical Fermi surface for FeSC. A, In FeX tri-layer, 1 Fe unit cell and the crystallographic (2 Fe) unit cells are marked with a dashed green line and solid black line, respectively. **B,** Fermi surface represented in 'unfolded' 1 Fe Brillouin zone. Usually there are one or two hole-like bands at the Γ point, and there is an electron-like band at the *X* point. For some compounds, there is another hole-like band at the *M* point. **C,** Popular proposal for the superconducting gap in FeSCs, s+-. This gap structure has s-wave symmetry which means that it preserves all point group symmetries of the tetragonal crystal. The gap on the hole-like pocket has the opposite sign compared to the gap on the electron-like pocket. Adapted from [20].

fermions is repulsive, the net interaction can have an attractive component once screening and exchange interactions with other fermions are taken into account. In particular, strong spin fluctuations lead to pairing in a state where the superconducting order parameter (also gap) changes sign between the Fermi surface regions connected by a wavevector of these fluctuations. The pairing interaction is then peaked at the wavevector of strong spin fluctuations. In FeSCs, stripe spin fluctuations at $(\pi, 0)$ and $(0, \pi)$ connect two well-nested pockets and most naturally promote s± superconducting state where the SC gap changes sign between the electron-like and the hole-like pocket (Fig. 1.4C).

Iron based superconductors are multi-orbital systems. The electronic structure within the 4-5 eV window around the chemical potential includes all five 3d orbitals of the iron. In the cubic environment, the crystal fields split the ener-

gies of the five orbitals into an upper $t2g$ triplet (i.e (d_{xy}, d_{xz}, d_{yz})) and a lower eg doublet (i.e $(d_{z^2}, d_{x^2-y^2})$). The tetragonal environment further splits the orbitals so that only d_{xz} and d_{yz} are degenerate. Finally, in the orthorhombic state, this remaining degeneracy is also lifted. Below I will discuss how the multi-orbital nature of FeSCs influences the electronic correlations inside the metallic phase out of which superconductivity emerges.

1.2 Correlations in iron based superconductors

Numerical studies of correlations in FeSCs start with the multi-orbital Hubbard model Hamiltonian,

$$\hat{H} = \sum_{i \neq j, lm\sigma} t_{ij}^{lm} c_{il\sigma}^{\dagger} c_{jm\sigma} + \sum_{il\sigma} (\epsilon_l - \mu)\, n_{il\sigma} + \hat{H}_{int} \tag{1.1}$$

where $n_{il\sigma} = c_{il\sigma}^{\dagger} c_{il\sigma}$, (i, j) are the indices for the lattice sites, and (i, j) are the orbital indices. The first term describes the kinetic (hopping) energy, ϵ_l lifts the orbital degeneracy (due to the crystal fields for instance), and μ is the chemical potential that tunes the total filling (i.e. electrons per site). $\hat{H}_{int}$ represents local multi-orbital electron-electron Coulomb interaction. The simplified version of rotationally invariant Kanamori Hamiltonian is a popular choice for $\hat{H}_{int}$ for computational reasons [22].

$$\hat{H}_{int} = U \sum_{il} n_{il\uparrow} n_{il\downarrow} + U' \sum_{i, l \neq m} n_{il\uparrow} n_{im\downarrow} + (U' - J) \sum_{i, l<m, \sigma} n_{il\sigma} n_{im\sigma} \tag{1.2}$$

where U and U' are the strengths of intra-orbital and inter-orbital repulsion, respectively, and J is the Hund's coupling. Common prescription is to set $U' = U - 2J$ (implied by rotational symmetry [23]).

We can gain some basic intuition about the Hubbard model by considering a system with a single orbital at half filling (i.e containing one electron per orbital). As the ratio of Coulomb repulsion to the width of the band U/W increases, the system undergoes a transition from a normal metal to a *Mott insulator*. In a Mott insulating ground state one electron is localized at each site to avoid a high double occupancy energy penalty imposed by large U. As we approach the transition from the normal metal side, the electronic correlations are expected to grow. Additionally, Mott insulators are antiferromagnets (at least on bipartite lattices) where electron spins on adjacent sites alternate.

Now let's return to a multi-orbital version of the Hubbard model. One popular theoretical approach to study electronic correlations in this model is spin-slave mean-field (SSMF) [24–26] theory. Numerical calculations with two, three and more orbitals show that the critical interaction strength U_c for the Mott transition is suppressed by the Hund's coupling J at half filling (i.e. n electrons in n orbitals) and enhanced for all other integer fillings [23, 25, 27]. Additionally, in the presence of sizable Hund's coupling, the half-filled Mott insulator dominates n-U/W phase diagram (n is the number of electrons specifying the filling) for $U \gtrsim U_c$ for an extended range of fillings away from half [22].

Fig. 1.5 shows SSMF calculations of several quantities - inverse electronic compressibility, total local moment, inter-orbital charge correlation function and mass enhancement - as a function of U with $J/U = 0.25$ at fixed densities in proximity of half filling for the two and three orbital model (from [22]). The crossover behavior is evident. At small U/W, the properties are consistent with the normal weakly correlated metal. At large enough U/W, mass enhancement shows the rapid rise of correlations. We call this correlated metal *Hund's metal*

[28–30]. It is a phase in which the intra-atomic exchange energy significantly influences the metallic properties [22].

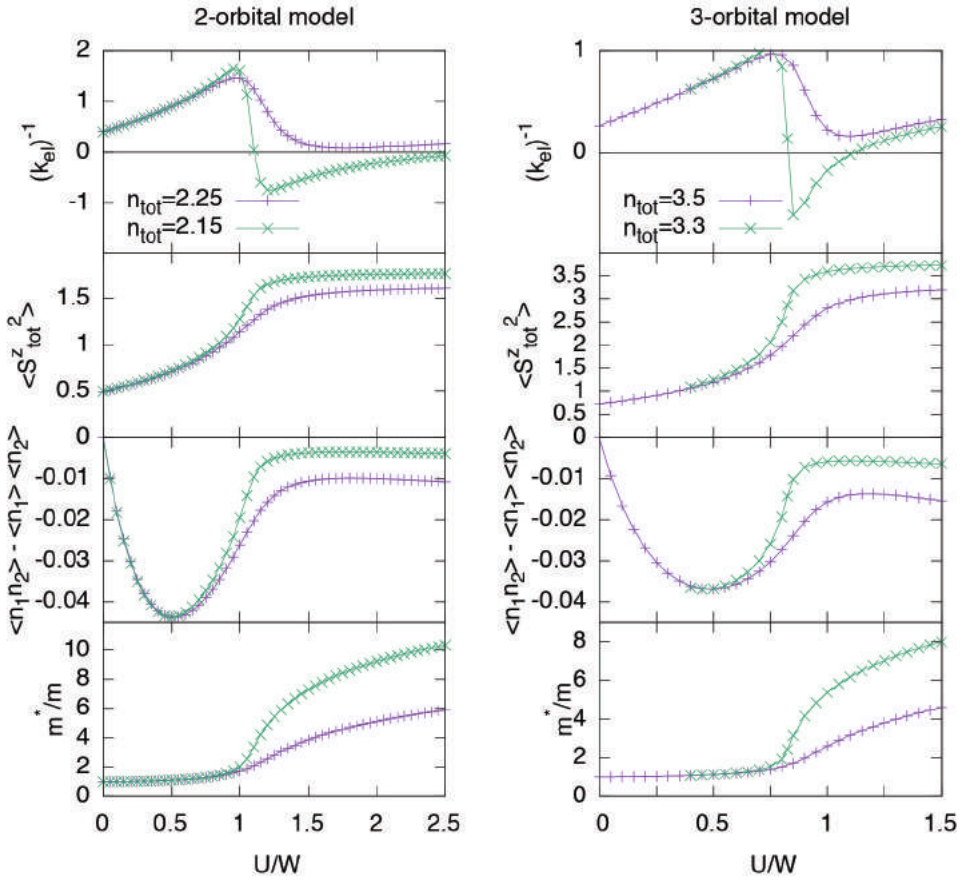

Figure 1.5: Normal to Hund's metal crossover. Calculation of inverse electronic compressibility $(k_{el})^{-1}$, total local moment $\left\langle (S^z_{tot})^2 \right\rangle$, inter-orbital charge correlation function $\langle n_1 n_2 \rangle - \langle n_1 \rangle \langle n_2 \rangle$ and mass enhancement m^*/m_b for SSMF solution of 2- and 3- orbital Hubbard model with Hund's coupling $J/U = 0.25$. Reproduced from [22].

In Fig. 1.5 the plot of the inter-orbital correlation function $\langle n_1 n_2 \rangle - \langle n_1 \rangle \langle n_2 \rangle$ illustrates an important feature of Hund's metal. At $U = 0$ the correlation is trivially zero and initially grows with increasing U before diminishing to a very low value approaching the crossover to Hund's metal. Hence we reach the conclusion that in the Hund's metal phase the charge fluctuations are independent between orbitals.

Such "orbital decoupling" [2, 22, 23, 25, 27, 31, 32] of correlations allows for the possibility of orbitally dependent proximity to the Mott insulator state. The strength of decoupled correlations in each orbital is set by the occupation of this orbital with respect to half filling [2, 31]. As the interaction strength U increases this allows for some orbital to undergo Mott transition before others. The resulting phase is referred to as the *orbital-selective Mott phase* (OSMP).

The emergence of the OSMP in paramagnetic solutions to the multi-orbital Hubbard model was extensively studied theoretically in context of FeSCs [27, 33–39]. In FeSCs three t_{2g} orbitals - d_{xz}, d_{yz}, and d_{xy} - dominate the electronic structure close to the chemical potential. In the tetragonal symmetry, d_{xz} and d_{yz} orbitals are split from d_{xy} by the crystal fields. Additionally, the in-plane nearest neighbor hopping for d_{xy} is less than for the d_{xz}/d_{yz} pair [28]. This results in greater correlations for the d_{xy} orbital and it can become Mott localized first. Angle resolved photoemission spectroscopy (ARPES) has indeed found that the OSMP is realized in iron chalcogenides [40–44]. At high enough temperature the d_{xy} orbital loses its coherent spectral weight at the Fermi energy while other orbitals remain coherent. Other experiments such as THz spectroscopy, Hall effect measurements, pump probe spectroscopy, and high pressure studies all provide further evidence for the OSMP [45–48].

The precursor to the OSMP state is a metal with orbital-selective correlations (Hund's metal). These correlations strongly influence the electronic structure of FeSCs and result in orbitally dependent mass renormalizations $\frac{m^*}{m_b}$ (where m_b and m^* are the bare band and renormalized masses, respectively). The magnitudes of mass renormalizations scale with the strength of correlations. The renormalization for states of predominately d_{xy} character reaches values of 10-20

for the iron selenides compared to substantially smaller values of 3-4 for states of d_{xz} and d_{yz} characters [42, 49].

Correlated systems remaining metallic is a consequence of Landau-Fermi liquid theory that states that the low energy and low temperature excitations of the interacting system of fermions can be adiabatically connected to the excitations of the Fermi gas (i.e. gas of non-interacting fermions) [50]. At low energies a system of strongly interacting particles can be described as a system of weakly interacting renormalized quasiparticles. The effect of interactions is captured by the self-energy $\Sigma(\vec{k},\omega)$ in associated Green's function $G(\vec{k},\omega) = \left[\omega - \xi_{\vec{k}} - \Sigma(\vec{k},\omega)\right]^{-1}$. Let's expand the denominator of the Green's function around the Fermi level and Fermi wavevector [26],

$$\begin{aligned} G(\vec{k},\omega) &= \frac{1}{\omega - \left(\xi_{\vec{k}} + \mathrm{Re}\,\Sigma(\vec{k},\omega)\right) - i\,\mathrm{Im}\,\Sigma(\vec{k},\omega)} \\ &\simeq \frac{1}{\omega - \omega\frac{\partial \mathrm{Re}\,\Sigma(\vec{k},\omega)}{\partial\omega}\Big|_{\vec{k}=\vec{k}_F}^{\omega=0} - (\vec{k}-\vec{k}_F)\cdot\frac{\partial\left(\xi_{\vec{k}}+\mathrm{Re}\,\Sigma(\vec{k},\omega)\right)}{\partial\vec{k}}\Big|_{\vec{k}=\vec{k}_F}^{\omega=0} - i\,\mathrm{Im}\,\Sigma(\vec{k},\omega)} \\ &= \frac{Z}{\omega - \tilde{\xi}_{\vec{k}} + \frac{i}{2\tilde{\tau}_{\vec{k}}(\omega)}} \end{aligned} \tag{1.3}$$

Here I defined the *quasiparticle weight Z* as a residue of the quasiparticle pole in the Green's function,

$$Z = \left[1 - \frac{\partial \mathrm{Re}\,\Sigma(\vec{k}_F,\omega)}{\partial\omega}\Big|_{\omega=0}\right]^{-1} \tag{1.4}$$

The quasiparticle weight of the interacting system is less than 1.

The band dispersion, renormalized due to interactions, is given by:

$$\tilde{\xi}_{\vec{k}} = Z(\vec{k}-\vec{k}_F)\cdot\frac{\partial\left(\xi_{\vec{k}} + \mathrm{Re}\,\Sigma(\vec{k},0)\right)}{\partial\vec{k}}\Big|_{\vec{k}=\vec{k}_F} \tag{1.5}$$

If this dispersion is put into the standard form $\tilde{\xi}_{\vec{k}} = \frac{1}{m^*}(\vec{k}-\vec{k}_F)\cdot\vec{k}_F$, this defines an

effective mass m^*.

$$\frac{m_b}{m^*} = Z\left(1 + \frac{m_b(\vec{k}-\vec{k}_F)\cdot \left.\frac{\partial \mathrm{Re}\,\Sigma(\vec{k},0)}{\partial \vec{k}}\right|_{\vec{k}=\vec{k}_F}}{(\vec{k}-\vec{k}_F)\cdot\vec{k}_F}\right) \tag{1.6}$$

If the self-energy does not depend on momentum, the mass renormalization m^*/m_b is simply $1/Z$. The important feature of this Fermi liquid description is that stronger interactions lead to smaller quasiparticle weight and stronger mass renormalizations.

Fig. 1.6 shows calculated quasiparticle weight Z as a function of filling n and relative interaction strength U/D ($D = W/2$ is half bandwidth) of the degenerate five orbital Hubbard model solved by SSMF. The Hund's coupling is set to $J/U = 0.2$ - value appropriate for FeSCs [2]. Stoichiometric Fe-based pnictides and chalcogenides have six electrons per iron occupying five 3d orbitals. According to the shown diagram, this puts these materials in the region of influence of half-filling Mott insulator and hence their metallic state has substantial correlations.

As mentioned earlier, the 3d orbitals in Fe pnictides and chalcogenides are not degenerate and correlations become orbital selective. In this situation, the quasiparticle weight depends on the orbital. Fig. 1.7 shows orbitally resolved quasiparticle weights Z_α as a function of filling calculated for doped $BaFe_2As_2$ and KFe_2As_2. A Mott insulator is realized at half filling, and for all other fillings the system is a metal with orbital-selective Mottness [31] where Z_α follows the corresponding orbital filling n_α and its proximity to half filling.

To summarize, the Hund's coupling promotes orbital-selective metallicity in the parent states of FeSCs by inducing "orbital decoupling". The key signature of this phenomenon is the difference in quasiparticle weights Z_α associated

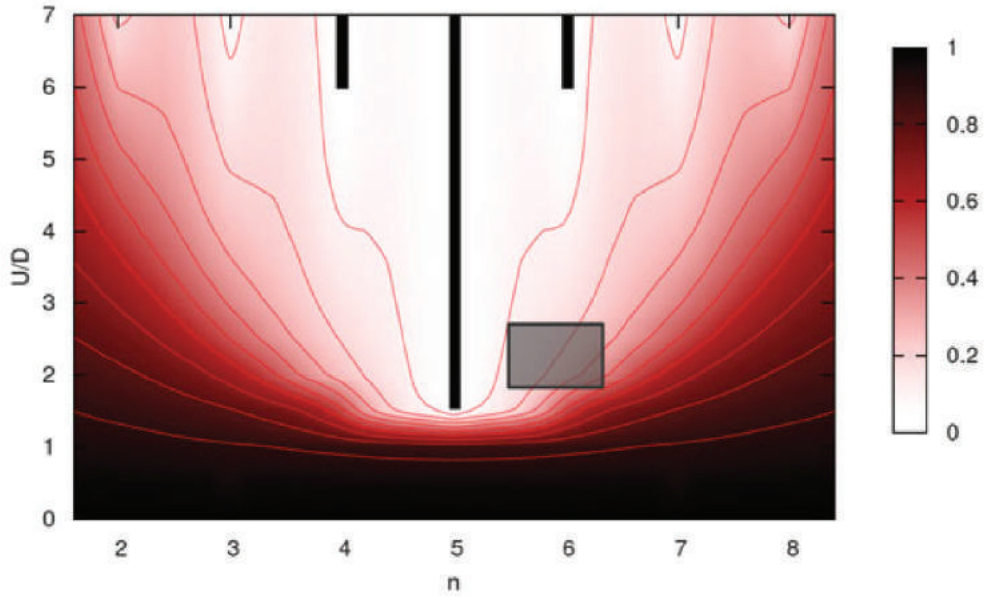

Figure 1.6: Quasiparticle weight as a function of filling and interaction strength in the five orbital Hubbard model. Black bars mark Mott transitions where Z goes to zero. Gray square corresponds realistic parameter range for FeSCs. Reproduced from [2].

with different orbitals α for specified interaction parameters $(U/W, J/U)$ and total electron filling. One important consequence of such orbital-selective correlations is the emergence of orbital-selective superconductivity [1, 51–53] where less correlated orbitals contribute more to electron (Cooper) pairing.

In Chapter 4, I will use Scanning Tunneling Microscopy (STM) as a probe of orbital anisotropy of quasiparticle weights with the focus on one of the more intriguing member of iron-based superconductor family FeSe. Therefore, it is now appropriate to finish this introductory chapter with a brief overview of FeSe physics.

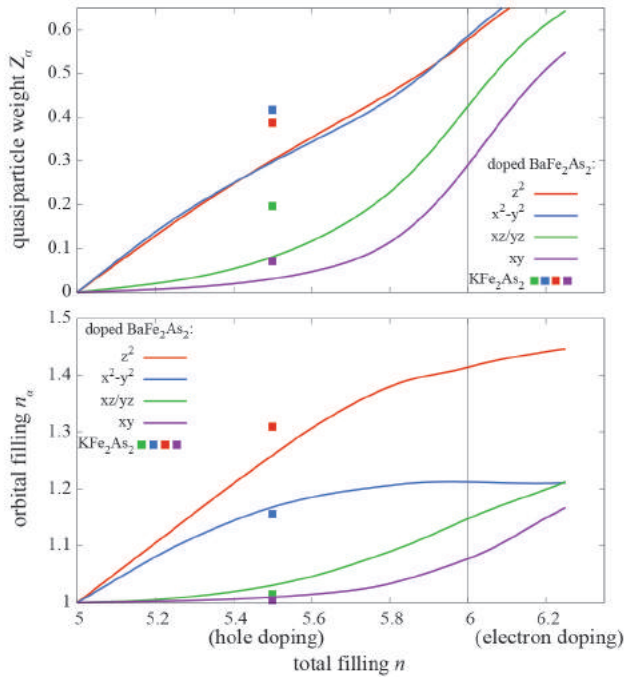

Figure 1.7: Orbitally resolved quasiparticle weight as a function of total conduction band filling for doped $BaFe_2As_2$ and KFe_2As_2. Z_α was calculated with DFT+SSMF [31]. Adapted from [2].

1.3 FeSe - one unlike the others

Structurally, FeSe is the simplest iron based superconductor. It consists of stacked FeSe trilayers with no filler layers. Despite this structural simplicity, FeSe possesses some mysterious properties that make this material unique among other FeSCs.

Like many other FeSCs, upon cooling FeSe undergoes tetragonal ($P4\backslash nmm$ space group) to orthorhombic ($Cmma$ space group) structural transition. The temperature evolution of orthorhombic lattice distortion $\delta = (a - b)/(a + b)$ indicates a second order phase transition at $T_s \approx 90K$. At low temperatures, $\delta \approx 2.7 * 10^{-3}$ [54]. If this value is normalized by the transition temperature $\delta(T = 0)/T_s$, it is nearly identical to the one obtained for $BaFe_2As_2$. However,

in contrast to '122' FeSCs, δ does not undergo any measurable change during superconducting transition that occurs at T_c = 8-9K [55].

Figs. 1.8A,C show the sketch of the crystal structure in the nematic state. In this thesis I choose the convention that the x axis is oriented along the longer orthorhombic axis. Fig. 1.8B shows STM topography of small region of clean FeSe surface exposed by cleaving at cryogenic vacuum. The crystal cleaves between two Se planes, and the visible atomic constant corresponds to Se atoms.

The structural transition is accompanied by an in-plane resistivity anisotropy [58]. Compared to $Ba(Fe_{1-x}Co_x)_2As_2$ the sign of the anisotropy $\rho_a - \rho_b$ is reversed and is positive for FeSe. Also, the magnitude of the anisotropy is only 4% of the in-plane average resistivity. In $Ba(Fe_{1-x}Co_x)_2As_2$ ρ_b is more than doubled relative to ρ_a at low temperature for x = 0.04 [59].

Aside from the resistivity anisotropy, a very clear splitting of NMR resonance lines is reported at T_s for in-plane applied magnetic field [60]. It is argued that this Knight shift anisotropy cannot be explained simply by the lattice distortion and instead should be associated with electronic nematic order.

In contrast to the other FeSCs, the nematic transition in FeSe is not followed by magnetic order. This allows for the study of the purely nematic phase - where the rotational symmetry is broken but the time reversal symmetry is preserved - over a wide temperature range [55]. The absence of magnetic order makes it unclear whether the origin of nematicity in FeSe is the same as in other FeSCs.

Recently, inelastic neutron scattering (INS) experiments have revealed that both stripe and Néel spin fluctuations are present in FeSe, and a substantial amount of spectral weight is transferred from the Néel to to the stripe fluctua-

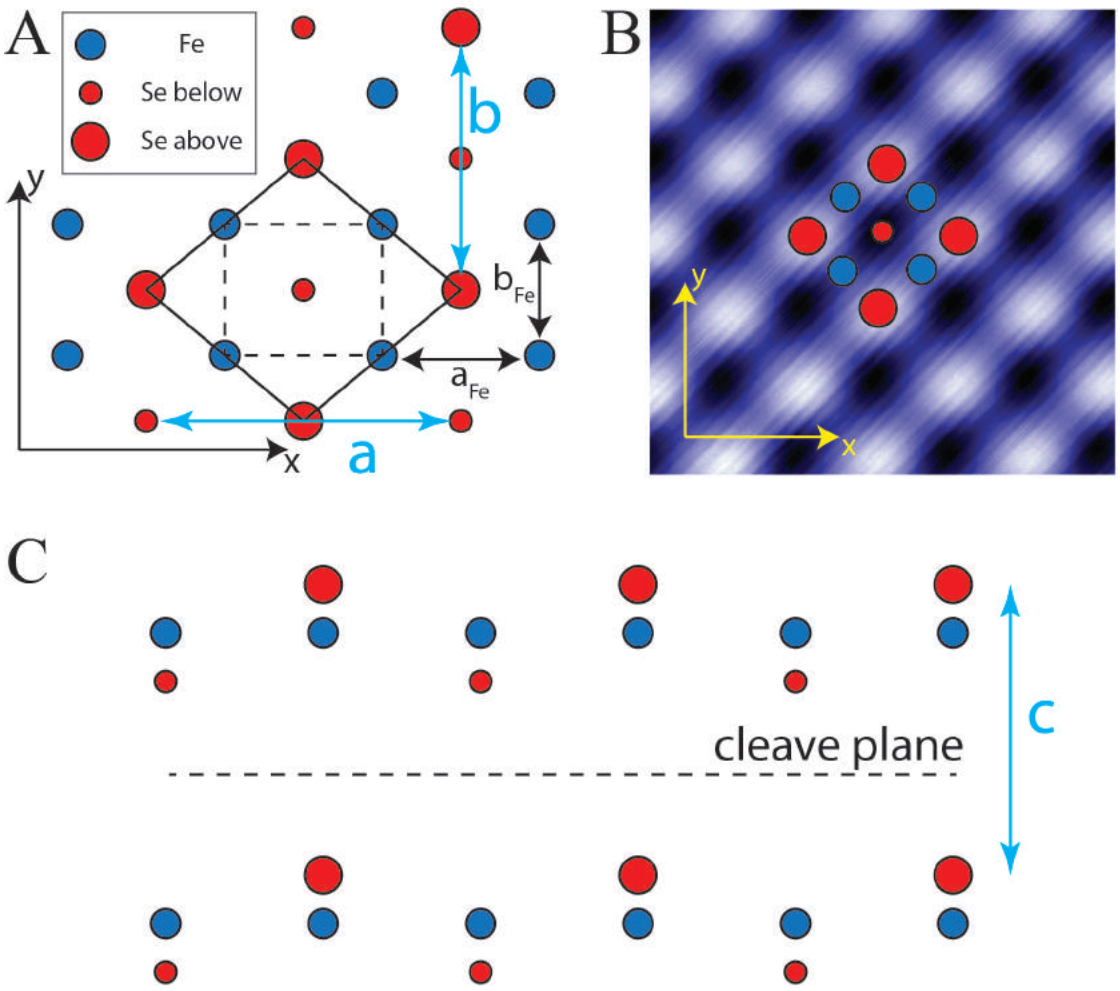

Figure 1.8: Crystal structure and surface of FeSe. A, Schematic of FeSe lattice structure in the orthorhombic phase ($T < 90$ K) viewed from the top. The crystallographic unit cell (also 2-Fe unit cell) is outlined with the solid black line. The 1-Fe unit cell is outlined with the dashed black line. The orthorhombic distortion is exaggerated for illustration purposes. The actual lattice parameters are $(a, b, c) = (5.33, 5.31, 5.48)$ Å [56, 57]. The two inequivalent nearest neighbor Fe-Fe are labelled as $(a_{Fe}, b_{Fe}) = (2.665, 2.655)$ Å. **B,** STM topography of FeSe surface. The exposed surface shows topmost Se atoms. **C,** Schematic of FeSe lattice structure viewed from the side. The cleave plane for the purpose of STM studies is between two consecutive Se planes that are loosely bonded by van der Waals forces.

tions on entering the nematic phase [61, 62]. Coexistence of both types of spin fluctuations is highly unusual since FeSe contains only one type of magnetic ions. Unlike the case of other FeSCs, the magnetic frustration seems to prevent

FeSe from ordering. In the intermediate coupling region within a frustrated J_1-J_2 model, it was predicted that FeSe would be an $S = 1$ nematic quantum paramagnet [63].

The transfer of spectral weight towards the stripe fluctuations upon cooling suggests that the system is close to the magnetically ordered stripe phase (SDW) found in many other FeSCs. Indeed, it was determined that the magnetic order is induced by high pressure (>0.8 GPa) [54,55,64,65]. Fig. 1.9 shows the pressure-temperature phase diagrams derived from several different experimental techniques, and they all demonstrate the existence of magnetic order with a dome-like pressure dependence. Initial pressure increase causes structural transition temperatures to drop and magnetic transition temperature to rise - a trend highly unusual for FeSCs [55].

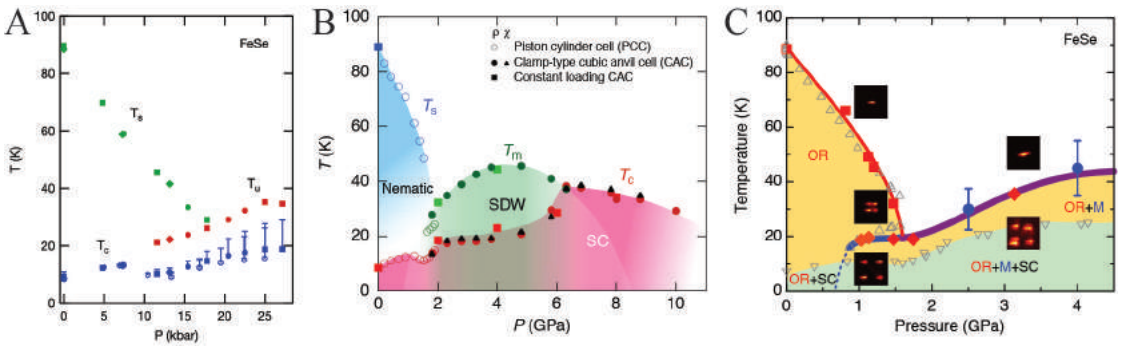

Figure 1.9: Pressure-temperature phase diagrams for FeSe. A, Resistivity and susceptibility measurements demonstrating structural and magnetic transitions in the same experiment. Reproduced from [65]. **B,** Resistivity measurement on high-quality single crystals over a large pressure range. Reproduced from [64]. **C,** X-ray diffraction and Mössbauer spectroscopy. Reproduced from [54].

Several ARPES studies looked at the electronic structure of FeSe. Fig. 1.10 shows the evolution of Fermi surface map as a function of temperature [66–68]. In the tetragonal phase there are two hole-like pockets at the zone center and two electron-like pockets at the zone corner. The nematic transition produces

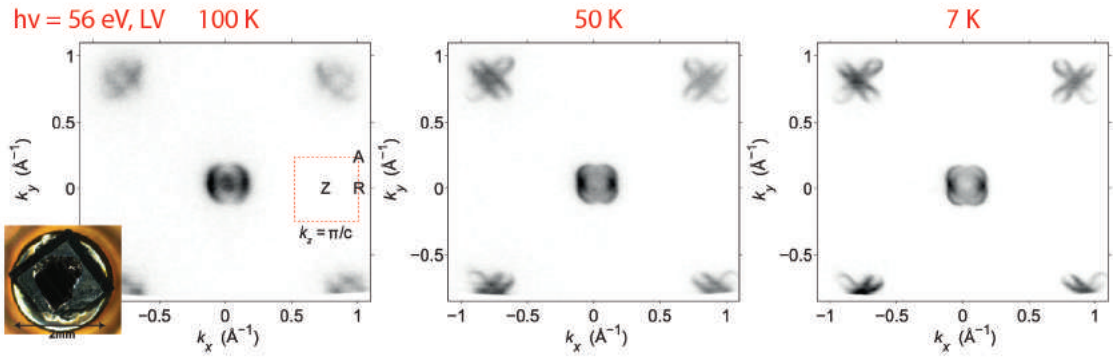

Figure 1.10: Twinned ARPES Fermi surface maps for different temperatures. Reproduced from [67].

d_{xz}/d_{yz} orbital splitting at the zone center and pushes one of the hole-like pockets below the Fermi level. Since the measurements in Fig. 1.10 were performed on samples with multiple orthorhombic domains in the nematic phase, doubling of bands due to twinning makes it hard to resolve certain details of the band structure. Therefore, ARPES was also used to study crystals detwinned by uniaxial tensile strain [69]. The resulting Fermi surface map is shown in Fig. 1.11A. Interestingly, only one electron-like pocket is visible. This observation was recently confirmed [70] (Fig. 1.11B). It suggests that one electron pocket becomes incoherent as a consequence of nematic ordering. Although at present the microscopic origin of this mysterious effect is an open problem, in Chapter 4 this incoherence is shown to also be present in STM data and is attributed to orbital selectivity of quasiparticle weights.

In the section below, I describe a tight binding parameterization of the electronic structure of the nematic state of FeSe.

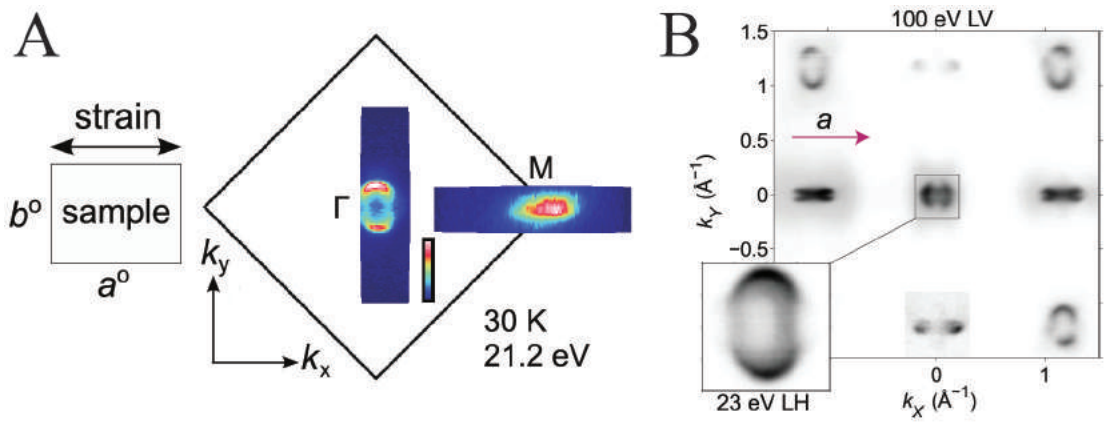

Figure 1.11: Single domain ARPES Fermi surface map in the nematic phase. **A,** Reproduced from [69]. **B,** Reproduced from [70].

1.3.1 Tight Binding Model

The following band structure parameterization of the nematic low temperature phase of FeSe was first introduced in [1]. The relevant Hamiltonian is $\hat{H} = \hat{H}_0 + \hat{H}_{OO} + \hat{H}_{SOC}$, where $\hat{H}_0$ (in real space notation) is a five orbital tight binding model given by

$$\hat{H}_0 = \sum_{\vec{r},\vec{r'},l,l'} t^{ll'}_{\vec{r}-\vec{r'}} c^{\dagger}_{l}(\vec{r}) c_{l'}(\vec{r'}) \tag{1.7}$$

where l and l' are indices running over $3d$ Fe orbitals $(d_{xy}, d_{x^2-y^2}, d_{xz}, d_{yz}, d_{3z^2-r^2})$ and $\vec{r}$ and $\vec{r'}$ are lattice sites. The convention for the axes is such that x points along the longer orthorhombic axis. For the orbital order term the momentum space representation is used,

$$\hat{H}_{OO} = \Delta_b(T) \sum_{\vec{k}} (\cos(k_x) - \cos(k_y))(n_{xz}(\vec{k}) + n_{yz}(\vec{k})) + \Delta_s(T) \sum_{\vec{k}} (n_{xz}(\vec{k}) - n_{yz}(\vec{k})) \tag{1.8}$$

Finally, the spin orbital coupling is given by

$$\hat{H}_{SOC} = \lambda \vec{L} \cdot \vec{S} \tag{1.9}$$

The low temperature parameter values are $\Delta_s = 9.6$ meV, $\Delta_b = -8.9$ meV, and $\lambda = 20$ meV. These values were chosen to achieve good agreement between

generated band structure and experimental results from detwinned ARPES [69, 70], quantum oscillations [66,71], and STM [1].

Fig. 1.12 contains the 2-dimensional cut of the low temperature band structure of nematic state of FeSe at $k_z = 0$. This cut can be considered representative of the entire 3-dimensional band structure since typically in Van der Waals (VdW) materials interplanar (k_z) dispersion is much smaller than intraplanar (k_x and k_y) dispersions. At Fermi level, there are three very small pockets. At the center of Brillouin zone (Γ), there is a nearly elliptical hole-like band α elongated along the y axis and dominated by d_{xz} and d_{yz} orbital content. At $(\frac{\pi}{a_{Fe}}, 0)$ point of Brillouin zone (X), there is a electron-like band ε dominated by d_{yz} and d_{xy} orbital character. Finally at $(0, \frac{\pi}{b_{Fe}})$ point (Y), there is another electron-like band δ of d_{xz} and d_{xy} orbital character.

1.3.2 Orbital-selective superconductivity in FeSe

Recently, my collaborators and I successfully deduced $\vec{k}$ dependence of the superconducting on α- and ε-bands in a BQPI STM experiment [1]. The measured anisotropies of the superconducting gaps $\Delta_\alpha(\vec{k})$ and $\Delta_\varepsilon(\vec{k})$ were confirmed by subsequent ARPES measurements [72,73]. There was no signal in BQPI that could be assigned to the δ-band in agreement with the missing spectral weight in detwinned ARPES experiments [69,70].

Fig. 1.13 demonstrates that the superconducting gap magnitude follows the anisotropy of the d_{yz} spectral weight near the Fermi surface expected from the tight binding parameterization of the electronic structure in the nematic state. This was interpreted as evidence for orbital-selective superconductivity where

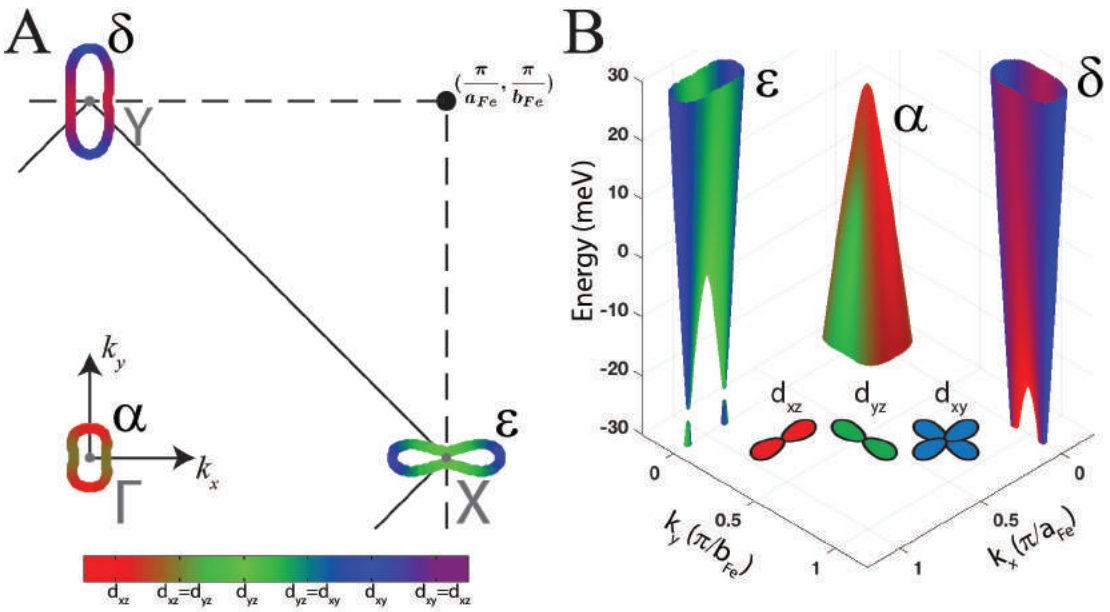

Figure 1.12: Band structure model of nematic low temperature phase of FeSe. **A,** Fermi surface contour at $k_z = 0$. The dashed and solid curves outline the 1 Fe and 2 Fe (also crystallographic) Brillouin zones (BZ). The colors represents the evolution of orbital content along the Fermi surface. Every specific eigenstate $|\mu, \vec{k}\rangle = \sum_l a_l^\mu(\vec{k})\,|l\rangle$ is mapped to a RGB color via $[R, G, B] = [|a_{xz}^\mu|^2, |a_{yz}^\mu|^2, |a_{xy}^\mu|^2]$. Here μ is a band label. **B,** Plot of $k_z = 0$ band structure of FeSe near chemical potential ($E = 0$) of generated from the tight binding model. The sketches of 2D projections of three relevant orbitals help orient the axes.

the contribution of the d_{yz}-orbital to Cooper pairing is greater than the d_{xz} and d_{xy} orbitals [1, 51].

Ref. [51] implemented the orbital-selective pairing in the weak coupling theory of exotic superconductivity based on itinerant magnetism by including orbital-selective correlations through phenomenological quasiparticle weights Z_s (i.e. Z_s is the weight of the orbital s). As discussed earlier in this chapter, the orbitally-dependent quasiparticle weights are naturally expected in the strong and intermediate coupling theories of the parent state of FeSCs that are based on the multi-orbital Hubbard model with Hund's interaction. So the mentioned approach merges two weak and strong coupling theories and hence it is not a

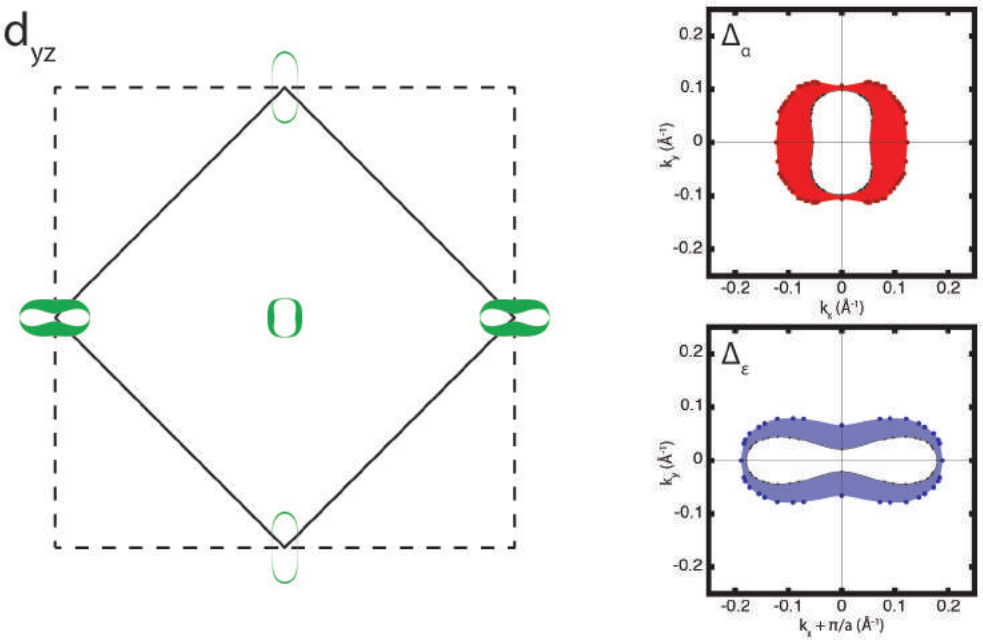

Figure 1.13: Orbital-selective superconductivity in FeSe. left, d_{yz} content at the Fermi surface represented by line thickness. **right,** Line thickness shows measured superconducting gap anisotropy on α and ε pockets of FeSe. Reproduced from [1].

self-consistent theory of FeSC superconductivity. However, it does raise an important theoretical issue. If inclusion of strong orbital-selective correlations is required to obtain the correct superconducting gap anisotropy within the weak coupling theory, this would imply that weak coupling is simply not enough to capture all important details of the superconducting state.

A major part of this thesis will focus on confirming the existence for orbital-selective correlations in FeSe using STM measurements. I will identify an observable in STM data that is sensitive to the orbital anisotropy of quasiparticle weights and will use this as a probe of such correlations.

1.4 Thesis outline

This thesis focuses on STM studies of nematic phase of FeSe. In **Chapter 2**, I give an overview of STM instrument and its functionality. I also discuss the relevant tunneling theory and relate STM observables to functions of the local density of states. Next in **Chapter 3**, I discuss a major application for STM studies - visualization of modulations of the local density of states that appear due to quasiparticle interference. Importantly, I relate the power spectrum of these modulations to the electronic structure of the measured material in momentum space. Then in **Chapter 4**, I analyze measured quasiparticle interference patterns in FeSe and interpret them in the context of orbital-selective correlations. In **Chapter 5**, I shift gears to look at the structure of the STM data images at the atomic scale. I show that at low energies the real space intra unit cell electronic structure of the nematic state of FeSe is noticeably directional despite the fact that the orthorhombic lattice distortion is very small. Finally, in **Chapter 6** I pose some open problems to provide an outlook on future STM studies of FeSe and other related systems.

CHAPTER 2

INTRODUCTION TO SCANNING TUNNELING MICROSCOPY

Gerg Binnig and Henrich Rohrer developed the scanning tunneling microscope (STM) in the early 1980s. It rapidly became a powerful tool for imaging the local electronic structure of conducting solid surfaces [74] at the atomic scale, earning its inventors a 1986 Nobel Prize in Physics.

Modern STM devices operate as follows. A sharp metallic tip is rigidly attached to a piezoelectric tube scanner. A piezoelectric tube scanner is a tube of piezoelectric ceramic with several electrodes. The exact number of electrodes and their arrangement can vary depending on the design. Fig. 2.1A shows a sketch of a typical scanner. There are four external electrodes (+X,-X,+Y,-Y) - symmetrically arranged around the tube, one external circumferential electrode (+Z) and one internal circumferential grounded electrode. Applying voltages of opposite polarity on the opposing electrodes (i.e. +X/-X and +Y/-Y) bends the tube in the corresponding direction. Applying a positive (negative) voltage on Z electrode lengthens (shortens) the scanner tube. The control of the tip's position (x, y, z) with picometer precision, enabled by the piezoelectric tube, allows STMs to image surfaces with atomic resolution (see Fig. 2.1B).

The scanner tube is housed in a holder that is attached to a coarse approach motor capable of parking the tip within hundreds of angstroms away from the surface. When the scanner brings the tip in close enough proximity (i.e. several angstroms) to a conducting surface via the Z voltage of the scanner, the quantum mechanical wave functions of the tip and the surface that extend into the vacuum start to overlap (Fig 2.1C). If a voltage is then applied to the tip relative to the surface, current flows through the junction because of quantum tunnel-

ing, and its magnitude is proportional to the energy integral of the density of states (see the next section). STM is a powerful experimental technique due to its ability to visualize the local density of states with the atomic resolution.

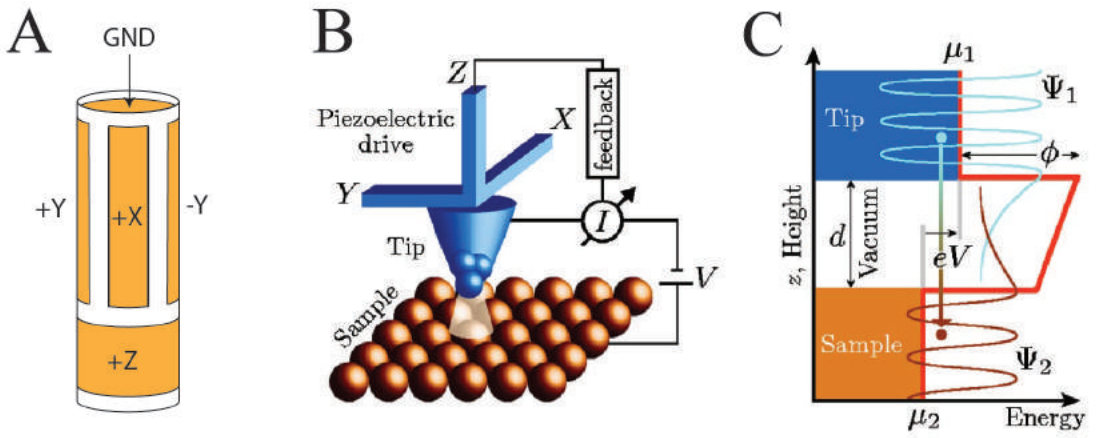

Figure 2.1: Principle of STM operation A, Schematic of a piezoelectric tube scanner. **B,** Schematic of STM tip in the proximity of the measured surface. **C,** Sketch of quantum mechanical tunneling between the tip and the surface. **B** and **C** are reproduced from [75].

2.1 Tunneling theory

The theoretical underpinning for STM research is described in the classic paper by Tersoff and Hamann [76]. This paper uses a simple geometric model for the metallic tip in conjunction with Bardeen's tunneling formalism [77] to derive the basic formulae relating measured tunneling current and the density of states of the sample. The basic starting expression for the tunneling current is provided below.

$$I = \frac{2\pi e}{\hbar} \sum_{\mu,\nu} f(E_\mu)[1 - f(E_\nu + eV)]|M_{\mu\nu}|^2 \delta(E_\mu - E_\nu) \tag{2.1}$$

Here $f(E)$ is the Fermi-Dirac distribution, and $M_{\mu\nu}$ is the tunneling matrix element between states ψ_μ of the tip and ψ_ν of the surface. In Bardeen's formalism,

the matrix element is given by the following formula.

$$M_{\mu\nu} = \frac{\hbar^2}{2m} \int d\vec{S} \cdot (\psi_\mu^* \vec{\nabla} \psi_\nu - \psi_\nu \vec{\nabla} \psi_\mu^*) \tag{2.2}$$

It can be shown that within the spherical model for the tip, the matrix element can be evaluated, and the tunneling current can be cast in the following simple form [76].

$$\begin{aligned} I &= \frac{4\pi e}{\hbar} e^{-d\sqrt{\frac{8m\phi}{\hbar^2}}} n_t(0) \int_{eV}^{0} n_s(\epsilon) d\epsilon \\ &= \frac{4\pi e^2}{\hbar} e^{-d\sqrt{\frac{8m\phi}{\hbar^2}}} n_t(0) \int_0^V n_s(eV') dV' \\ &= 2\pi^2 G_0 e^{-d\sqrt{\frac{8m\phi}{\hbar^2}}} n_t(0) \int_0^V n_s(eV') dV' \end{aligned} \tag{2.3}$$

Here V is the voltage applied to the sample relative to the tip which is grounded. The work function of the material is ϕ, the tunnel barrier length is d, and the quantum of conductance $\frac{2e^2}{\pi\hbar}$ is G_0. Finally, n_s and n_t are the sample and tip density of states respectively. Note that for negative (positive) V in Eq. 2.3, we are integrating over the states below (above) the chemical potential.

2.2 Types of STM measurements

In the following I will outline the different modes of STM operation.

2.2.1 Topography

The most basic type of STM measurement is a *topograph*. It is a constant current scan across the sample surface. During a scan, the Electronic Control Unit

(ECU) in combination with a control computer regulates the feedback mechanism that maintains the tunneling current at a constant specified value by continuously changing the Z voltage of the piezo scanner tube. This voltage is sampled and saved during the scan generating a topographic image $T(\vec{r})$ of the surface. Fig 2.2 shows an example of such an image.

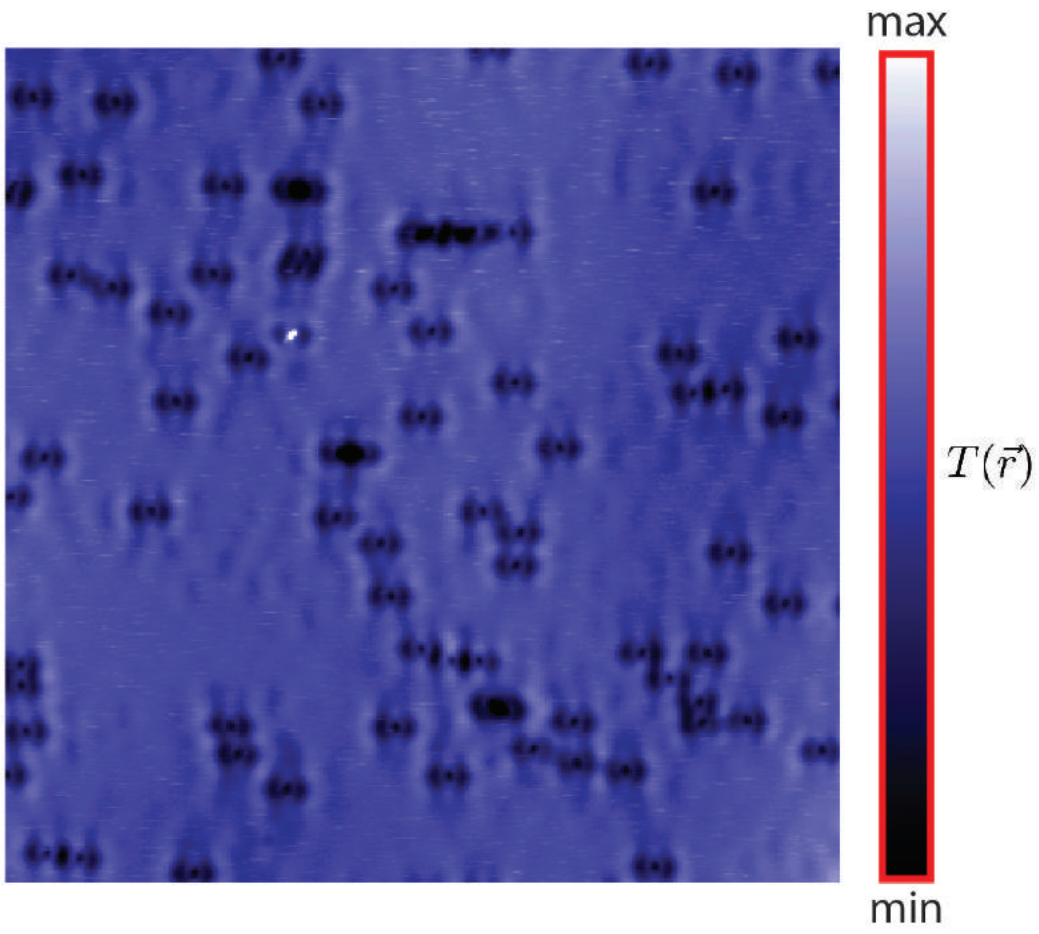

Figure 2.2: STM Topograph $T(\vec{r})$ showing surface of FeSe superconductor. The tip was scanned across the surface of FeSe line by line at the speed of 20 nm/s. The junction bias was set to -5 mV. The PID feedback kept the tunneling current at a constant value of 250 pA by continuously adjusting the Z piezo voltage. The total number of scan lines was 512, and the sample region scanned was 90 nm by 90 nm. During each line scan, 512 Z piezo voltage values was recorded at evenly spaced intervals. Thus 512 by 512 image of the 90 nm FOV was generated.

Assuming the measured sample field of view (FOV) does not have any step edges and debri, we can relate $T(\vec{r})$ to the density of states using Eq 2.3 by solving for the barrier width $d(\vec{r})$.

$$\begin{aligned} T(\vec{r}) \sim d(\vec{r}) = & \sqrt{\frac{\hbar^2}{8m\phi}} \ln\left(\frac{4\pi e^2}{\hbar|I|} n_t(0)\right) + \sqrt{\frac{\hbar^2}{8m\phi}} \ln\left(\left|\int_0^V n_s(eV')dV'\right|\right) \\ & \sim \ln\left(\left|\int_0^V n_s(eV')dV'\right|\right) \end{aligned} \tag{2.4}$$

Here symbol $\sim$ means a linear relationship between quantities. That is $y \sim x$ means $y = m \cdot x + b$. Hence the contrast in $T(\vec{r})$ represents variations in the energy integrated sample density of states.

2.2.2 dI/dV spectroscopy

Another type of STM measurement is dI/dV spectroscopy. If Eq. 2.3 is differentiated with respect to voltage, the following expression is obtained.

$$\frac{dI}{dV} = 4\pi^2 G_0 e^{-d\sqrt{\frac{8m\phi}{\hbar^2}}} n_t(0) n_s(eV) \tag{2.5}$$

Hence measuring dI/dV as a function of the sample bias gives us access to the sample density of states n_s as a function of energy.

The dI/dV is normally acquired experimentally using the following method. The ECU adds a sinusoidal ripple $dV(t)$ from a lock-in amplifier is to the sample bias voltage. The tunneling current $I = I_0 + \frac{dI}{dV} dV(t)$ will then pick up a sinusoidal modulation with the amplitude proportional to $\frac{dI}{dV}$. The output current is converted into the voltage signal by the preamplifier, and the output voltage ripple amplitude is measured using the lock-in amplifier.

2.2.3 Spatial dI/dV mapping and the setup effect

One of the most useful and powerful STM measurements in modern research of quantum materials is the $\frac{dI}{dV}$ *spectroscopic map* (also *g map*) where $\frac{dI(V)}{dV}$ spectra are sequentially acquired on a two dimensional pixel grid spanning a certain region of a sample. A spectroscopic map can be viewed as a sequence of $\frac{dI}{dV}(\epsilon = eV, \vec{r})$ images stacked along the energy axis (Fig. 2.3). The impor-

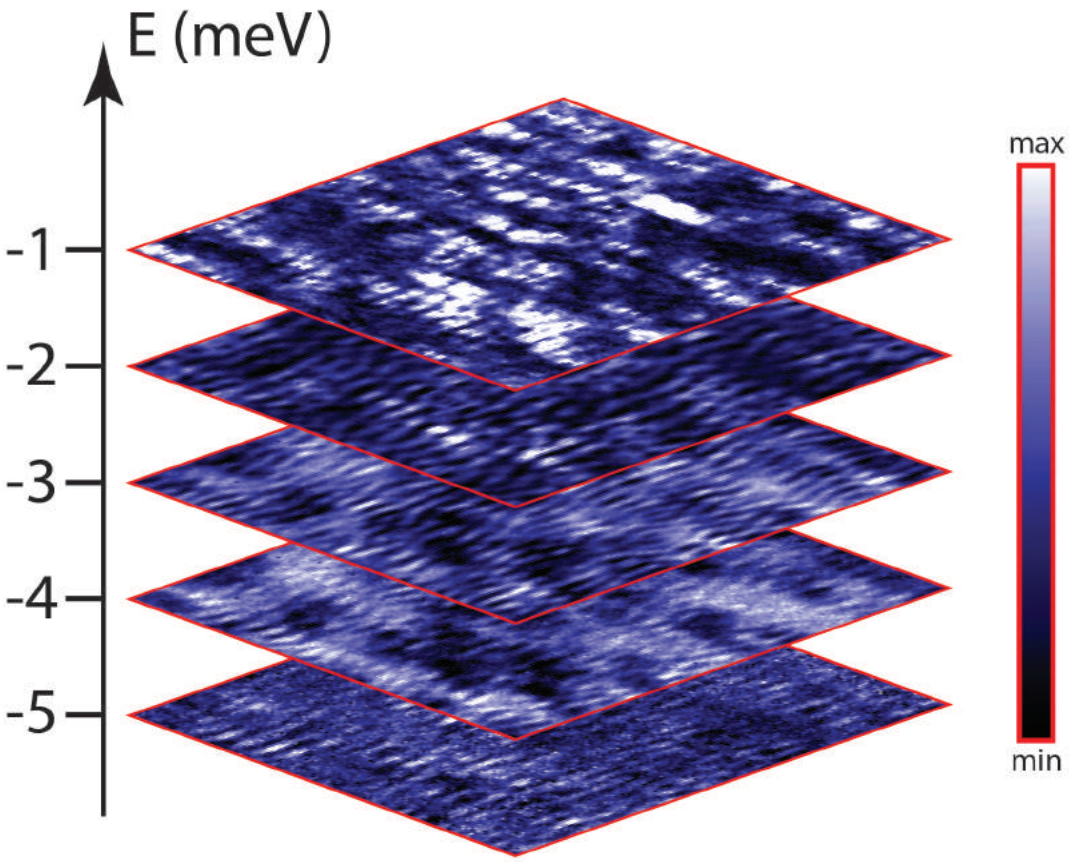

Figure 2.3: Schematic of $\frac{dI}{dV}$ spectroscopic map A sequence of stacked conductance images visualizing spatial modulations of the local density of states as a function of energy.

tance of spectroscopic maps will be discussed in the next chapter in the context of *quasiparticle interference* - a technique that gives a lot of information about the sample band structure as well as the superconducting gap structure for the

superconducting samples. Additionally, this type of measurement allows the visualization of vortex lattices in type II superconductors.

To discuss the spatial dependence of STM spectra, the position coordinate is explicitly added to equations 2.3 and 2.5.

$$I(\vec{r}) = \frac{4\pi e^2}{\hbar} e^{-d(\vec{r})\sqrt{\frac{8m\phi}{\hbar^2}}} n_t(0) \int_0^V n_s(eV', \vec{r}) dV' \tag{2.6}$$

$$\frac{dI}{dV}(V, \vec{r}) = \frac{4\pi e^2}{\hbar} e^{-d(\vec{r})\sqrt{\frac{8m\phi}{\hbar^2}}} n_t(0) n_s(eV, \vec{r}) \tag{2.7}$$

Here the position coordinate $\vec{r}$ appears not only in the local density of states of the sample $n_s(\vec{r})$ but also in the tip-sample separation distance d. It is not possible in a sensible way to measure at constant d in the situation where both the density of states and the surface height depend on the location. The surface height can vary because of step edges, surface debri and overall sample tilt. Since the tunneling current is what can be measured locally, the spectroscopic maps are acquired at a constant setup current. At every location on the two dimensional grid, the STM control system uses PID feedback to vary the Z voltage of the piezo scanner until the specified current is reached at the fixed junction bias, and then the spectrum ($\frac{dI}{dV}$ as function of voltage) is acquired.

This discussion has a profound effect on the interpretation of spectroscopic maps. Suppose a certain spectroscopic map is acquired at the setup bias voltage V_0 and the setup current I_0. Eq. 2.6 can be used to relate the two parameters.

$$I_0 = \frac{4\pi e^2}{\hbar} e^{-d(\vec{r})\sqrt{\frac{8m\phi}{\hbar^2}}} n_t(0) \int_0^{V_0} n_s(-eV', \vec{r}) dV' \tag{2.8}$$

Using this relation, the equations 2.6 and 2.7 can be rewritten in terms of experimental map parameters, I_0 and V_0.

$$I(V, \vec{r}) = I_0 \frac{\int_0^V n_s(eV', \vec{r}) dV'}{\int_0^{V_0} n_s(eV', \vec{r}) dV'} \tag{2.9}$$

$$g(V,\vec{r}) \equiv \frac{dI}{dV}(V,\vec{r}) = I_0 \frac{n_s(eV,\vec{r})}{\int_0^{V_0} n_s(eV',\vec{r})dV'} \tag{2.10}$$

The spectroscopic map $g(V,\vec{r})$ was conventionally used in a lot of STM studies. Note that the denominator $\int_0^{V_0} n_s(eV',\vec{r})dV'$ in Eq. 2.9 and Eq. 2.10 depends on $\vec{r}$. This is known as *the setup effect*, and it is a major problem since ideally all the spatial dependence of spectroscopic maps would be contained in the physically relevant local density of states. It is clear that the specific map $g(V,\vec{r})$ depends on the chosen experimental parameters I_0 and V_0.

To address the setup effect, other types of spectroscopic maps were introduced. In superconductors, the density of states are particle-hole symmetric near the chemical potential, and the following function becomes useful [78].

$$Z(V,\vec{r}) = \frac{g(V,\vec{r})}{g(-V,\vec{r})} = \frac{n_s(-eV,\vec{r})}{n_s(eV,\vec{r})} \tag{2.11}$$

The theoretical justification for making scientific deductions from $Z(V,\vec{r})$ relies on the fact that the perturbation to the local density (see next chapter) of Bogoluibov quasiparticles due to impurity scattering at energy eV has substantial out of phase component spatially with respect to corresponding perturbation at energy $-eV$ [79, 80]. Suppose we decompose the local density of states $n(\vec{r}) = n_0 + \delta n(\vec{r})$ into a uniform component, n_0, and a perturbation due to scattering from surface defects, $\delta n(\vec{r})$. As shown below, if the perturbations are small, there is a linear relationship between $Z(V,\vec{r})$ and the anti-symmetrized function, $\delta n_{odd}(eV,\vec{r}) = \delta n(eV,\vec{r}) - \delta n(-eV,\vec{r})$, and the setup effect is removed [81].

$$\begin{aligned} Z(V,\vec{r}) &= \frac{n_0 + \delta n(eV,\vec{r})}{n_0 + \delta n(-eV,\vec{r})} \approx (1 + \frac{\delta n(eV,\vec{r})}{n_0})(1 - \frac{\delta n(-eV,\vec{r})}{n_0}) \\ &\approx 1 + \frac{\delta n(eV,\vec{r}) - \delta n(-eV,\vec{r})}{n_0} = 1 + \frac{\delta n_{odd}(eV,\vec{r})}{n_0} \end{aligned} \tag{2.12}$$

Another spectroscopic function appropriate for all samples and not only superconductors is the normalized conductance (also called *Feenstra parameter* or L

map) $L(V, \vec{r})$ [82].

$$L(V, \vec{r}) = \frac{\frac{dI}{dV}}{\frac{I}{V}} = V \frac{n_s(eV, \vec{r})}{\int_0^V n_s(eV', \vec{r}) dV'} \tag{2.13}$$

Compared to Eq. 2.10, it seems like no progress was made. However, note that even though the position dependence in the denominator survives, $L(V, \vec{r})$ does not depend on the arbitrarily chosen parameters I_0 and V_0. The spectroscopic normalized conductance maps on the same material but acquired using different setup conditions can be compared directly. Also as will be discussed in the next chapter, $L(V, \vec{r})$ can be theoretically computed within the T-matrix approximation.

2.3 Experimental setup

Here I review the important aspects of the experimental setup used for the STM studies presented in this thesis.

2.3.1 Vibration isolation

Since the tunneling current has an exponential dependence on the tip sample separation, it is critically important to minimize any mechanical vibrations reaching the tunnel junction. Any mechanical noise diminishes the performance of STM especially in the spectroscopic mode. Most STM instruments acquire a local spectrum without active feedback, and therefore fluctuations in the tunnel barrier height during a measurement can result in changes in the conductance greater than the spectral features under consideration.

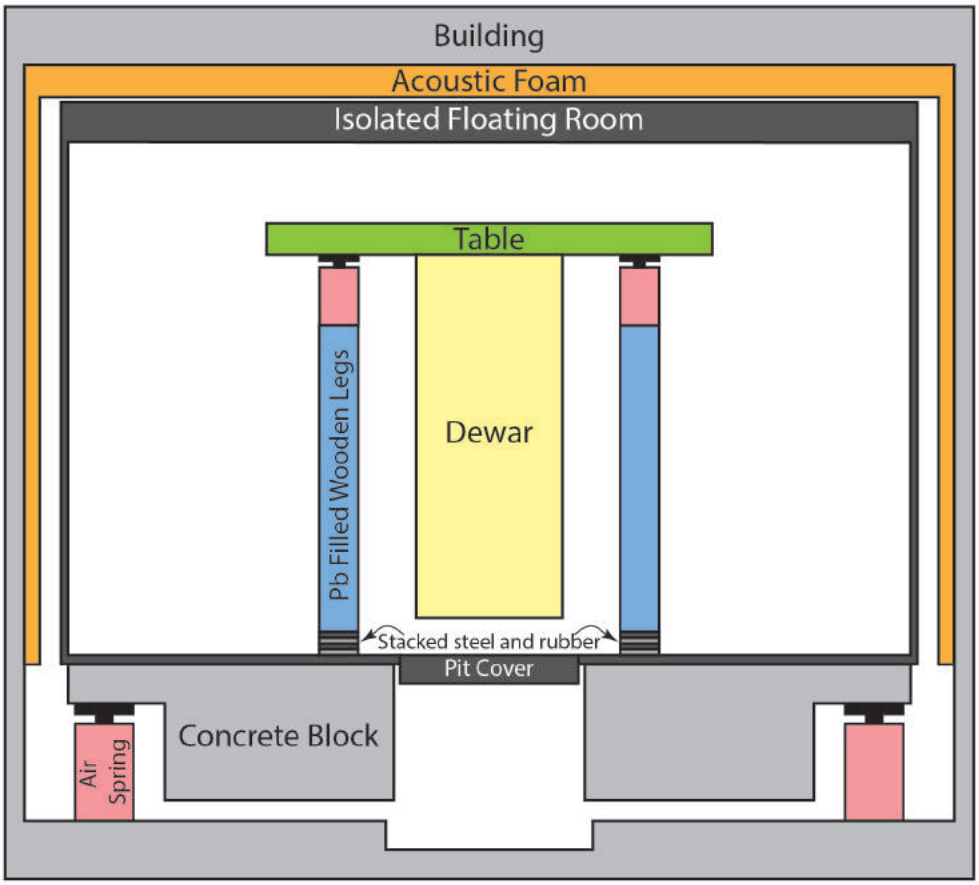

Figure 2.4: Schematic of the vibration isolation system. The room containing the cryostat seats on the 30 ton concrete block isolated from the main building using high load air springs. Dewar is suspended from the 1.5 ton table filled with lead. The table is connected to the air springs supported to the three lead filled wooden legs weighing 0.5 ton each. The schematic is not to scale.

There are two ways to enhance signal-to-noise ratio (SNR) of spectroscopic STM measurements. (The fundamental source of noise discussed is presumed to be mechanical since the electrical noise is mitigated with well designed electronics that use proper shielding and filters.) One way is to increase the averaging time during data acquisition. However, longer averaging times per data point will put limits on the resolution of spectroscopic maps that can be obtained in low temperature studies since the helium dewars have finite hold time restrict-

ing the total number of spectra that can acquired between helium refills. (A data point is a $\frac{dI}{dV}$ measurement acquired at a specified junction bias V and a particular location $\vec{r}$ on the sample surface.)

The other way is to reduce mechanical vibrations reaching the tunnel junction from the environment. This can be accomplished with a vibration isolation system utilizing the principle of mechanical impedance mismatch [83] which refers to the fact that energy propagation is poor between the subsystems with mechanical modes that significantly differ in resonance frequencies. Hence, by connecting a stiff and light STM scanner to a sequence of progressively heavier and softer mechanical stages, we can greatly attenuate the mechanical noise that reaches the junction.

A very successful implementation of such a system is used in the Davis group at Cornell University. It is sketched in Fig. 2.4. The room with the cryostat is isolated from the main building using four high load air springs. To drive the fundamental vibrational mode of the room down in frequency, a 30 ton concrete block is used. Inside the room, the superinsulation dewar enclosing the experiment is bolted to the triangular table. The table is filled with lead bringing its weight to 1.5 tons. It is isolated from the three wooden support legs with another set of air springs. Each support leg is also filled with lead and weighs 0.5 tons. The legs are connected to the room with stacked rubber and steel pads. Note that the setup described above can be viewed as a set of mechanical stages with each stage characterized by associated mass and spring constant. The first stage (the floating room supported by the set of air springs) has resonance frequency of a few Hz whereas one of the final stages (STM scanner supported by the press plate) has resonance frequency in hundreds of kHz. Hence, the me-

chanical vibrations from the environment are greatly attenuated at the tunnel junction.

The last thing worth mentioning in this section is a common source of the mechanical noise originating inside of liquid helium cryostat with 1K pot stages. It is of paramount importance to cool the liquid helium entering the 1K pot. If the liquid helium inside the pot is superfluid but the liquid helium entering the pot is in the normal phase, there will be mechanical vibrations generated in the cryostat. These vibrations can then reach the STM head and reduce the experimental performance.

2.3.2 Cryostat

Looking back at Eq. 2.1, it becomes apparent that STM spectroscopy has a thermal resolution of a few k_BT because of the presence of Fermi-Dirac distribution. For SIN (superconductor-insulator-normal) tunnel junctions, the thermal broadening of $3.5k_BT$ is usually quoted [84]. In modern research of quantum materials (e.g. superconductors, heavy fermion systems), many interesting spectral features are of order meV and less. At 4 K, the relevant thermal broadening is $3.5k_BT = 1.2$ meV. Hence, these types of studies requires STM spectroscopy at cryogenic temperatures typically utilizing liquid helium.

Majority of STM studies contained in this thesis were performed using the STM housed inside of ^{3}He cryostat [85]. The operation temperature that can be achieved is 280 mK which corresponds to an energy resolution of about $0.085meV$. The schematic of the cryostat is shown in Fig. 2.5.

The cryostat has 1 K pot stage to pre-cool the system to 1.2 K to reduce the thermal load on the ^{3}He stage. The ^{3}He is not circulated. Instead, activated charcoal sorption pump is used. The charcoal is lowered to the 4K stage to start pumping on the ^{3}He. Once a week, the ^{3}He needs to be liberated and re-liquified by raising the charcoal closer to the room temperature stage. This is usually synchronized with liquid ^{4}He transfers into the dewar since its hold time is also about a week. Additionally the dewar contains a superconducting magnet capable of generating maximum magnetic field of 8.5 T at the sample location.

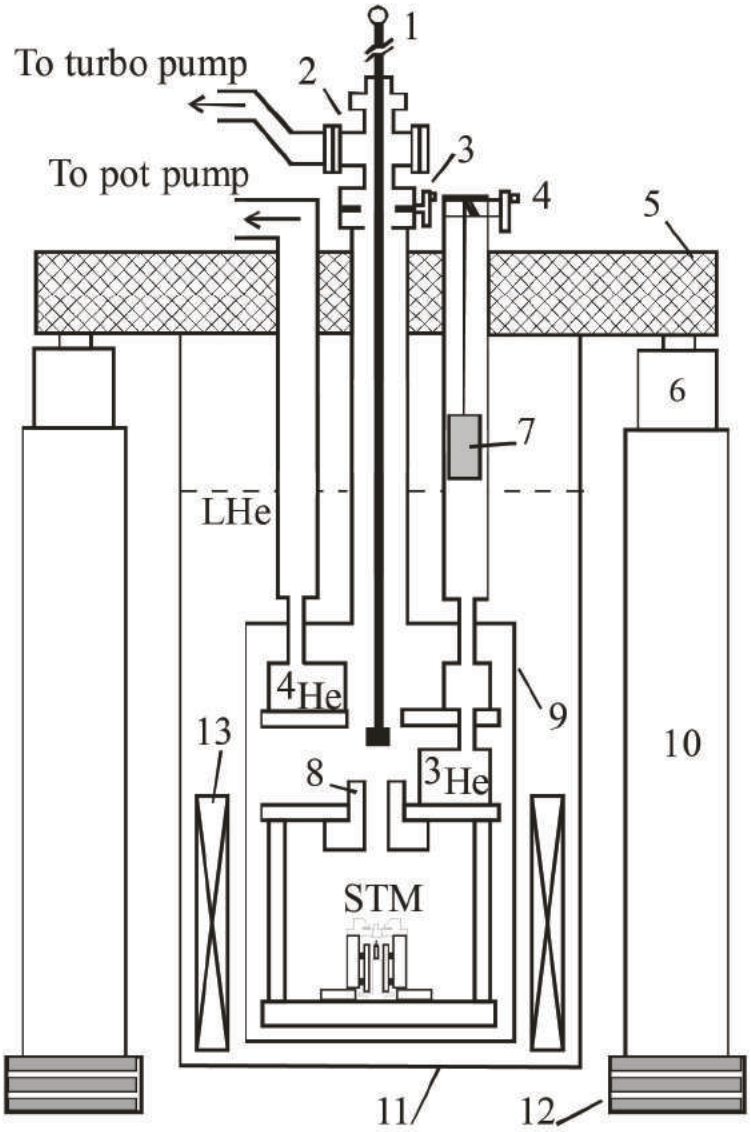

Figure 2.5: Schematic of the STM cryostat. (1) Sample manipulator rod, (2) Sample loading chamber, (3) Gate-valve, (4) Charcoal sorption pump lift/lowering mechanism, (5) Lead filled table top for vibration isolation, (6) Air-spring, (7) Activated charcoal sorption pump, (8) Mechanical sample cleavage stage, (9) Vacuum chamber, (10) Supporting table leg, (11) Superinsulation dewar, (12) Stacked rubber and steel pads, (13) 8.5 T magnet. Schematic is not to scale. Reproduced from [85].

CHAPTER 3

IMAGING QUASIPARTICLE INTERFERENCE

In the Lindhard theory of screening, the asymptotic form of the induced charge due to a point defect in a D-dimensional uniform electron gas contains an oscillating term [86].

$$\rho_{ind}(\vec{r}) \approx \delta n \frac{\cos(2k_F|\vec{r}| + \delta)}{|\vec{r}|^D} \tag{3.1}$$

These $2k_F$ oscillations are known as Friedel oscillations. Similar oscillations occur in the local density of states inside a metal due to quasiparticle scattering from impurities or defects [87–90]. This phenomenon is called quasiparticle interference (QPI).

As shown below, the evolution of the wavevectors of LDOS modulations in a given material as a function of energy is directly related to its band structure. This fact turns SI-STM into a powerful band structure probe that has certain advantages over angular resolved photoemission spectroscopy (ARPES) - a popular experimental technique for band structure measurements. Unlike ARPES, STM measurements are not limited to zero magnetic field and energies below the chemical potential. Additionally, in combination with dilution or ^{3}He refrigerator, STM can boast of high energy resolution not yet achieved by ARPES.

This chapter discusses the basic theory of LDOS modulations produced by quasiparticle interference (QPI) and serves as a prelude to the following chapter where STM measurements of QPI patterns in the nematic state of FeSe will be analyzed in the context of orbital-selective correlations.

3.1 Introduction

In a periodic crystal, the quasiparticle states take form of Bloch waves $\psi_{\vec{k}}(\vec{r}) = e^{i\vec{k}\cdot\vec{r}}u(\vec{r})$ where $u(\vec{r})$ is a function of lattice periodicity [91]. Since the density of states depends on the sum of the squared amplitudes of the eigenstates (i.e. $n(E,\vec{r}) \propto \sum_{\vec{k}} \left|\psi_{\vec{k}}(\vec{r})\right|^2 \delta(E - E(\vec{k}))$), which for Bloch waves do not depend on wavevectors $\vec{k}$ (i.e. $\left|\psi_{\vec{k}}(\vec{r})\right|^2 = \left|u(\vec{r})\right|^2$), the local density of states does not contain any $\vec{k}$ space information in a perfectly periodic system.

The situation changes drastically once the crystal has defects that destroy the perfect periodicity of the problem. To the lowest order, in the vicinity of defects, new eigenstates corresponding to a certain energy become linear combinations of old eigenstates of the same energy (i.e Bloch waves). Since a linear combination of Bloch waves depends on multiple $\vec{k}$s, its squared amplitude contains sinusoidal oscillations whose wavevectors are differences of these $\vec{k}$s (see Section 3.2.1 below for details). Hence, due to interference of quasiparticle states, LDOS close to defects will have oscillations that contain $\vec{k}$-space information.

To elucidate the utility of these oscillations as a band structure probe, consider a metal with a single parabolic band $E(\vec{k}) = \frac{\hbar^2|\vec{k}|^2}{2m} - E_0$. The perturbation to the LDOS caused by a single impurity with short range potential can readily be calculated within the T-matrix formalism (Section 3.2.2). The result of this calculation reveals that such perturbation $\delta n(E,\vec{r})$ is dominated by oscillations with wavevectors satisfying $\vec{q}(E) = 2\vec{k}(E)$. Such oscillations are caused by interference of the $|\vec{k}(E)\rangle$ and $|-\vec{k}(E)\rangle$ states where the notation $\vec{k}(E)$ denotes that E is the energy of the $|\vec{k}\rangle$ state. Fig. 3.1A shows a typical $\vec{r}$-space QPI pattern calculated at a single energy for a parabolic band. In the calculation it is assumed

that the system has several randomly distributed maximally localized defects. By localized defect, I mean that its scattering potential is a delta function in real space. Fig. 3.1B then shows the QPI pattern in $\vec{q}$-space (i.e. the amplitude of the Fourier transform of Fig. 3.1A), where a ring defined by $\vec{q}(E) = 2\vec{k}(E)$ is apparent.

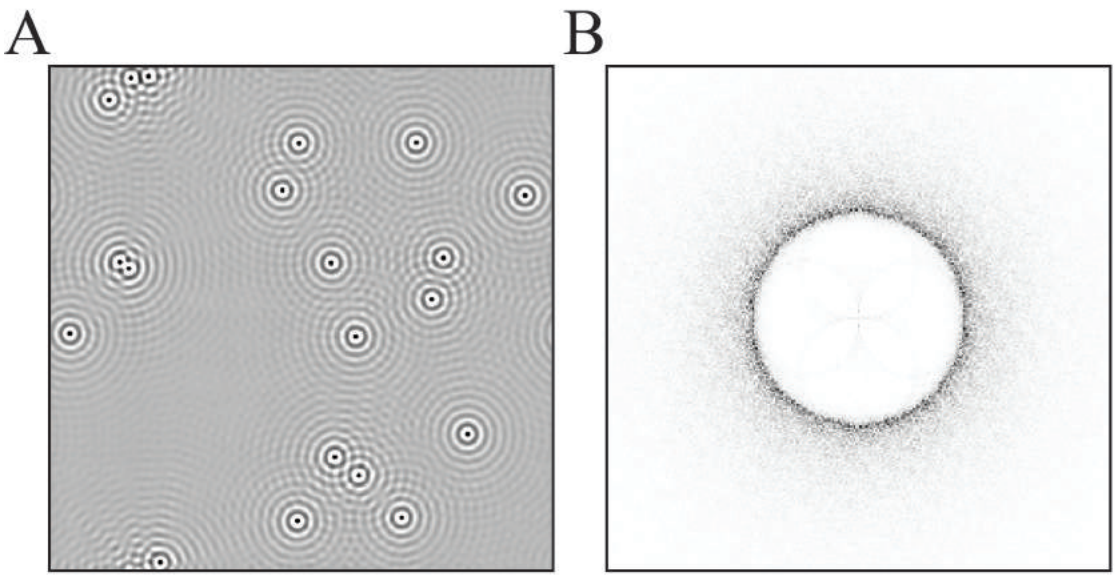

Figure 3.1: Typical quasiparticle interference pattern. A, Several randomly distributed defects create ripples in the local density of states, $\delta n(E, \vec{r})$. The calculated LDOS image at one particular energy E is shown. **B,** The amplitude of spatial Fourier transform of A, $\left|\delta n(E, \vec{q})\right|$.

Fig 3.2 illustrates how band structure can be reconstructed from QPI in the simplest case with one parabolic band. First the data, consisting of a sequence of LDOS images as function of energy, is Fourier transformed. Then the set of principle scattering wavevectors $\vec{q}(E)$ naturally determines the band dispersion $E(\vec{k})$ since $\vec{q}(E) = 2\vec{k}(E)$.

In the next section, I will look at common theoretical descriptions of QPI phenomena and derive the results that were used in the intuitive explanation above.

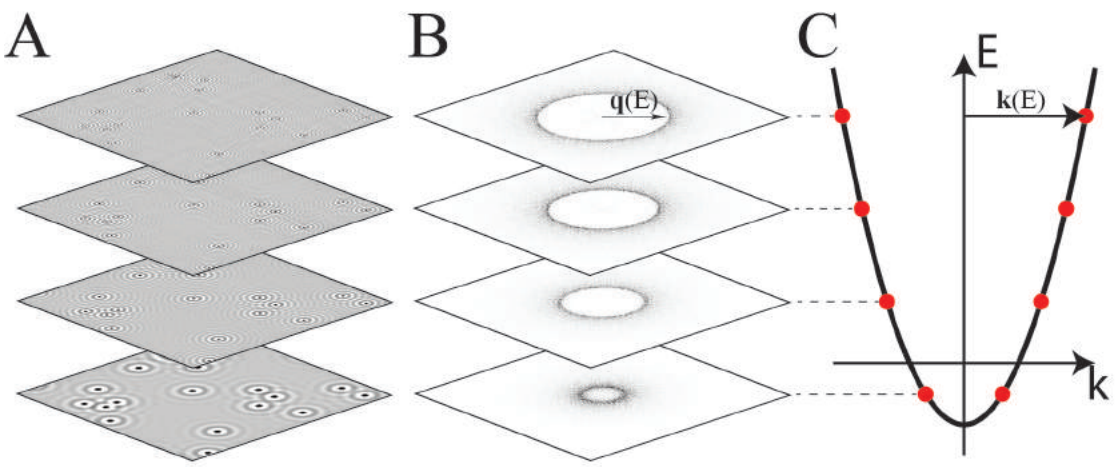

Figure 3.2: Determination of electronic structure with QPI. A, Example sequence of $\delta n(E, \vec{r})$ images as a function of energy. **B,** Corresponding sequence of $\delta n(E, \vec{q})$ images. **C,** Parabolic band used for calculating images in **A** and **B**.

3.2 Theoretical treatments

Here I review the most common methods for calculating quasiparticle interference patterns taking specific electronic structure models and impurity potential as inputs. The first approach is phenomenological and is based on the idea of the *joint density states* (JDOS). In its simplest form, JDOS postulates that $\delta n(E, \vec{q})$ is proportional to the density of pairs of states $\left(|\vec{k}_1(E)\rangle, |\vec{k}_2(E)\rangle\right)$ where $\vec{k}_1 - \vec{k}_2 = \vec{q}$. The second approach is a quantum mechanical treatment of the impurity scattering problem based on the T-matrix approximation [92, 93].

3.2.1 Joint density of states

In this section, I will motivate the JDOS approximation for calculating quasiparticle interference patterns closely following [86, 94].

In the absence of defects, I define the local density of states of the sample

$n_s(E,\vec{r})$ in terms of Bloch eigenstate wavefunctions $\psi_{\vec{k}}(\vec{r})$.

$$n_s(E,\vec{r}) = \sum_{\vec{k},\sigma} |\psi_{\vec{k}}(\vec{r})|^2 \delta(E(\vec{k}) - E) \propto \int_{\vec{k}} |\psi_{\vec{k}}(\vec{r})|^2 \delta(E(\vec{k}) - E) d\vec{k} \tag{3.2}$$

Any Bloch state associated with crystal momentum $|\vec{k}\rangle$ can be written as a sum of plane waves [91], $\psi_{\vec{k}}(\vec{r}) = \sum_{\vec{G}} a(\vec{k},\vec{G}) e^{i(\vec{k}-\vec{G})\cdot\vec{r}}$. Here the sum is over the reciprocal vectors, $\vec{G}$.

In the presence of defects, the eigenstates of the system will be modified. At the lowest order of perturbation theory, the new *perturbed* states $|\psi_{\vec{q'}}\rangle$ with energy E can be expressed in terms of linear combinations of the *unperturbed* Bloch states $|k\rangle$ with the same energy E. That is $|\psi_{\vec{q'}}\rangle = \sum_{\vec{k}\in S_E} b_{\vec{q'}}(\vec{k}) |\vec{k}\rangle$. (At this point, $\vec{q'}$ is just a label for the new states.)

$$\psi_{\vec{q'}}(\vec{r}) = \sum_{\vec{k}\in S_E,\vec{G}} a(\vec{k},\vec{G}) b_{\vec{q'}}(\vec{k}) e^{i(\vec{k}-\vec{G})\cdot\vec{r}} = \frac{1}{4\pi^2} \int_{\vec{k}\in S_E} \sum_{\vec{G}} a(\vec{k},\vec{G}) b_{\vec{q'}}(\vec{k}) e^{i(\vec{k}-\vec{G})\cdot\vec{r}} d\vec{k} \tag{3.3}$$

Here S_E is a surface of constant energy contour (i.e. set of all states with the same energy eigenvalue E). Now let's look at the local density of states, $n_s(\omega,\vec{r}) = \frac{1}{2\pi^2} \int_{\vec{q'}} |\psi_{\vec{q'}}(\vec{r})|^2 \delta(E(\vec{q'}) - E) d\vec{q'}$, in the presence of defects. The relevant quantity is the amplitude, $\langle \psi_{\vec{q'}} | \psi_{\vec{q'}} \rangle = \sum_{\vec{k},\vec{k'},\vec{G},\vec{G'}} a^*(\vec{k'},\vec{G'}) b^*_{\vec{q'}}(\vec{k'}) a(\vec{k},\vec{G}) b_{\vec{q'}}(\vec{k}) e^{i(\vec{k}-\vec{k'}+\vec{G'}-\vec{G})\cdot\vec{r}}$. Using the identity $e^{i(\vec{k}-\vec{k'}+\vec{G'}-\vec{G})\cdot\vec{r}} = \int_{\vec{q}} e^{i\vec{q}\cdot\vec{r}} \delta\left[\vec{q} - \vec{k} - \vec{k'} + \vec{G'} - \vec{G}\right] d\vec{q}$, the local density of states can be put in the following form.

$$n_s(E,\vec{r}) = \frac{1}{2\pi} \int_{\vec{q}} g(E,\vec{q}) e^{i\vec{q}\cdot\vec{r}} d\vec{q} \tag{3.4}$$

$$g(E,\vec{q}) = \int_{S_E} \int_{S_E} f(\vec{k},\vec{k'},\vec{G},\vec{G'}) \delta(\vec{q} - \vec{k} - \vec{k'} + \vec{G'} - \vec{G}) d\vec{k} d\vec{k'} \tag{3.5}$$

$$f(\vec{k},\vec{k'},\vec{G},\vec{G'}) = \frac{1}{2\pi^2} \int_{\vec{q'}} a^*(\vec{k'},\vec{G'}) b^*_{\vec{q'}}(\vec{k'}) a(\vec{k},\vec{G}) b_{\vec{q'}}(\vec{k}) d\vec{q'} \tag{3.6}$$

The function $g(E,\vec{q})$ is the inverse Fourier transform of $n_s(E,\vec{r})$. Its amplitude is the power spectrum of the modulations in the local density of states created by scattering from defects. Each pair of unperturbed states $|\vec{k}\rangle$, $|\vec{k'}\rangle$ of the

same energy can interfere with one another creating modulations at wavevector $\vec{q} = \vec{k} - \vec{k'}$ modulo reciprocal lattice vector. The information about relative amplitudes of all the modulations at various wavevectors is contained in the function $f(\vec{k}, \vec{k'}, \vec{G}, \vec{G'})$.

The simplest model for $g(E, \vec{q})$ is to take $f(\vec{k}, \vec{k'}, \vec{G}, \vec{G'})$ to be a constant function. Then $g(E, \vec{q})$ is proportional to the number of pairs of states with wavevectors differing by $\vec{q}$. The number of pairs is related to the *joint density of states* (JDOS). Hence, this simplified model is called the JDOS approximation. The wavevectors that connect large regions of constant energy contours (CEC) generate the most scattering. Such wavevectors are said to be well nested.

A schematic explanation of nesting is provided in Fig 3.3, for hexagonal and circular CECs. $\Delta\vec{k}$ is the smearing of these contours due to finite quasiparticle lifetime and thermal excitations. To evaluate the expected magnitude of QPI according to the JDOS at a specified wavevector $\vec{q}$, the replica of the contour is translated from the origin by $\vec{q}$. Then the $\vec{k}$-space overlap between the contour and its translated replica gives the desired result. The hexagonal CEC has six wavevectors - $\vec{q}_2$ and its symmetric partners - with the largest such overlap. By the same argument for the circular CEC, QPI pattern should be isotropic as a function of $\vec{q}$-space angle.

To perform calculations within the JDOS approximation, it is useful to rewrite Eq. 3.5 in the following form.

$$g(E, \vec{q}) \simeq \int A(\vec{k}, E) A(\vec{k} + \vec{q}, E) d\vec{k} \tag{3.7}$$

This form facilitates making predictions for the scattering power spectrum provided there is a model of the band structure, $E(\vec{k})$, for the material in question. $A(\vec{k}, E) = -\frac{1}{\pi} \mathrm{Im}(\mathrm{Tr}[\hat{G}(\vec{k}, E)])$ is the spectral function (also spectral density

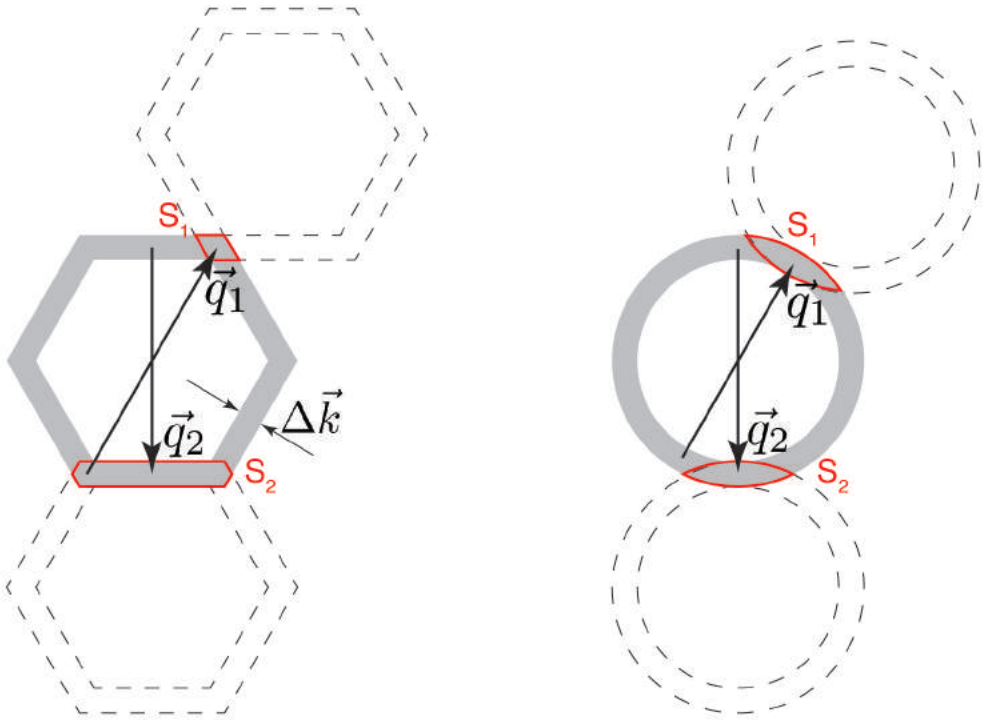

Figure 3.3: Geometrical construction illustrating nesting. The hexagonal and circular CEC (constant energy contours) are shown. $\Delta\vec{k}$ represents quasiparticle smearing due to interactions and finite temperature. In the hexagonal case, $g(E, \vec{q}_2) > g(E, \vec{q}_1)$ due to the difference in nesting. For circular CEC, there is no special direction for preferred scattering interference. Adapted from [86].

function) defined in terms of the single electron Green's function, $\hat{G}(\vec{k}, E) = ((E + i\eta)\hat{I} - \hat{H}_{\vec{k}})^{-1}$ [92]. In this context, $A(\vec{k}, E)$ can be interpreted as the density of states with crystal momentum $\vec{k}$ and energy E. Eq. 3.7 can be used to generate predictions for the quasiparticle interference patterns from the single particle Hamilitonian, $\hat{H}_{\vec{k}}$. Additionally, since $A(\vec{k}, E)$ can be taken from ARPES spectrum, JDOS connects observables from ARPES and STM experiments [95]. Fig 3.4A shows a single energy layer of $g(E, \vec{q})$ calculated for a parabolic band. A ring of scattering vectors defined by $\vec{q}(E) = 2\vec{k}(E)$ dominates the QPI pattern, and hence in this simple case constant energy contours can be visualized directly.

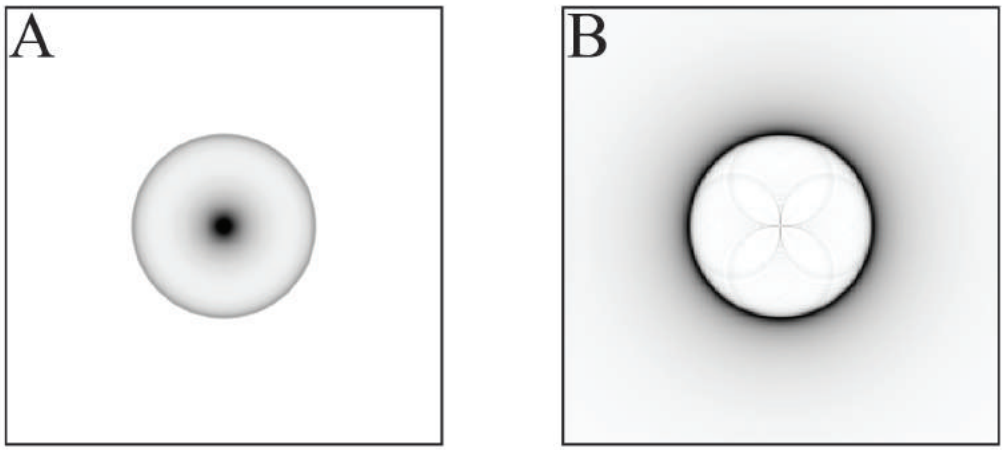

Figure 3.4: QPI pattern in Fourier space calculated for an isotropic parabolic band. A, JDOS pattern $g(\vec{q}, E)$. **B,** $\left|\delta n(\vec{q}, E)\right|$ calculated within T-matrix approximation.

Taking $f(\vec{k}, \vec{k'}, \vec{G}, \vec{G'})$ to be a constant function should be considered a phenomenological model and not a complete quantum mechanical description. In practice, this approximation is very useful for interpreting results. In the next section an alternative theoretical treatment is presented based on T-matrix calculations.

3.2.2 T-matrix approximation

I start with a multi-orbital tight-binding Hamiltonian in real space, $\hat{H}_0 = \sum_{\alpha\beta\vec{r}\vec{r'}} t_{\alpha\beta\vec{r}\vec{r'}} c^{\dagger}_{\alpha}(\vec{r}) c_{\beta}(\vec{r'})$, where α and β are orbital indices. Suppose that the material surface contains a single impurity at position, $\vec{r^*}$. The effects of this impurity can be included by adding the following impurity term to the Hamiltonian, $\hat{H}_{imp} = V_0 \sum_{\alpha} c^{\dagger}_{\alpha}(\vec{r^*}) c_{\alpha}(\vec{r^*})$. Here I assumed that the impurity term is diagonal in orbital space as well as perfectly localized meaning that the impurity density is a delta function centered at $\vec{r^*}$. Since the impurity breaks the translational

invariance, the new Green's function depends on two crystal momenta and can be expressed as a series shown in Eq. 3.8 [93].

$$\begin{aligned}\hat{G}(\vec{k},\vec{k'},E) = \hat{G}_0(\vec{k},E) + \hat{G}_0(\vec{k},E)\hat{V}_{\vec{k},\vec{k'}}\hat{G}_0(\vec{k'},E) \\ + \sum_{\vec{k''}} \hat{G}_0(\vec{k},E)\hat{V}_{\vec{k},\vec{k''}}\hat{G}_0(\vec{k''},E)\hat{V}_{\vec{k''},\vec{k'}}\hat{G}_0(\vec{k'},E) + ...\end{aligned} \tag{3.8}$$

The series can be summed defining the T-matrix, $\hat{T}_{\vec{k},\vec{k'}}$.

$$\hat{G}(\vec{k},\vec{k'},E) = \hat{G}_0(\vec{k},E) + \hat{G}_0(\vec{k},E)\hat{T}_{\vec{k},\vec{k'}}(E)\hat{G}_0(\vec{k'},E) \tag{3.9}$$

$$\begin{aligned}\hat{T}_{\vec{k},\vec{k'}}(E) &= \hat{V}_{\vec{k},\vec{k'}} + \sum_{\vec{k''}} \hat{V}_{\vec{k},\vec{k''}}\hat{G}_0(\vec{k''},E)\hat{V}_{\vec{k''},\vec{k'}} + ... \\ &= \hat{V}_{\vec{k},\vec{k'}} + \sum_{\vec{k''}} \hat{V}_{\vec{k},\vec{k''}}\hat{G}_0(\vec{k''},E)\hat{T}_{\vec{k''},\vec{k'}}(E)\end{aligned} \tag{3.10}$$

The equation 3.10 needs to be solved for $\hat{T}_{\vec{k},\vec{k'}}$. Since for a perfectly localized impurity $\hat{V}_{\vec{k},\vec{k'}} = V_0\hat{I}$ ($\hat{I}$ is the identity matrix), the solution has a closed form.

$$\hat{T}(E) = V_0\hat{I}[\hat{I} - V_0\sum_{\vec{k}} \hat{G}_0(\vec{k},E)]^{-1} \tag{3.11}$$

Finally, the perturbation to the LDOS in $\vec{q}$-space is easily obtained.

$$\delta n(E,\vec{q}) = -\frac{1}{\pi}\,\mathrm{Im}\,\mathrm{Tr}\sum_{\vec{k}} \hat{G}_0(\vec{k},E)\hat{T}(E)\hat{G}_0(\vec{k}+\vec{q},E) \tag{3.12}$$

One further simplify Eq. 3.12 if the impurity potential is very small. In the limit $V_0 \to 0$, the T-matrix becomes proportional to identity resulting in the expression below.

$$\delta n_s(E,\vec{q}) = -\frac{V_0}{\pi}\,\mathrm{Im}\,\mathrm{Tr}\sum_{\vec{k}} \hat{G}_0(\vec{k},E)\hat{G}_0(\vec{k}+\vec{q},E) \tag{3.13}$$

Fig. 3.4B shows a single energy layer of $\left|\delta n_s(E,\vec{q})\right|$ calculated for a parabolic band and a single impurity at the origin. For a single band calculation the result is very similar to JDOS. The scattering from $\vec{k}$ to -$\vec{k}$ is dominant as expected from the JDOS calculation. Note that the T-matrix method calculates only the

perturbation to the density of states, and hence the corresponding QPI patterns do not have contributions at $\vec{q} = 0$.

It is worthwhile to compare the two approximation schemes $\delta n_s(E, \vec{q})$ and $\delta n_{JDOS}(E, \vec{q}) = \frac{V_0}{\pi} \sum_{\vec{k}} \mathrm{Im}(\mathrm{Tr}\, \hat{G}_0(\vec{k}, E)) \,\mathrm{Im}(\mathrm{Tr}\, \hat{G}_0(\vec{k} + \vec{q}, E))$ from the last section. In the T-matrix approximation, there is a full matrix product of Green's functions under the summand. In JDOS approach, the off-diagonal elements in G_0's are ignored, and only the spectral densities (i.e. $A = \mathrm{Tr}(G_0)$) are used.

In the language of elementary quantum mechanics, the matrix products in equations 3.12 and 3.13 include the effect of quantum overlaps between scattered states, $\langle \alpha; \vec{k} | \hat{T} | \beta; \vec{k'} \rangle$. Since the Hamiltonian, $\hat{H}_k$, is in general a matrix containing orbital and spin degrees of freedom, α and β are included as eigenvector labels containing band indices and spin indices if relevant. These overlaps can be small for some pairs of states on a given CEC, resulting in suppressed scattering at the corresponding $\vec{q}$ wavevectors.

A specific case where these considerations are important is STM studies of spin textured systems like topological insulators [96]. If the scatterer is non-magnetic, it preserves spin ($\langle \uparrow | \hat{T} | \downarrow \rangle = 0$). In the systems discussed, the spin of the quasiparticle at $\vec{k}$ is opposite to the spin of the quasiparticle at $-\vec{k}$. Hence, the usually dominant intraband scattering across a Fermi pocket with wavevector $\vec{q} = 2\vec{k}$ is completely suppressed. In the JDOS calculation, however, such suppression would not be observed.

3.2.3 Computation of normalized conductance

In section 2.2.3, the normalized conductance or Feenstra parameter, $L(V, \vec{r})$, was introduced as a way of defining conductance maps that are experimentally accessible and independent from the setup current and voltage. Here I discuss a theoretical calculation of $L(E, \vec{r})$ and its Fourier transform, $L(E, \vec{q})$.

Recall from Eq. 2.13, that $L(E, \vec{r})$ is the following function of the local density of states .

$$L(E, \vec{r}) = E \frac{n(E, \vec{r})}{\int_0^E n(E', \vec{r}) dE'} \tag{3.14}$$

In the previous section, it was shown how the power spectrum of perturbations to the local density of states arising from defect scattering, $\delta n(E, \vec{q})$, can be computed using the T-matrix formalism. The Fourier transform of the Feenstra parameter can be numerically constructed from $\delta n(E, \vec{q})$ using the following sequence of steps.

First the inverse Fourier transform of $\delta n(E, \vec{q})$ is calculated to go to real space.

$$\delta n(E, \vec{r}) = \sum_{\vec{q}} e^{i\vec{q}\cdot\vec{r}} \delta n(E, \vec{q}) \tag{3.15}$$

Next the uniform component of the density of states is added to the perturbed one.

$$n(E, \vec{r}) = n_0(E) + \delta n(E, \vec{r}) = \frac{1}{\pi} \mathrm{Tr}[\mathrm{Im} \sum_{\vec{k}} G_0(\vec{k}; E)] + \delta n(E, \vec{r}) \tag{3.16}$$

Then the Feenstra function is calculated in real space.

$$L(E, \vec{r}) = E \frac{n(E, \vec{r})}{\sum_0^E n(E', \vec{r})} \tag{3.17}$$

Finally $L(E, \vec{r})$ is Fourier transformed.

$$L(E, \vec{q}) = \sum_{\vec{r}} e^{-i\vec{q}\cdot\vec{r}} L(E, \vec{r}) \tag{3.18}$$

CHAPTER 4

ORBITAL-SELECTIVE QUASIPARTICLE INTERFERENCE PATTERNS IN FeSe

In Chapter 1, I discussed correlations in the multi-orbital context of iron-based superconductors. Theoretical arguments, based on the numerical studies of the multi-orbital Hubbard model, suggest that FeSCs are generally Hund's metals - correlated metals where Hund's coupling leads to orbital decoupling of charge excitations. This decoupling, in combination with the lifting of orbital degeneracy due to crystal field splitting and nematic ordering, leads to orbital selectivity of electronic correlations. This orbital selectivity manifests itself in the orbital dependence of mass renormalizations and quasiparticle weights. In this chapter, I show that the orbital anisotropy of quasiparticle weights naturally leads to orbital-selective quasiparticle interference. Then I use this idea to analyze the STM measurements of quasiparticle interference patterns in the nematic phase of FeSe and show that these measurements establish the existence of strong orbital selectivity of correlations in this system.

4.1 Quasiparticle interference and orbital-selective correlations

In this section, I will consider the effects of orbital-selective correlations on calculations of quasiparticle interference patterns.

4.1.1 Orbital-Selective Ansatz

Suppose that the electronic structure of a multiband system under investigation is well described by a tight-binding Hamiltonian, $H = \sum_{\vec{k},s,s'} t_{\vec{k}}^{ss'} c_s^\dagger(\vec{k}) c_{s'}(\vec{k})$, where $t_{\vec{k}}^{ss'}$ is the Fourier transform of the hopping parameters, $t_{\vec{r}-\vec{r}'}^{ss'}$, and $c_s^\dagger(\vec{k})$ creates an electron in Wannier orbital s with wavevector $\vec{k}$. We can go from orbital to band space by diagonalizing the Hamiltonian via a unitary transformation to obtain $H = \sum_{\vec{k},\mu} E_\mu(\vec{k}) c_\mu^\dagger(\vec{k}) c_\mu(\vec{k})$, where $E_\mu(\vec{k})$ gives the dispersion of band μ, and $c_\mu^\dagger(\vec{k})$ creates an electron in Bloch state $|\mu\vec{k}\rangle$. Note that Greek indices label bands, while Roman indices label orbitals.

If the hoppings, $t_{\vec{r}-\vec{r}'}^{ss'}$, are adjusted to match the dispersions acquired from the experiments probing the band structure (i.e. ARPES, SI-STM, de Haas-van Alphen effect), then H includes some effects of correlations (due to electron-electron interactions) since correlations lead to band renormalizations. However, this simple model gives no information contained in the quasiparticle self-energy such as quasiparticle weights and lifetimes. Here the term *uncorrelated* will be used for systems where quasiparticles have unit weight even if the model H produces experimentally deduced "correlated" dispersions.

In the band basis, the uncorrelated retarded Green's function at energy ω and wavevector $\vec{k}$ is simply a diagonal matrix given by $G_\mu^R(\vec{k},\omega) = \frac{1}{\omega - E_\mu(\vec{k}) + i\Gamma_\mu(\vec{k})}$. The matrix elements $a_\mu^s(\vec{k})$ of the unitary transformation diagonalizing the tight binding Hamiltonian connect band and orbital basis operators (i.e. $c_s(\vec{k}) = \sum_\mu a_\mu^s(\vec{k}) c_\mu(\vec{k})$). The same basis transformation can be used to write the Green's function in orbital space as follows [51].

$$G_{ss'}^R(\vec{k},\omega) = \sum_\mu a_\mu^s(\vec{k}) a_\mu^{s'}(\vec{k})^* G_\mu^R(\vec{k},\omega) = \sum_\mu \frac{a_\mu^s(\vec{k}) a_\mu^{s'}(\vec{k})^*}{\omega - E_\mu(\vec{k}) + i\Gamma_\mu(\vec{k})} \tag{4.1}$$

Now we can introduce correlations by using the following orbital-selective (OS) ansatz introduced in [51]. The density operator $c_l^\dagger(\vec{k})c_l(\vec{k})$ will now refer to quasiparticles with quasiparticle weight Z_s in orbital s implying the replacement $c_s^\dagger(\vec{k}) \rightarrow \sqrt{Z_s}c_s^\dagger(\vec{k})$. The corresponding Green's function then becomes

$$\tilde{G}^R_{ss'}(\vec{k},\omega) = \sqrt{Z_s Z_{s'}} \sum_\mu \frac{a^s_\mu(\vec{k}) a^{s'}_\mu(\vec{k})^*}{\omega - E_\mu(\vec{k}) + i\Gamma_\mu(\vec{k})} = \sqrt{Z_s Z_{s'}} G^R_{ss'}(\vec{k},\omega) \tag{4.2}$$

The Green's function $\tilde{G}^R(\vec{k},\omega)$ has been "dressed" with quasiparticle weights. The coherent part of the associated spectral function reveals the effects of the proposed ansatz in band space.

$$\begin{aligned}
\tilde{A}(\vec{k},\omega) &= -\frac{1}{\pi}\,\mathrm{Im}\,\mathrm{Tr}\,\tilde{G}^R(\vec{k},\omega) = -\frac{1}{\pi}\,\mathrm{Im}\sum_s \tilde{G}^R_{ss}(\vec{k},\omega) \\
&= -\frac{1}{\pi}\,\mathrm{Im}\sum_s Z_s \sum_\mu \frac{a^s_\mu(\vec{k}) a^s_\mu(\vec{k})^*}{\omega - E_\mu(\vec{k}) + i\Gamma_\mu(\vec{k})} \\
&= -\frac{1}{\pi}\,\mathrm{Im}\sum_\mu \frac{\sum_s Z_s |a^s_\mu(\vec{k})|^2}{\omega - E_\mu(\vec{k}) + i\Gamma_\mu(\vec{k})} \\
&= -\frac{1}{\pi}\,\mathrm{Im}\sum_\mu \frac{Z_\mu(\vec{k})}{\omega - E_\mu(\vec{k}) + i\Gamma_\mu(\vec{k})}
\end{aligned} \tag{4.3}$$

Here $Z_\mu(\vec{k}) \equiv \sum_s Z_s |a^s_\mu(\vec{k})|^2$ gives the contribution of a given band to the spectral function. The interacting Green's function can be expressed in the standard form $\tilde{G}_\mu(\vec{k},\omega) = \frac{1}{\omega - E_\mu(\vec{k}) - \Sigma_\mu(\vec{k},\omega)}$ where $\Sigma_\mu(\vec{k},\omega)$ is the self-energy. The quasiparticle weight $Z_\mu(\vec{k})$ can be deduced from $\Sigma_\mu(\vec{k},\omega)$ which is a complex function containing the information about interactions in the system (refer to Section 1.2). The relevant expression is provided below.

$$Z_\mu(\vec{k}) = \left(1 - \frac{\partial}{\partial\omega}\,\mathrm{Re}\,\Sigma_\mu(\vec{k},\omega)\Big|_{\omega=0}\right)^{-1} \tag{4.4}$$

The quasiparticle weight is strictly defined only at the chemical potential. Note since the energy ω is measured from the chemical potential, the partial derivative of the self-energy is evaluated at the chemical potential (i.e $\omega = 0$).

In the next section, I will discuss how correlations modify the quasiparticle interference patterns in the FeSe system where it has been proposed that OS ansatz is relevant [1,51]. Through the "dressed" Green's functions, the quasiparticle weights Z_s enter the calculation of the perturbation to the density of states caused by QPI (see Eq. 3.12). As a result, QPI amplitudes in $\vec{q}$ space are modified in the correlated system in such a way that more coherent orbitals (i.e. with greater quasiparticle weight) produce a greater scattering response compared to more correlated orbitals.

4.1.2 Application to the Nematic State of FeSe

Let us consider the orbital-selective ansatz in the context of the nematic state of FeSe. As discussed in the introduction of this thesis, the associated band structure of this state is accurately parameterized by the five orbital model described in Section 1.3.1. Assuming all quasiparticles are equally coherent, the spin susceptibility calculated for this band structure model peaks at the wavevector $(\frac{\pi}{a_{Fe}}, \frac{\pi}{b_{Fe}})$ [51]. Contrary to this, inelastic neutron-scattering (INS) experiments have found a transfer of spectral weight from the Néel $((\frac{\pi}{a_{Fe}}, \frac{\pi}{b_{Fe}}))$ to the stripe $((\frac{\pi}{a_{Fe}}, 0)$ or $(0, \frac{\pi}{b_{Fe}}))$ spin fluctuations in FeSe on entering the nematic phase [61,62]. Moreover, the specific variation of the superconducting gap magnitude on two Fermi pockets, deduced from a Bogoluibov quasiparticle interference (BQPI) experiment [1], is inconsistent with the itinerant weak coupling spin-fluctuation theory calculations (described in [4, 97]) if $(\frac{\pi}{a_{Fe}}, \frac{\pi}{b_{Fe}})$ fluctuations are dominant.

If orbital-selective correlations are present in the nematic state of FeSe, these

experiments can still be consistent with the spin-fluctuation based pairing. The introduction of quasiparticle weights into the definitions of susceptibility and pairing vertex includes these correlations into the theory. The specific values $(Z_{xy}, Z_{x^2-y^2}, Z_{xz}, Z_{yz}, Z_{z^2}) = (0.073, 0.94, 0.16, 0.85, 0.36)$ were used to fit the gap symmetry function calculated within spin-fluctuation theory to experiment by Kreisel *et al.* [51], although calculations are mostly only sensitive to the values of (Z_{xy}, Z_{xz}, Z_{yz}) since the relevant electronic structure close to chemical potential is dominated by (d_{xy}, d_{xz}, d_{yz}) orbitals. The important results of the BQPI study mentioned above are: (i) the gap on the Fermi surface is largest at those $\vec{k}$-points where the d_{yz} orbital content (i.e. $|a_\mu^{yz}(\vec{k})|^2$) is large, (ii) the gap is largest on the α pocket centered at $(0,0)$ point of the Brillouin zone, (iii) no gap was detected on the δ pocket centered at $(0, \frac{\pi}{b_{Fe}})$. Kreisel *et al.* have found that calculations are consistent with experimental data for a range of Z_s values as long as $Z_{yz} \gg Z_{xz} > Z_{xy}$. Moreover, if quasiparticle weights indeed follow this proposed hierarchy, the calculated spin susceptibility is now peaked at $(\frac{\pi}{a_{Fe}}, 0)$ which agrees with strong stripe fluctuations revealed by inelastic neutron scattering. It is worth mentioning that INS measurements on detwinned crystals of FeSe would be a more stringent test of proposed orbitally selective correlations since they would distinguish between $(\frac{\pi}{a_{Fe}}, 0)$ and $(0, \frac{\pi}{b_{Fe}})$ spin fluctuations. Nevertheless, the orbital-selective ansatz in nematic FeSe is well motivated by existing experiments.

In order to visualize the variation of quasiparticle weight in $\vec{k}$-space, we first compute $Z_\mu(\vec{k}) = \sum_s Z_s |a_\mu^s(\vec{k})|^2$ using the Z_s values listed above and the matrix elements, $a_\mu^s(\vec{k})$, of a unitary transformation that diagonalizes the five orbital tight binding Hamiltonian (section 1.3.1). Then $Z_\mu(\vec{k})$ is used to shade $E_\mu(\vec{k})$ points in such a way that less coherent states are represented by fainter (more transpar-

ent) colors. The chromaticity of each colored point displays the orbital content of the corresponding state with red, green and blue colors assigned to d_{xz}, d_{yz} and d_{xy} orbitals, respectively. The result is shown in the figure 4.1.

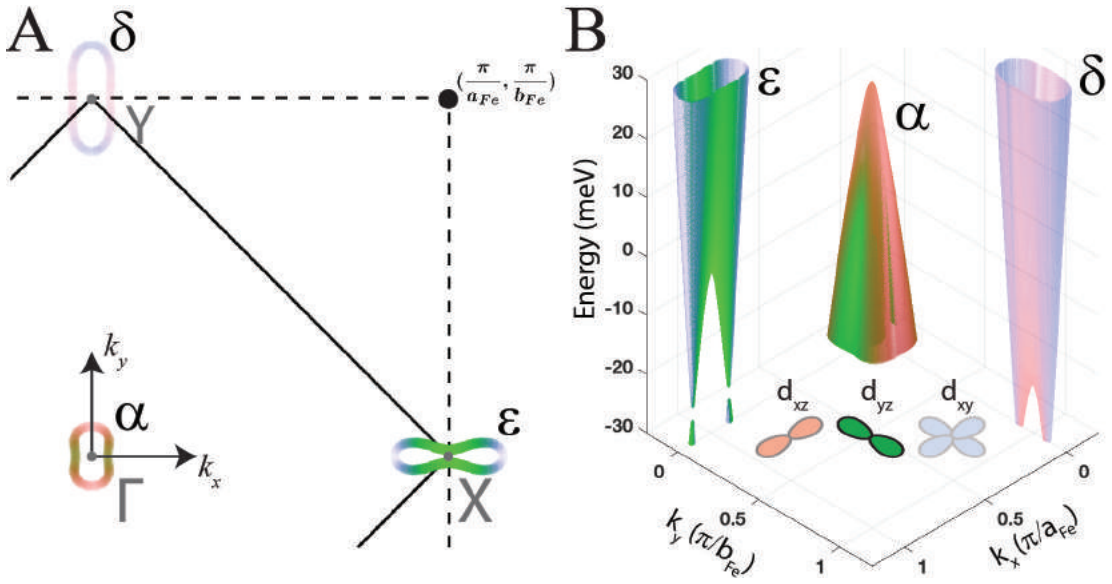

Figure 4.1: Model of electronic structure in nematic phase of FeSe incorporating orbital-selective ansatz. **A,** Sketch of orbital-selective correlations on Fermi surface contour at $k_z = 0$. The color transparency represents quasiparticle weight with the faint colors showing $\vec{k}$ states with low $Z_\mu(\vec{k})$ defined by Eq. 4.4. The specific values of (Z_{xy}, Z_{xz}, Z_{yz}) were taken from [51] to be $(0.07, 0.16, 0.85)$. **B,** Proposed "correlated" $k_z = 0$ electronic structure of FeSe nematic state.

This orbital-selective picture can explain why detwinned APRES studies [69, 70] have not observed any spectral weight in the vicinity of $(0, \frac{\pi}{b_{Fe}})$ point, the expected location of the δ-band.

4.1.3 Predicted Band Resolved Quasiparticle Interference with and without Quasiparticle Weights

Having introduced the orbital-selective ansatz, I are ready to discuss predictions of quasiparticle interference patterns in systems with orbital-selective correlations. The nematic phase of FeSe will be used as an example.

Just below the chemical potential, the band structure is dominated by the hole-like α-band of d_{yz} and d_{xz} orbital characters, and the electron-like bands occupy substantially smaller $\vec{k}$-space volumes. Fig. 4.2A shows the orbitally-resolved constant-energy-contour (CEC) of the α-band, $\vec{k}_\alpha(E)$ at $E = -10$ meV. Fig. 4.2C then shows the corresponding intraband QPI intensity pattern, $|\delta n_\alpha(\vec{q}, E = -10\,\text{meV})|$, calculated using the T-matrix approximation (section 3.2.2) assuming fully coherent quasiparticles ($Z_s = 1$ for all orbitals). Note that the $|\delta n_\alpha(\vec{q}, E)|$ image contains a closed contour corresponding to $\vec{q}_\alpha(E) = 2\vec{k}_\alpha(E)$ scattering (i.e. intraband scattering across the pocket) that typically dominates QPI patterns. The scattering intensity is bigger closer to q_x axis due to better nesting since the pocket is elongated, but there is a substantial signal at all angular directions.

Fig. 4.2B also shows the orbitally-resolved CEC of the α-band at $E = -10$ meV but now with $Z_\mu(\vec{k})$ shading described in previous section. The quasiparticle weights describing orbital-selective correlations are the same as before $Z_s = (0.073, 0.94, 0.16, 0.85, 0.36)$ as introduced in [1, 51]. These values will be used for all subsequent simulations of QPI for orbital-selective quasiparticles (OSQP). Fig. 4.2D then shows the corresponding T-matrix calculation of $|\delta n_\alpha(\vec{q}, E = -10\,\text{meV})|$ using the "dressed" Green's function $\tilde{G}^R_{ss'}(\vec{k}, E) =$

$\sqrt{Z_s Z_{s'}} G^R_{ss'}(\vec{k}, E)$ (section 4.1.1). Here the scattering between states of predominantly d_{xz} orbital character with a smaller quasiparticle weight is strongly suppressed. The QPI intensity viewed as a function of the $\vec{q}$-space angle is strongly anisotropic with a maximum near the q_x axis and almost no signal near the q_y axis.

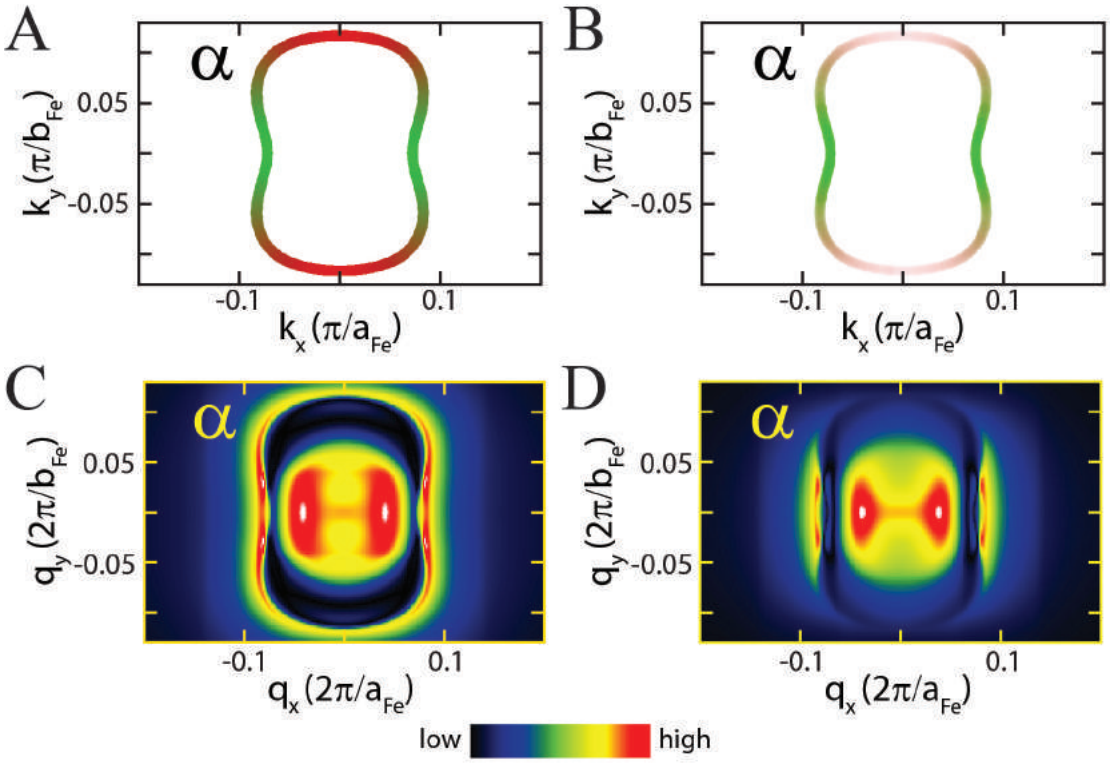

Figure 4.2: Predicted intraband quasiparticle interference pattern for the α band. **A,** Constant energy ($E = -10$ meV) contour for the α band, $\vec{k}_\alpha(E = -10 \text{ meV})$, at the Γ-point (0,0) plotted using the "uncorrelated" color code from Fig. 1.12. **B,** Constant energy contour for the α band at the Γ-point (0,0) using the "correlated" color code from Fig. 4.1. **C,** Calculated $\delta n_\alpha(E = -10 \text{ meV}, \vec{q})$ with $Z_s = 1$. **D,** Calculated $\delta n_\alpha(E = -10 \text{ meV}, \vec{q})$ with $(Z_{xy}, Z_{xz}, Z_{yz}) = (0.07, 0.16, 0.85)$. The calculations in panels **C** and **D** are done using T-matrix approach with weak impurity potential ($V_{imp} \sum_{\vec{k}} \hat{G}_0(\vec{k}, E) \ll 1$) introduced in Section 3.2.2. In the calculations, the $\vec{k}$ sum was restricted to the small region surrounding Γ-point of the Brillouin zone to only include intraband scattering from the α band. That is $\delta n_\alpha(E, \vec{q}) = \frac{V_{imp}}{\pi} \sum_{|\delta\vec{k}|<\frac{\pi}{4}} \hat{G}_0(\vec{\Gamma} + \delta\vec{k}; E)\hat{G}_0(\vec{\Gamma} + \delta\vec{k} + \vec{q}; E)$.

Likewise, since the α-band closes around $E = +15$ meV, above the chemical

potential, the band structure is dominated by the electron-like ε-band of the d_{xy} and d_{yz} orbital characters and the electron-like δ band of d_{xy} and d_{xz} orbital characters. Fig. 4.3A shows the orbitally-resolved constant-energy-contour (CEC) of the ε-band, $\vec{k}_\varepsilon(E)$, at $E = +10$ meV. Fig. 4.3C then shows the corresponding intraband QPI intensity pattern, $|\delta n_\varepsilon(\vec{q}, E = +10 \text{ meV})|$, calculated using the T-matrix approximation assuming fully coherent quasiparticles ($Z_s = 1$ for all orbitals). The intraband scattering across the pocket from $\vec{k}_\varepsilon(E)$ to $(\frac{2\pi}{a_{Fe}}, 0) - \vec{k}_\varepsilon(E)$ is clearly visible. The primary scattering vectors follow $\vec{q}_\varepsilon(E) = 2\vec{k}_\varepsilon(E) - (\frac{2\pi}{a_{Fe}}, 0)$ since the ε-band is centered at $(\frac{\pi}{a_{Fe}}, 0)$. Unlike the α-band case (Fig. 4.2C), here there is a strong suppression of QPI at some angles so that the scattering pattern does not form a closed contour. This suppression is a consequence of the multi-orbital nature of the problem and will be briefly discussed in the next section. Fig. 4.3B shows the orbitally-resolved CEC of the ε-band at $E = +10$ meV with $Z_\mu(\vec{k})$ shading. Note the strong suppression of spectral weight for the states of the d_{xy} orbital character close to the k_x axis. Fig 4.3D then shows the corresponding T-matrix calculation within the orbital-selective ansatz (with "dressed" Green's function). Again the QPI intensity in the orbital-selective scenario is strongly anisotropic as a function of angle with the maximum near the q_y axis and no signal near the q_x axis. The two calculations in Fig. 4.3C and Fig. 4.3D differ by the presence of scattering along the q_x axis.

The discussion above demonstrates that orbital-selective correlations can produce additional anisotropy to quasiparticle interference patterns on top of what is generated by band structure properties (i.e. nesting and Fermi velocity). The more correlated states with lower quasiparticle weights produce less scattering than the less correlated ones. This fact opens the possibility of using spectroscopic imaging STM to identify systems containing orbital-selective

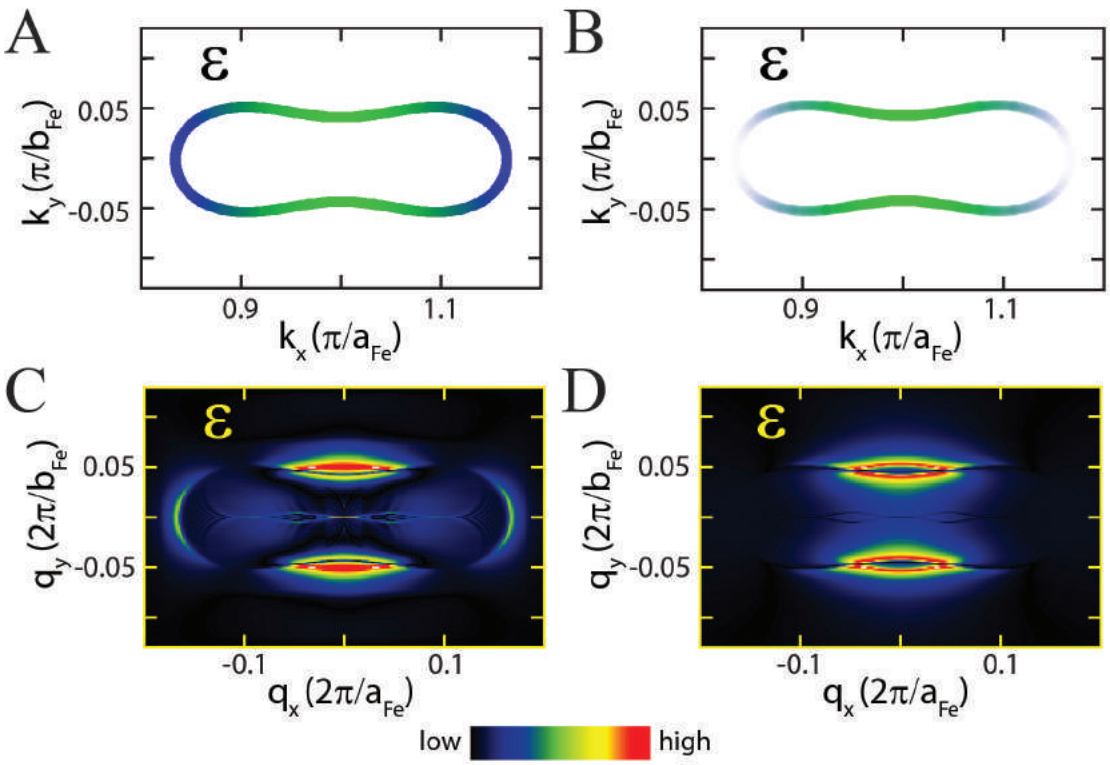

Figure 4.3: Predicted intraband quasiparticle interference pattern for the ε band. **A,** Constant energy ($E = +10$ meV) contour for the ε band, $\vec{k}_\varepsilon(E = +10\,\text{meV})$, at the X-point $(\frac{\pi}{a_{Fe}}, 0)$ plotted using the "uncorrelated" color code from Fig. 1.12. **B,** Constant energy contour for the ε band at the X-point $(\pi,0)$ using the "correlated" color code from Fig. 4.2. **C,** Calculated $\delta n_\varepsilon(E = +10\,\text{meV}, \vec{q})$ with $Z_s = 1$. **D,** Calculated $\delta n_\varepsilon(E = +10\,\text{meV}, \vec{q})$ with $(Z_{xy}, Z_{xz}, Z_{yz}) = (0.07, 0.16, 0.85)$. All comments about the calculations at the end of the caption of Fig. 4.2 apply, but the $\vec{k}$ sum is different, $\delta n_\varepsilon(E, \vec{q}) = \frac{V_{imp}}{\pi} \sum_{|\delta\vec{k}|<\frac{\pi}{4}} \hat{G}_0(\vec{X}+\delta\vec{k}; E)\hat{G}_0(\vec{X}+\delta\vec{k}+\vec{q}; E)$

physics. Later in this chapter, STM $\frac{dI}{dV}$ data will be used to argue that the nematic state of FeSe is such a system.

4.1.4 Quasiparticle Interference in Multi-orbital Systems

This section discusses general properties of quasiparticle interference (QPI) in the multi-orbital context.

Suppose we consider elastic scattering between two energy eigenstates $|\Psi\rangle$ and $|\Phi\rangle$ of the unperturbed Hamiltonian $\hat{H}_0$. The scattering amplitude should be proportional to $\langle\Psi|\hat{H}_{imp}|\Phi\rangle$ where $\hat{H}_{imp}$ is a perturbing term of the full Hamiltonian describing an impurity. The magnitude of $\langle\Psi|\hat{H}_{imp}|\Phi\rangle$ is important in calculations of predicted QPI patterns and interpretation of QPI experiments.

One example of this phenomenology is the absence of backscattering in QPI for the boundary states present on the surface of topological insulators if scatterers are non-magnetic [96]. These boundary states have a chiral spin texture where the states of opposite crystal momentum have opposite spin. If the impurity term in the Hamiltonian is diagonal in spin space, $\langle\vec{k};\uparrow|\hat{H}_{imp}|-\vec{k};\downarrow\rangle = 0$ and backscattering is prohibited. In the previous chapter, it is mentioned that scattering between $|\vec{k}\rangle$ and $|-\vec{k}\rangle$ at $\vec{q} = 2\vec{k}$ typically dominates QPI. However, in the current context this statement is maximally violated due to the specific configuration of the spin degrees of freedom. Note that if impurities are magnetic (e.g. chromium dopants), quasiparticle interference between the states of opposite momentum is expected and observed [98].

A similar suppression of QPI for certain wavevectors can happen because of the orbital degrees of freedom. In the multi-orbital system, we model a localized impurity at $\vec{r^*}$ by adding the following term to the Hamiltonian, $\hat{H}_{imp} = V_0 \sum_\alpha c^\dagger_\alpha(\vec{r^*}) c_\alpha(\vec{r^*})$ (see section 3.2.2). Here the impurity potential is assumed to be proportional to the identity in orbital space meaning that the impurity does not preferentially scatter states depending on their orbital content. Suppose we consider elastic scattering between two energy eigenstates $|\vec{k}_n\rangle$ and $|\vec{k}_m\rangle$. If $|n\rangle$ and $|m\rangle$ are the corresponding eigenvectors in orbital space, the scattering amplitude should be proportional to the overlap $\langle n|m\rangle$. Hence there can

be anisotropy in the QPI pattern corresponding to the variation of $\langle n|m\rangle$ along a constant energy contour.

Let's continue this discussion in the context of the tight-binding parameterization for the nematic state of FeSe (section 1.3.1). Fig. 4.4A shows constant energy contour at $E = -20$ meV for the α-band shaded using the amplitude of the inner product, $|\langle n|m\rangle|$, where $|n\rangle$ and $|m\rangle$ are the eigenvectors in orbital space of two states on diagonally opposite $\vec{k}$ points. Fig. 4.4B clearly shows that the variation of $|\langle n|m\rangle|$ as a function of angle in $\vec{k}$-space is small. Unsurprisingly, the corresponding T-matrix calculation of intraband quasiparticle interference for the α-band shows a closed $\vec{q}(E) = 2\vec{k}(E)$ contour without any obvious suppression of scattering at any angle. Fig. 4.4D shows constant energy contour ($E = +20$ meV) for the ε-band shaded analogously with Fig 4.4A. Fig. 4.4E demonstrates that the variation of $|\langle n|m\rangle|$ as a function of the $\vec{k}$-space angle is substantial. The corresponding calculated intraband QPI signal for the ε-band is very anisotropic and goes to zero at the angle where $|\langle n|m\rangle|$ vanishes as expected (Fig 4.4F). This example demonstrates that in multi-orbital systems, the eigenvectors can have an important effect on quasiparticle interference.

Since the goal of this chapter is to demonstrate that in FeSe the anisotropy of QPI signals detected is most consistent with the presence of orbital-selective correlations, it is important to argue why some specific variation of orbital eigenvector components along the electronic structure cannot fully account for the STM measurements. If two states on diagonally opposite $\vec{k}$ points are dominated by a single orbital, the inner product of their orbital eigenvectors cannot be small. As apparent from Fig. 4.2A and Fig 4.3A, this is true for states lying on major symmetry axis. Therefore, in later sections, data along these axis

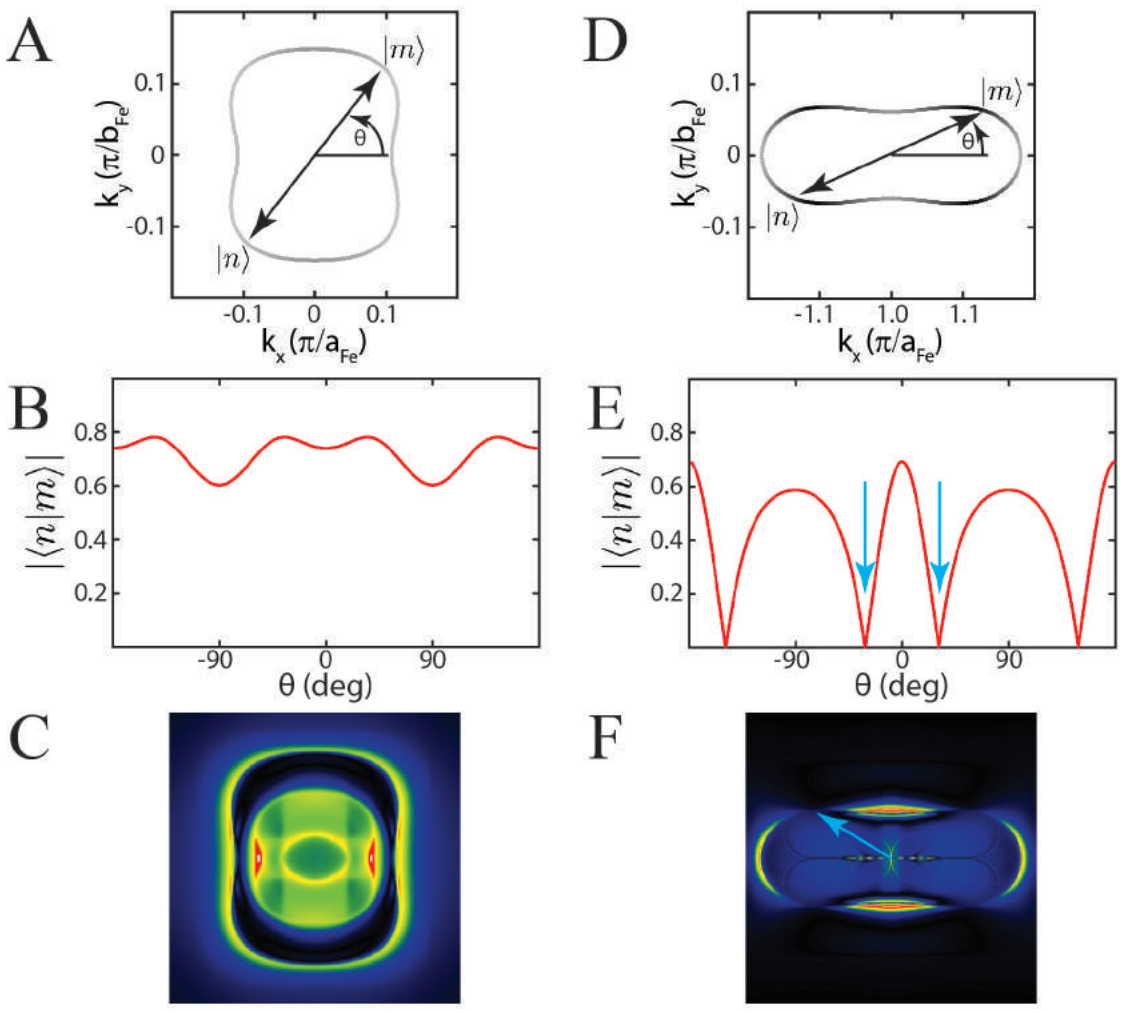

Figure 4.4: Multi-orbital quasiparticle interference. **A,** Constant energy contour for the α band, $\vec{k}_\alpha(E = -20\text{ meV})$. The grayscale color code is used to represent the variation of the quantum overlap $|\langle n|m\rangle|$ where $|n\rangle$ and $|m\rangle$ are two states on the diagonally opposite points on the contour. Darker shade means smaller $|\langle n|m\rangle|$. **B,** Plot of $|\langle n|m\rangle|$ for the $\vec{k}_\alpha(E = -20\text{ meV})$ as a function of angle labelled in A. The result is quite isotropic. **C,** $|\delta n_\alpha(E = -20\text{ meV}, \vec{q})|$, QPI pattern calculated within T-matrix approximation ($Z_s = 1$). The contour of high QPI intensity is closed which is consistent with B. **D,** Constant energy contour for the ε band, $\vec{k}_\varepsilon(E = +20\text{ meV})$ with the same shading as in A. **E,** Plot of $|\langle n|m\rangle|$ for the $\vec{k}_\varepsilon(E = +20\text{ meV})$ as a function of angle labelled in D. The result is extremely anisotropic and in fact vanishes at some angles marked by blue vertical arrows. **F,** $|\delta n_\varepsilon(E = +20\text{ meV}, \vec{q})|$, QPI pattern calculated within T-matrix approximation ($Z_s = 1$). The calculated QPI signal vanishes at angles where $|\langle n|m\rangle|$ goes to 0.

will be used to elucidate the effect of orbital-selective correlations on detected quasiparticle interference.

4.2 Methods and Materials

In the subsequent sections of the current chapter, I will present SI-STM measurements of the nematic state of bulk FeSe. Here I provide the experimental methodology used in the search of orbital-selective quasiparticle interference phenomena.

High quality single crystals FeSe were grown using $KCl/AlCl_3$ chemical vapor transport [99] and subsequently thoroughly characterized by resistivity, DC magnetization and high energy x-ray diffraction measurements [54, 58, 99, 100]. The structural transition temperatures T_s were in the range 87-89 K, and the superconducting transition temperatures T_c were 8.7-8.8 K. Crystals closest to the ideal shape and dimension (1 mm by 1 mm square) were chosen for SI-STM experiments. The selected crystal was glued onto a brass sample stud using silver epoxy. Then a brass or aluminum cleaving rod of diameter slightly smaller than the sample was glued on top using the same silver epoxy. The stud with the sample was mounted onto a long aluminum rod, and inserted into the STM cryostat. The sample was then cleaved in cryogenic vacuum at $T < 20K$. STM measurements were performed at two temperatures. Since the focus was the normal (i.e. not superconducting) nematic state of FeSe, spectroscopic images for energies between -8.75 meV and +8.75 meV were measured at 10K while the remaining images were measured at 4K to reduce thermal smearing. This is justified since the maximum superconducting gap in FeSe is about 2.5 meV [1].

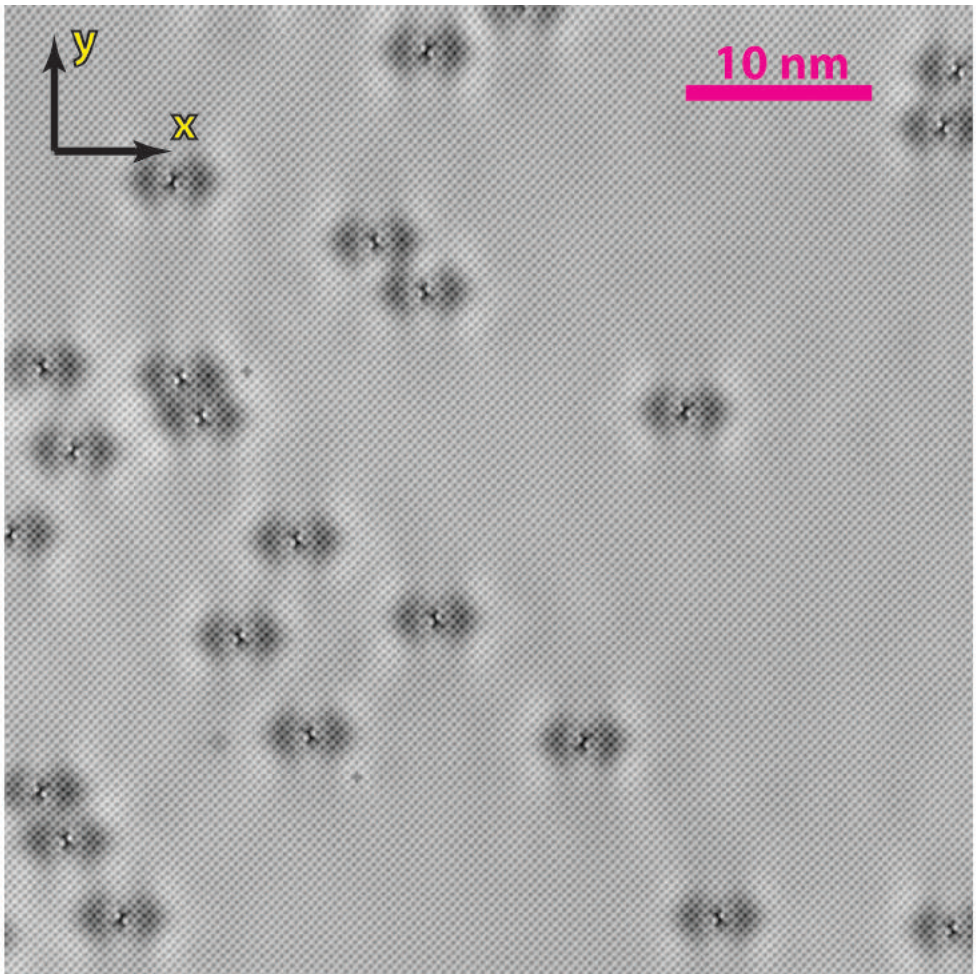

Figure 4.5: High resolution STM topography of the experimental field of view for single domain QPI studies. The topographic image was acquired at -20 mV bias and 10 pA setup current. The FOV size is 52 nm, and the resolution is 1024 pixels. The axes *x* and *y* are the longer and shorter orthorhombic, respectively.

The maximum piezo scanner range of the STM instrument used is 200 nm. Although topographic 200 nm by 200 nm images of FeSe crystal typically were found to contain a few nematic domain walls, relatively large regions (over 100 nm by 100 nm) within a single domain were not uncommon. Fig. 4.5 shows one high resolution topographic image of FeSe of a 52 nm by 52 nm field of view (FOV) within a single domain. FeSe cleaves between loosely bonded Se planes, and the atomic contrast corresponds to Se atoms of the exposed surface. The most common surface defect observed is centered on an iron site (i.e. in between

two nearest neighbor selenium atoms). These defects cause the two nearest Se atoms to appear brighter in topographs. Because there are two inequivalent Fe sites relative to Se positions, there are two types of these "dimers" related to each other via a 90° rotation. Regardless of the orientation of the dimers, there are clear perturbations in the energy-integrated local density of states along the x-axis which corresponds to the longer orthorhombic axis. These perturbations due to quasiparticle interference are the primary focus of this chapter.

Fig. 4.6 contains representative data images for energies below the chemical potential from SI-STM spectroscopic studies performed in the FOV of Fig. 4.5. As mentioned before, the data for $E \leq -10$ meV was acquired at 4.2 K, while the data close to the chemical potential (i.e. $-10 < E \leq 0$ meV) was acquired at 10 K. The energy resolution for the current study is $\Delta E = 1.25$ meV (i.e. the energy difference between consecutive data images). Both $g(\vec{r}, E) \equiv dI/dV(\vec{r}, E = eV)$ and $I(\vec{r}, E = eV)$ were sampled and recorded using a 300 by 300 point grid. The spatial resolution is then $\Delta x = \frac{52\,\text{nm}}{300} = 0.173\,\text{nm}$. In the Fourier space, this corresponds to the wavevector resolution equal to $\Delta q = \frac{2\pi}{52\,\text{nm}} = 0.121\,\text{nm}^{-1}$ and to the longest wavevector component within the Nyquist window equal to $\frac{\pi}{\Delta x} = 18.1\,\text{nm}^{-1}$. Since the crystallographic Bragg peaks are at $(\pm\frac{\pi}{a_{Fe}}, \pm\frac{\pi}{b_{Fe}}) = (\pm 11.8, \pm 11.8)\,\text{nm}^{-1}$, we are capturing the full Brillouin zone. The normalized conductance images $L(\vec{r}, E = eV)$ are obtained by dividing $dI/dV(\vec{r}, E = eV)$ images by their $I(\vec{r}, E = eV)$ counterparts.

The perturbations due to quasiparticle interference surrounding defects on iron sites are clearly visible in all types of spectroscopic images shown. Below the chemical potential, they are strongly unidirectional and aligned along the longer orthorhombic axis. Later in the chapter it will be argued that this direc-

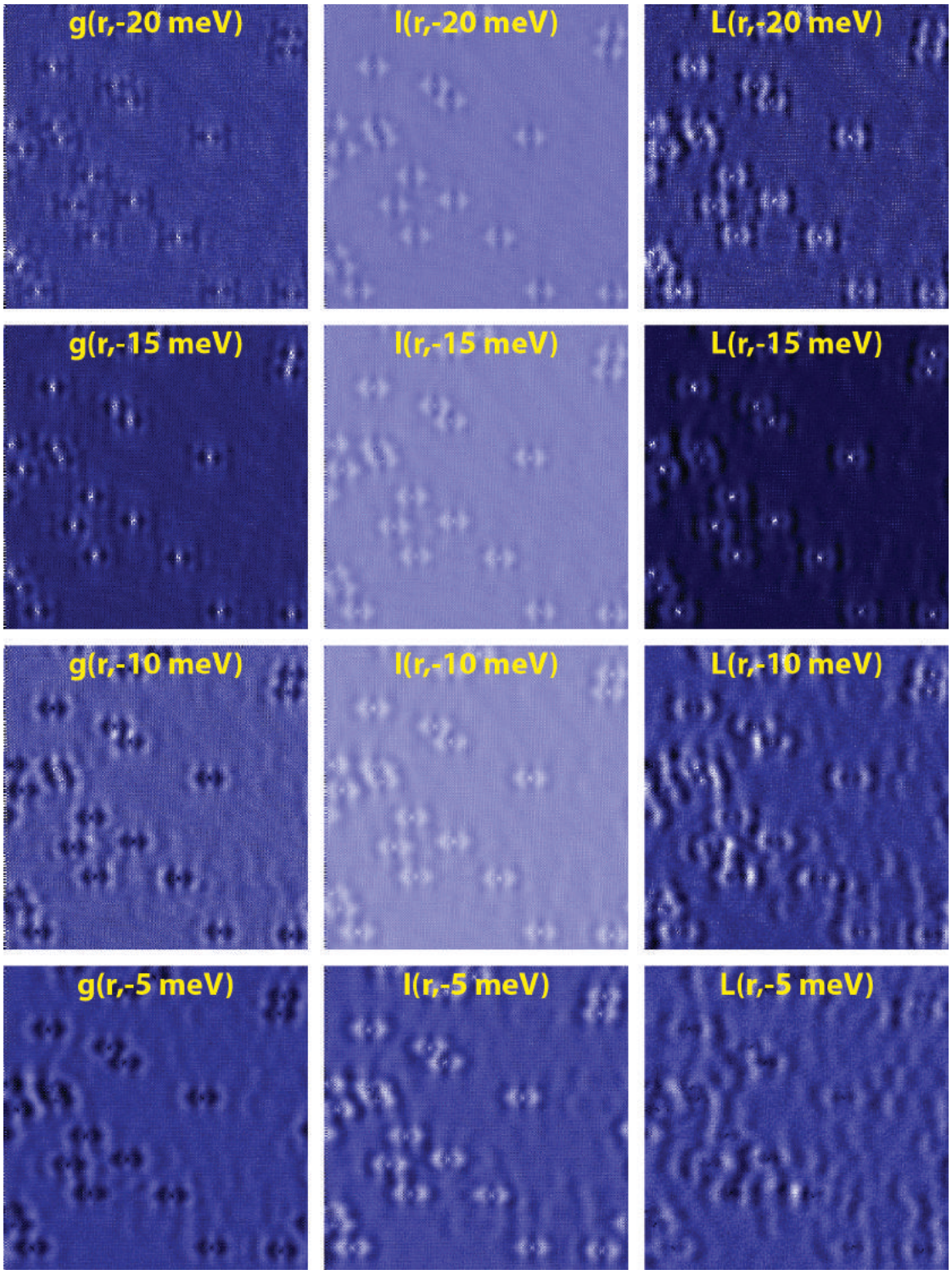

Figure 4.6: Spectroscopic data images in real space below the chemical potential. Left, Conductance images $g(\vec{r}, E)$ **Center,** Current images $I(\vec{r}, E)$ **Right,** Normalized conductance images $L(\vec{r}, E)$

tionality is most consistent with scattering of quasiparticles exhibiting orbital-selective correlations.

Likewise, Fig. 4.7 contains representative data images for energies above the chemical potential from SI-STM spectroscopic studies performed in the FOV of Fig. 4.5. The data for $E \geq +10$ meV was acquired at 4.2 K, while the data close to chemical potential (i.e. $0 \leq E < 10$ meV) was acquired 10 K. Here the quasiparticle interference patterns for $E \geq +10$ meV have strong component aligned along the shorter orthorhombic axis.

Fig. 4.8 shows normalized conductance images acquired in the field of view containing a twin boundary. The QPI patterns in different domains are rotated by 90° degrees relative to each other as expected.

4.3 Measured quasiparticle interference in FeSe

After reviewing the relevant experimental methodology, I am ready to discuss the SI-STM study of the nematic state of FeSe. Particularly, the observed unidirectionality of quasiparticle interference patterns will be analyzed in the context of the orbital-selective ansatz introduced above. Measured spectroscopic maps in Fourier space will be compared to the T-matrix calculations performed with and without orbital-selective quasiparticle weights. It will be shown that quasiparticle scattering is strongest between the $\vec{k}$ states with substantial d_{yz} orbital component and weak otherwise. This confirms the existence of strong orbital-selective correlations in the nematic state of FeSe implied earlier by the studies of the superconducting state [1,51].

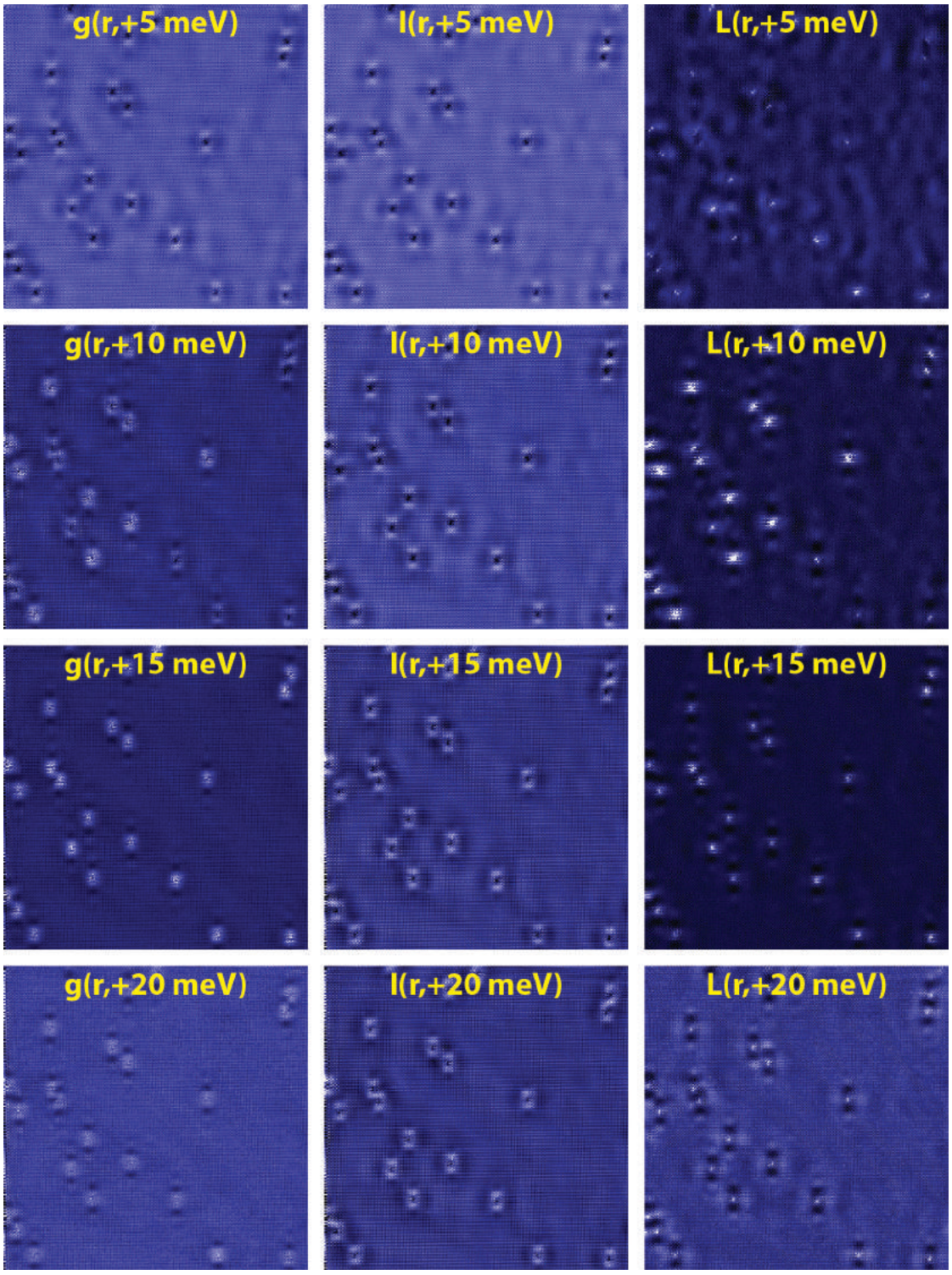

Figure 4.7: Spectroscopic data images in real space above chemical potential. Left, Conductance images $g(\vec{r}, E)$ **Center,** Current images $I(\vec{r}, E)$ **Right,** Normalized conductance images $L(\vec{r}, E)$

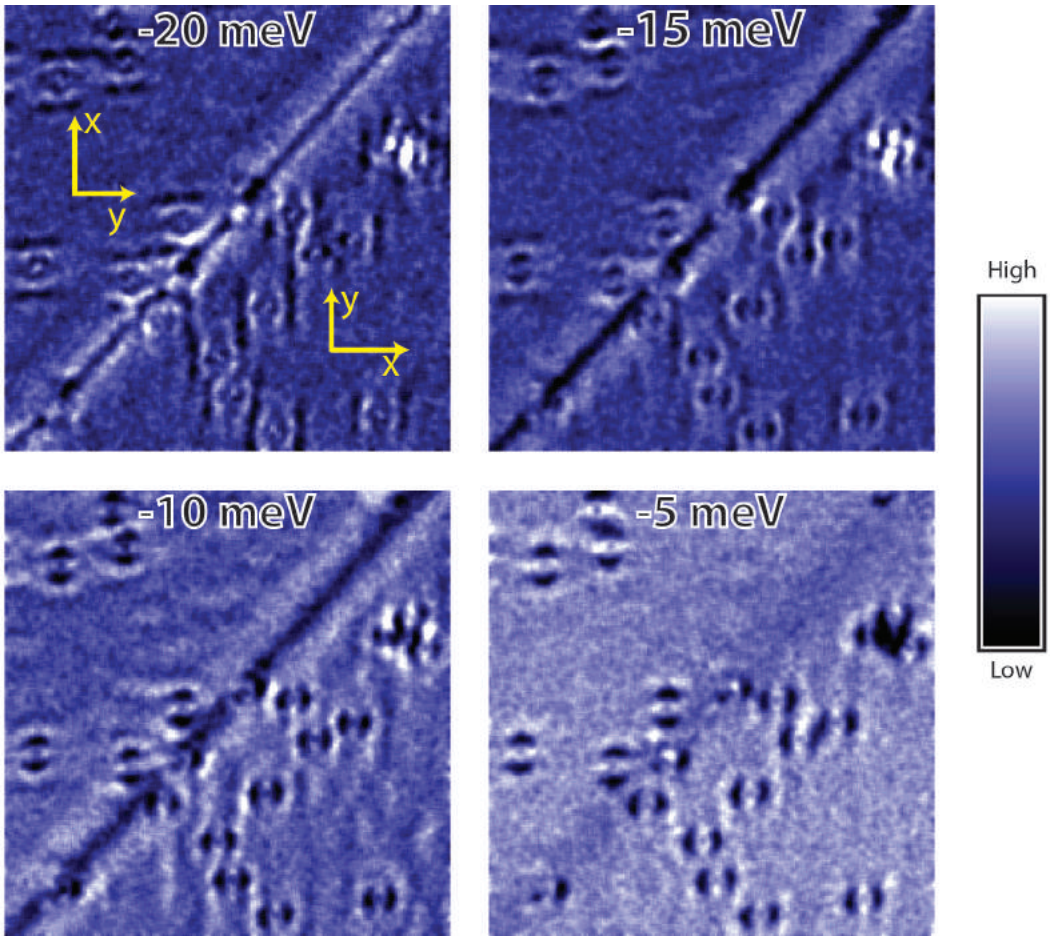

Figure 4.8: Rotation of quasiparticle interference patterns across the twin boundary. Normalized conductance images $L(\vec{r}, E)$ in the FOV containing twin boundary. The longer orthorhombic axis is x, and the shorter orthorhombic axis is y.

4.3.1 Representative measured and calculated Fourier transforms of normalized conductance

I begin by looking at measured quasiparticle interference phenomena at small wavevectors $\vec{q}$ and compare them to the anticipated scattering patterns calculated within the T-matrix approach. By focusing on small wavevectors, I restrict myself to intraband scattering. In the uncorrelated picture where all the quasiparticles are of equal spectral weight, we expect three sets of $\vec{q}$ vectors that

correspond to interference within α, ε, and δ bands. Hence, if we find that only a certain subset of expected $\vec{q}$ wavevectors dominate the QPI pattern, we should conclude that the correlations are important for faithfully modeling the physics of the nematic state of FeSe.

In this section, the amplitude of the spatial Fourier transform of the normalized conductance is used as QPI signature. Recall that the normalized conductance is defined as $L(\vec{r}, E = eV) = \frac{dI(\vec{r},V)/dV}{I(\vec{r},V)/V}$ (section 2.2.3). Experimentally, both $I(\vec{r}, V)$ and $\frac{dI(\vec{r},V)}{dV}$ are acquired simultaneously allowing this normalization. Theoretically, $L(\vec{r}, E)$ is proportional to $n(E, \vec{r})/\int_0^E n(E', \vec{r})dE'$ where $n(E, \vec{r})$ is the local density of states at energy E and location r. For a system with impurities, this quantity can be numerically computed within the T-matrix approximation (sections 3.2.2 and 3.2.3). In the discussion below, single impurity calculations are used.

Fig. 4.9A-B shows the amplitudes of Fourier transforms of the normalized conductance, $\left|L(\vec{q}, E)\right|$, at two representative energies below the chemical potential in the nematic state of FeSe calculated within the T-matrix approximation in the absence of any orbital-selective correlations (i.e. $Z_s = 1$). Here I focus on intraband scattering by considering small wavevectors. Fig. 4.9C-D also shows calculated $\left|\tilde{L}(\vec{q}, E)\right|$, but with tilde denoting that orbital-selective ansatz is used. That is "dressed" Green's functions, $\tilde{G}^R_{ss'}(\vec{k}, E) = \sqrt{Z_s Z_{s'}} G^R_{ss'}(\vec{k}, E)$, are used in the T-matrix calculations. In this scenario with orbital-selective correlations, the quasiparticle weights are set to $Z_s = (0.073, 0.94, 0.16, 0.85, 0.36)$ as before. As mentioned previously, the most relevant values correspond to the three dominant orbitals (i.e. $(Z_{xy}, Z_{xz}, Z_{yz}) = (0.073, 0.16, 0.85)$). Finally, Fig. 4.9E-F shows the amplitude of spatial Fourier transform of measured normalized conductance,

$\left|L^{EXP}(\vec{q}, E = eV)\right|$. The intensity pattern of the measured QPI agrees better with the calculation describing orbital-selective quasiparticles (OSQP). The scattering signal is strong primarily along the q_x where wavevectors connect states belonging to hole-like band α with high d_{yz} orbital content which suggests that d_{yz} is the least correlated orbital.

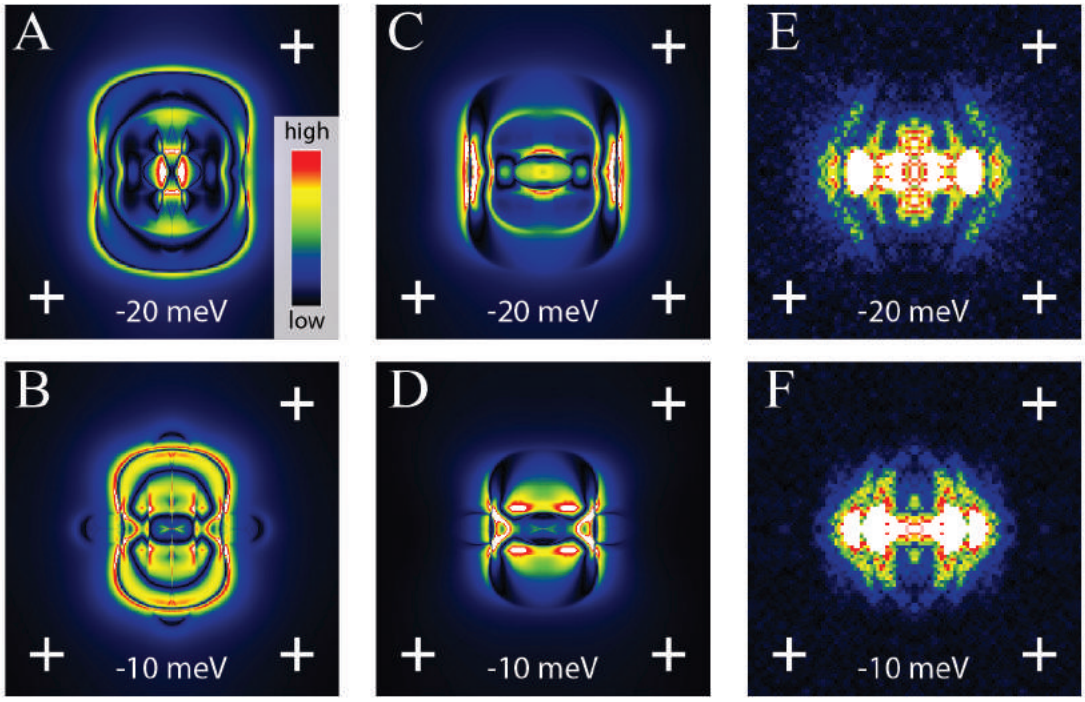

Figure 4.9: Measured and calculated QPI patterns below the chemical potential. **A-B,** Calculated $\left|L(\vec{q}, E)\right|$ QPI signature of intraband scattering when all quasiparticles are assumed to be fully coherent (i.e. $Z_{xy} = Z_{xz} = Z_{yz} = 1$ and hence $Z_\mu(\vec{k}) = 1$). The white crosses correspond to $\frac{3}{16}(\pm\frac{2\pi}{a_{Fe}}, \pm\frac{2\pi}{b_{Fe}})$ points in the momentum transfer ($\vec{q}$-) space. **C-D,** Calculated $\left|\tilde{L}(\vec{q}, E)\right|$ QPI signature of intraband scattering when quasiparticles weights are assumed to be different (specifically $Z_{xy} \approx 0.1, Z_{xz} \approx 0.2, Z_{yz} \approx 0.8$). **E-F,** Measured $\left|L^{EXP}(\vec{q}, E = eV)\right|$ of FeSe at 4K.

Likewise, Fig. 4.10A-B shows the amplitudes of Fourier transforms of the calculated normalized conductance, $\left|L(\vec{q}, E)\right|$, at two representative energies above the chemical potential assuming fully coherent quasiparticles. Fig. 4.10C-D then shows $\left|\tilde{L}(\vec{q}, E)\right|$ for the case of orbital-selective correlations. Finally, Fig.

4.10E-F shows the result of the corresponding measurement at the same energies, $\left|L^{EXP}(\vec{q}, E = eV)\right|$. Again the intensity pattern of the measurement closer matches the OSQP calculation.

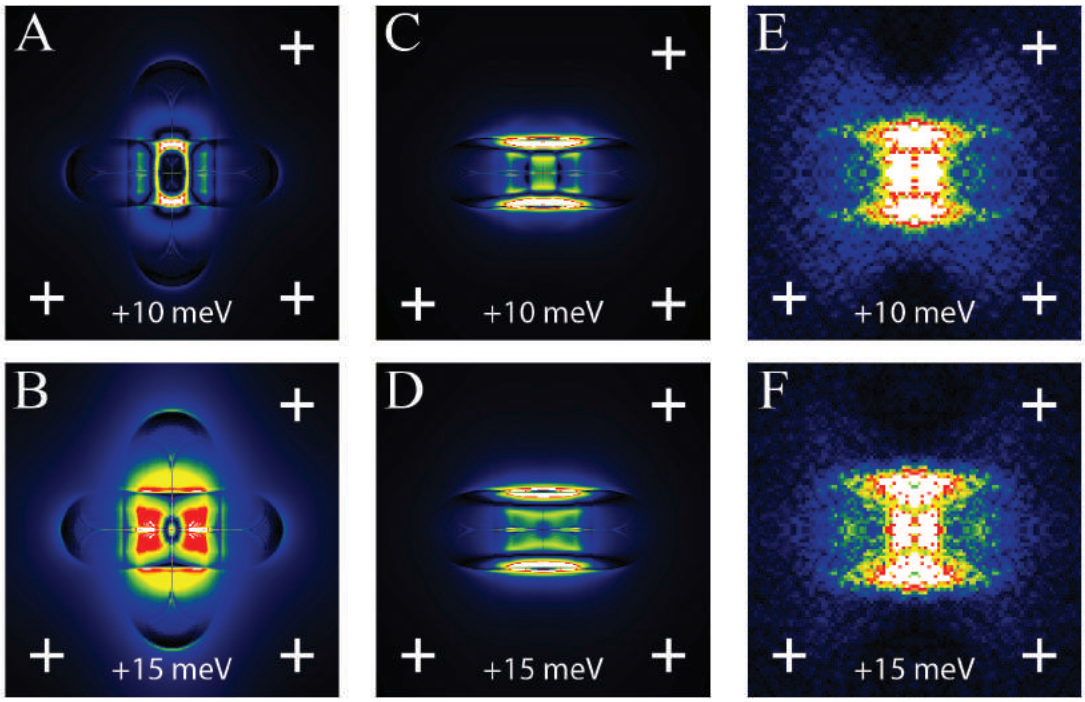

Figure 4.10: Measured and calculated QPI patterns above the chemical potential. A-B, Calculated $L(\vec{q}, E)$ QPI signature of intraband scattering when all quasiparticles are assumed to be fully coherent. **C-D,** Calculated $L(\vec{q}, E)$ QPI signature of intraband scattering when quasiparticles weights vary. **E-F,** Measured $L(\vec{q}, E)$ of FeSe at 4K.

From the measurement of quasiparticle interference, it is clear the interference patterns in the nematic phase of FeSe are very unidirectional. The directionality rotates by 90 degrees close to the chemical potential. This is reproduced by the T-matrix calculations if it is assumed that quasiparticle weights are different for the different orbitals and specifically that the quasiparticles of predominantly d_{yz} character are most itinerant. It is not surprising since from the tight binding parameterization, it is evident that horizontal wavevectors con-

nect such states below the chemical potential and vertical wavevectors connect them above the chemical potential. The rest of this chapter will provide further analysis of $\left|L^{EXP}(\vec{q}, E = eV)\right|$ to bolster the case for the orbital-selective correlations.

4.3.2 Constructing Line cuts

In the subsequent sections, I will analyze line cuts through spatial data maps like $\left|L^{EXP}(\vec{q}, E = eV)\right|$. Therefore, it would be worthwhile to formally define these line cuts and describe the algorithm for computing them.

Recall that spectroscopic data maps are spatially sampled functions of the local density of states (section 2.2.3). A data map consists of a sequence of pixelated images with each image corresponding to a single energy. I will use normalized conductance $L^{EXP}(\vec{r}, E)$ as an example of a data map. Due to the finite spatial sampling, $L^{EXP}(\vec{r}, E)$ is only defined on a 2D grid of points (x_n, y_m) where n and m are integers. The spatial resolution of the measurement is given by $\Delta x \equiv x_{n+1} - x_n$ and $\Delta y \equiv y_{n+1} - y_n$ which are typically equal. $L^{EXP}(x_n, y_m, E)$ is the value of the image (corresponding to energy E) at pixel (n, m).

A line cut is the set of data map values along a line connecting two points, (x_1, y_1) and (x_2, y_2), on the grid of sampled locations . This line cut through $L^{EXP}(x_n, y_m, E)$ will be denoted as $L_{(x_1,y_1)\rightarrow(x_2,y_2)}(r_k, E)$ where $\{r_k\} = \{r_0, r_1, ..., r_n\}$ is a set of equally spaced coordinates along the cut such that $r_0 = 0$ and $r_n = \sqrt{(x_2 - x_1)^2 + (y_2 - y_1)^2}$. The number of segments in the line cut is chosen by $\max(\frac{|x_2 - x_1|}{\Delta x}, \frac{|y_2 - y_1|}{\Delta y})$. Fig. 4.11A shows an example of a line cut through an image. The line cut is shown as a red line, and the first (i.e. (x_1, y_1) and r_0) and last

(i.e. (x_1, y_1) and r_n) pixels are marked by the black dots through the pixel center. The red dots represent the set of spatial points corresponding to the interior coordinates $\{r_k\}$. They typically do not lie on the center of a pixel and hence, have values assigned using an interpolation method. Bilinear interpolation is used for computing all line cuts presented in this thesis. This technique is depicted in Fig. 4.11B and described in the corresponding caption.

Additionally, we can increase the signal to noise ratio and smooth the line cut at the expense of spatial resolution by performing a transverse averaging procedure in computing $L_{(x_1,y_1)\to(x_2,y_2)}(r_k, E)$. To visualize this procedure, I consider the averaging symmetric line segment (see the blue segment in Fig. 4.11A) through (x_k, y_k) that is perpendicular to the line cut. Then to determine the value of the line cut at r_k (i.e. (x_k, y_k)), we simply average the set of values assigned to the locations along the averaging segment spaced one pixel apart. Again the assignment of values to arbitrary coordinates is done by using bilinear interpolation.

Finally, one last bit of notation needs to be introduced. Often a line cut is calculated from the Fourier transformed data set, where the origin of the cut is a natural (often $\vec{q} = 0$), and its direction can specified by providing an angle. In this case, the line cut will be denoted as $L(q_\theta, E)$.

4.3.3 Line cuts of QPI patterns along major symmetry axis

Having introduced the notion of a line cut through a spectroscopic map in the previous section, here I will analyze the line cuts along principle symmetry directions derived from the calculated and measured L-maps introduced in

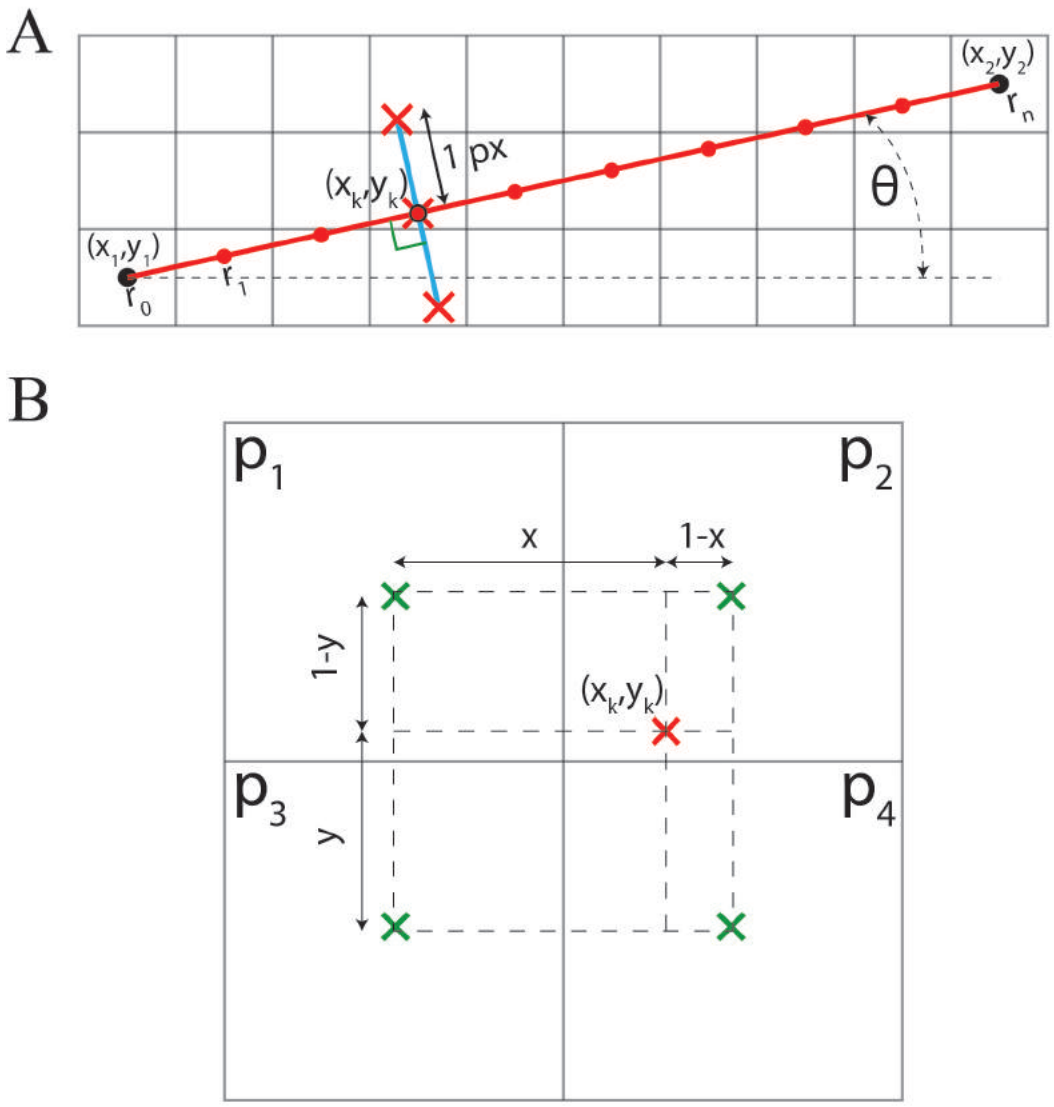

Figure 4.11: Algorithm for constructing line cuts from STM data images. A, A representative line cut through a pixel grid. The blue perpendicular line segment shows the path used for transverse averaging. **B,** Sketch explaining bilinear interpolation. The red cross marks the location, (x_k, y_k), where the value needs to be assigned. The blue crosses mark the four nearby pixels relevant for interpolation. If the image values at these four pixels are (p_1, p_2, p_3, p_4), then the interpolated value is $f(x_k, y_k) = p_1 \cdot (1-x)(y) + p_2 \cdot (x)(y) + p_3 \cdot (1-x)(1-y) + p_4 \cdot (x)(1-y)$.

section 4.3.1. To reveal the structure of quasiparticle interference patterns, these maps were defined in the Fourier ($\vec{q}$)-space. Since for QPI any scattering vector $\vec{q}$ connects two $\vec{k}$ states, the $\vec{q}$-space will also be referred to as momentum trans-

fer space. Since all Fermi pockets are twofold symmetric in the nematic state of FeSe, the major symmetry directions in $\vec{q}$-space are q_x and q_y axes.

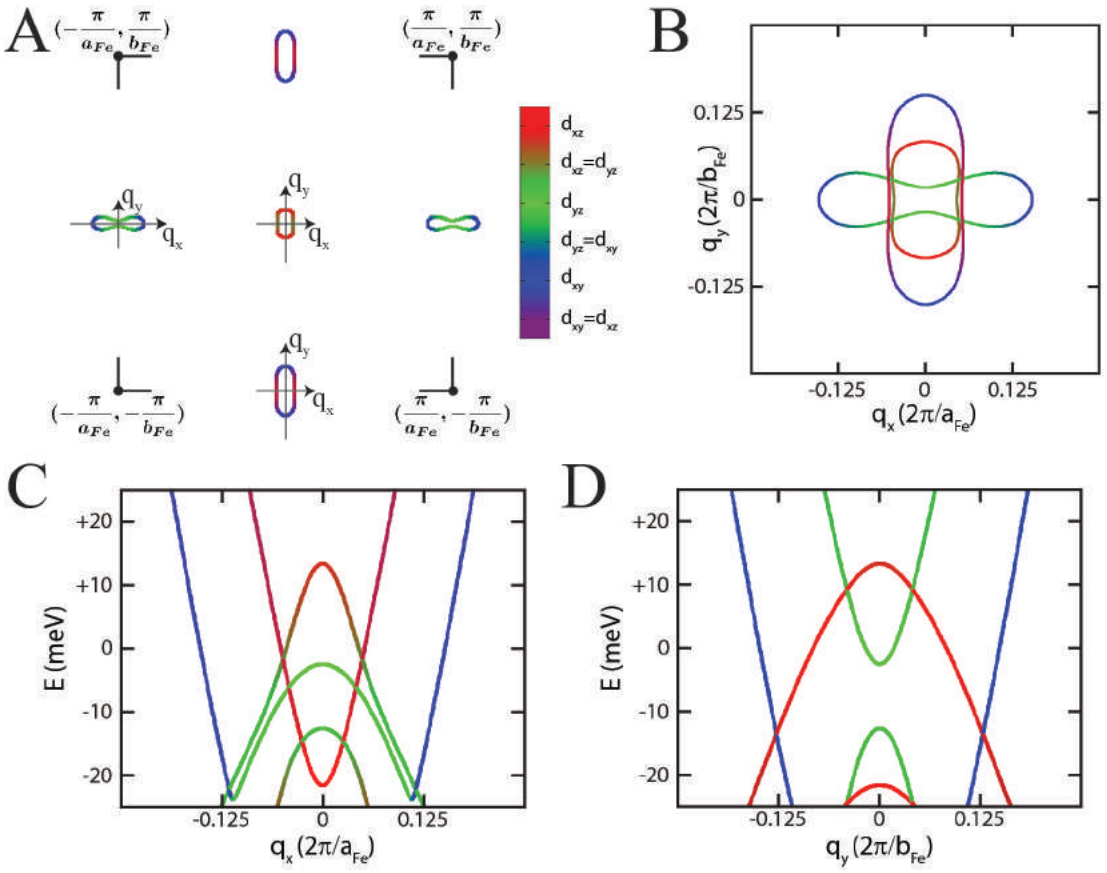

Figure 4.12: FeSe band structure in momentum transfer space along major symmetry axes. A, Fermi surface of FeSe at low temperature labelling major symmetry directions for intraband QPI analysis as q_x and q_y. **B,** Fermi surface $k_z = 0$ contours shown in $\vec{q}$-space. **C,** The band structure at $k_z = 0$ near chemical potential plotted along q_x. **D,** The band structure at $k_z = 0$ near chemical potential plotted along q_y. The figure is adapted from [101].

To facilitate interpretation of the line cuts across QPI patterns, it is worthwhile to consider the plot of FeSe band structure model in the momentum transfer space along q_x and q_y. Fig. 4.12A shows the orbitally resolved plot of the Fermi surface at $k_z = 0$. The horizontal and vertical fold axes for all three bands are labelled as q_x and q_y. This is appropriate since intraband scattering across

the pocket center between the $\vec{k}$ states intersecting these axes will correspond to wavevectors on q_x and q_y axes in $\vec{q}$-space. Fig. 4.12B also shows the Fermi surface at $k_z = 0$, but now plotted in the momentum transfer space. Such a plot is constructed by translating all the pockets so that they are centered at $\vec{q} = 0$, because each $\vec{q}$ wavevector is the difference between two $\vec{k}$ vectors and hence does not preserve the information about the absolute location of a band in $\vec{k}$-space. The linear dimensions of $\vec{q}$-plots of Fermi pockets are doubled relative to $\vec{k}$ plots since the contours now represent the dominant scattering between the diagonally opposite $\vec{k}$-states. For example, for the α-band at the center of the Brillouin zone, the dominant scattering is between $\vec{k}$ and $-\vec{k}$, and the wavevectors are given by $\vec{q} = 2\vec{k}$. Fig. 4.12C-D show the orbitally resolved cuts of band structure at $k_z = 0$ along the q_x and q_y. Within the orbital-selective ansatz, we expect the line cuts $\left|\tilde{L}(q_x, E)\right|$ and $\left|\tilde{L}(q_x, E)\right|$ to resemble the green d_{yz} component of these plots. Alternatively, if there is no substantial difference in the values of the quasiparticle weights among d_{xz}, d_{yz} and d_{xy} orbitals, all the dispersions in Fig. 4.12C-D should be observed in $|L(q_x, E)|$ regardless of orbital character.

Now I examine the $\vec{q}$-space line cuts across L-maps for the two major symmetry directions. Fig. 4.13A-B show $|L_n(q_x, E)| \equiv |L_n(q_{0^\circ}, E)|$ and $\left|L_n(q_y, E)\right| \equiv |L_n(q_{90^\circ}, E)|$ derived from T-matrix calculation of QPI signature $|L(\vec{q}, E)|$ assuming all orbitals are equally coherent. The letter n indicates that the line cuts were normalized such that the maximum intensity is 1 at each energy, i.e. $L_n(q_\theta, E) = \frac{L(q_\theta, E)}{\max_{q_\theta} L(q_\theta, E)}$. This normalization makes band dispersions more visible. Fig. 4.13C-D then show $\left|\tilde{L}_n(q_x, E)\right|$ and $\left|\tilde{L}_n(q_y, E)\right|$ for the orbital-selective quasiparticles (refer to section 4.1.2 for Z_s values). Evidently, the "red"/d_{xz} and "blue"/d_{yz} dispersions shown in Fig. 4.13C-D are present in the coherent calculation but suppressed in the orbital-selective calculation. Note that L-maps are

undefined for $E = 0$ meV, and hence the corresponding layer is set to 0 in Fig 4.13.

Finally Fig. 4.13E-F shows the measured line cuts, $\left|L_n^{EXP}(q_x, E)\right|$ and $\left|L_n^{EXP}(q_y, E)\right|$. Refering to Fig. 4.12C-D, the dominant dispersions in Fig 4.13E-F originate from d_{yz} states belonging to α and ε bands. The measurements match closer to the calculations with the orbital-selective quasiparticles shown in Fig. 4.13C-D.

As discussed at the end of section 4.1.4, the observed suppression of certain QPI dispersions is very unlikely to be caused by the orthogonality of eigenvectors in orbital space. Fig. 4.12C-D makes it quite clear that the eigenvectors belonging to states lying on the major symmetry axes are dominated by a single orbital. One such state cannot be orthogonal to the state diagonally opposite to $\vec{k}$-space relative to the center of the relevant band. Therefore, the data presented in this section strongly points to the conclusion that the quasiparticle weight for d_{yz} orbital is substantially bigger than the other two active orbitals in the vicinity of the chemical potential (d_{xz} and d_{xy}).

4.3.4 Analysis of the electron-like dispersions

As discussed previously, the specific values for the orbital quasiparticle weights (i.e. $(Z_{xy}, Z_{xz}, Z_{yz}) = (0.073, 0.16, 0.85)$) were used to simulate QPI in the proposed orbital-selective state in FeSe. The simulated images are not sensitive to the small changes in these parameters. The goal of the quasiparticle interference study is to test the assertion that the quasiparticle weights follow the general trend $Z_{yz} \gg Z_{xz} > Z_{xy}$. This trend would explain the superconducting gap

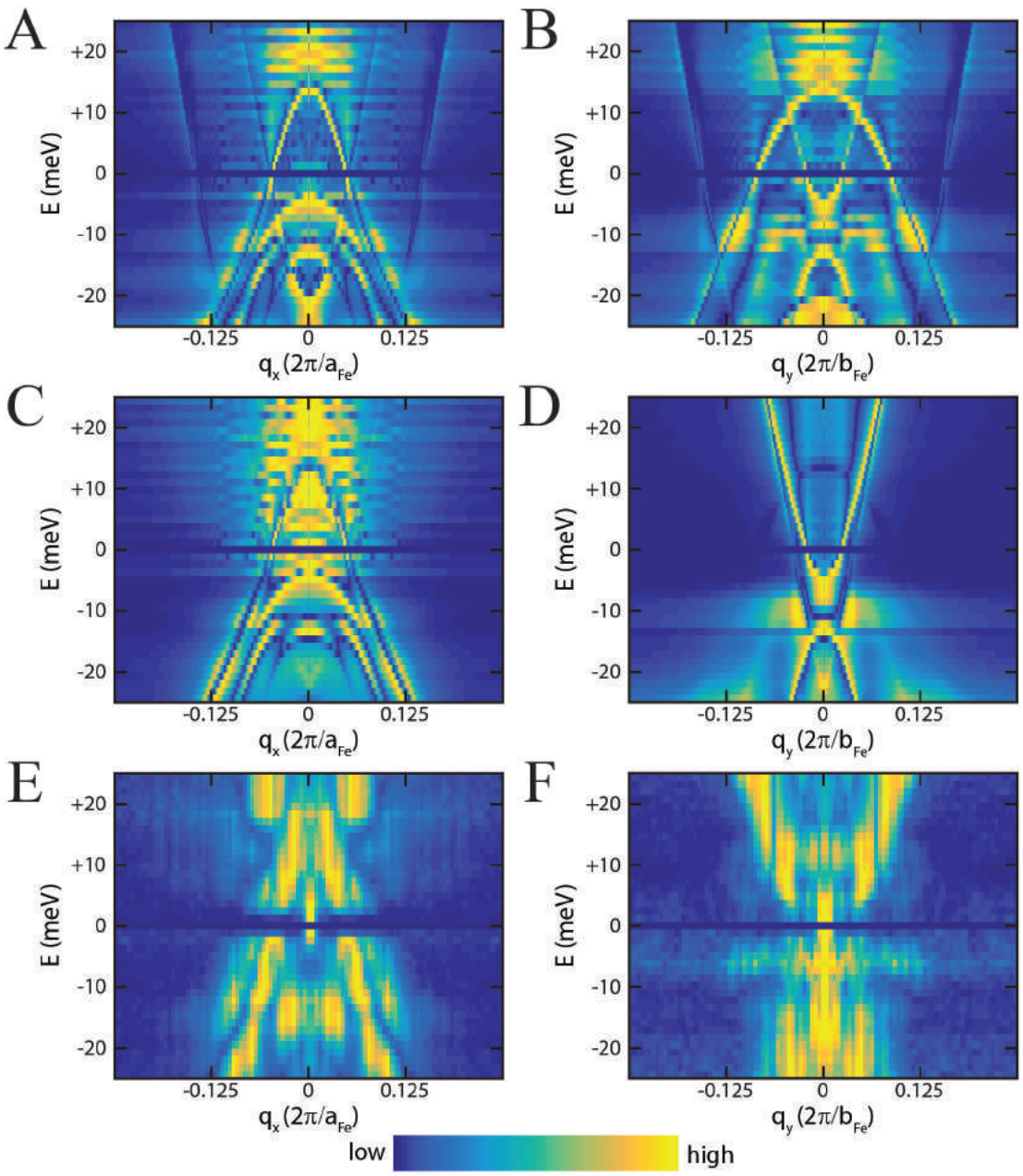

Figure 4.13: Energy resolved orbital-selective QPI along major symmetry axes. A-B, Calculated intensities of intraband scattering signature for fully coherent state shown in the two E-q planes parallel to q_x, $|L_n(q_x, q_y = 0, E)|$ and q_y, $|L_n(q_x = 0, q_y, E)|$. **C-D,** Calculated $|\tilde{L}_n(q_x, q_y = 0, E)|$ and $|\tilde{L}_n(q_x = 0, q_y, E)|$ for proposed orbital-selective state **E-F,** Measured intensities of intraband QPI signature along the two major symmetry axes. The figure is adapted from [101].

anisotropy within the itinerant theory of the spin fluctuation pairing of Ref. [51] and the missing spectral weight for the electron-like δ-band of d_{xy} and d_{xz} orbital

character in the ARPES experiments [69, 70]. Also, small Z_{xy} is expected theoretically since from the studies of the many-body effects it is known that the d_{xy} orbital is strongly renormalized [102, 103] (Section 1.2).

Since the ARPES studies of detwinned FeSe crystals did not observe the δ-band, and the quasiparticle weights Z_s are proposed to obey the relation $Z_{yz} \gg Z_{xz} > Z_{xy}$, it is worthwhile to look for the quasiparticle interference that would be attributed to scattering between states primarily of d_{xz} character. The existence of such a QPI signal would put a limit on the decoherence of the d_{xz} states. This is of interest since this decoherence has presumably a lot to do with the unusual nematic state in FeSe where properties associated with the d_{xz} and d_{yz} orbitals are no longer equivalent in the absence of tetragonal symmetry. In fact, these orbitals are split in energy, and the splitting is $\vec{k}$-dependent [66, 69].

The intraband quasiparticle interference associated with the d_{xz} states can hypothetically be detected both on the α-band below the chemical potential, and on the δ-band above the chemical potential. However, as evident from the analysis of the line cuts along the major symmetry axes (section 4.3.3), experimentally all QPI dispersions assigned to the α-band originate from the $\vec{k}$ state with large d_{yz} component. Within the proposed orbital-selective formalism, this observation implies that $Z_{yz} \gg Z_{xz}$. Therefore, it is more promising to look for d_{xz} QPI dispersion of the δ-band above the chemical potential because this band is dominated by the d_{xz} and d_{xy} orbitals and lacks any substantial d_{yz} component (Fig. 4.12).

Fig. 4.14A shows orbitally resolved constant energy contours at E = +15 meV. The intraband QPI for the ε-band is expected to be strong for vertical wavevectors connecting the d_{yz} states and suppressed for horizontal wavevec-

tors connecting the d_{xy} states if the assertion $Z_{yz} \gg Z_{xz} > Z_{xy}$ is true. Likewise, for the δ-band, weak intraband QPI is expected for horizontal wavevectors connecting the d_{xz} states, and should be suppressed for the vertical wavevectors connecting the d_{xz} states. The dominant scattering vectors for each band are represented by double-headed black arrows, and the suppressed vectors are shown with thin gray arrows. Fig. 4.14B then shows the relevant data image, $\left|L^{EXP}(\vec{q}, E = +15 \text{ meV})\right|$. The image was symmetrized along the twofold axes (i.e. q_x and q_y). There are two visible spectral peaks corresponding to QPI signals. The strong peak intersecting the q_y axis is a result of QPI between the d_{yz} states belonging to the ε-band. Much weaker peak intersecting the q_x axis is attributed to QPI between the d_{xz} states states belonging to the δ band. These assignments are not ambiguous because of the correspondence between the actual lengths of the $\vec{q}$ vectors and the expected lengths from the tight binding parameterization that was designed to agree with the APRES [69, 70] and quantum oscillations [66, 71] data. The centers of these peaks are marked by the black circle (ε-band) and the black square (δ-band), and their locations are determined by a Gaussian fit. In the data image, there are no visible peaks that could be assigned to the quasiparticle interference between d_{xy} states. All these observations are consistent with the hypothesis of orbital-selective correlations and specifically with the proposed relation between the orbital weights (i.e. $Z_{yz} \gg Z_{xz} > Z_{xy}$).

Since not all peaks in the Fourier transform of spectroscopic maps should be assigned to the quasiparticle interference phenomena, it is important to consider the peak dispersions as a function of energy. The data structures $L^{EXP}(\vec{q}, E)$ can contain non-dispersing peaks because of density waves, bound impurity states or the setup effect (Sec. 2.2.3). The peaks discussed above do disperse with energy as evident from the experimental line cuts $\left|L^{EXP}(q_y, E)\right|$ and $\left|L^{EXP}(q_x, E)\right|$

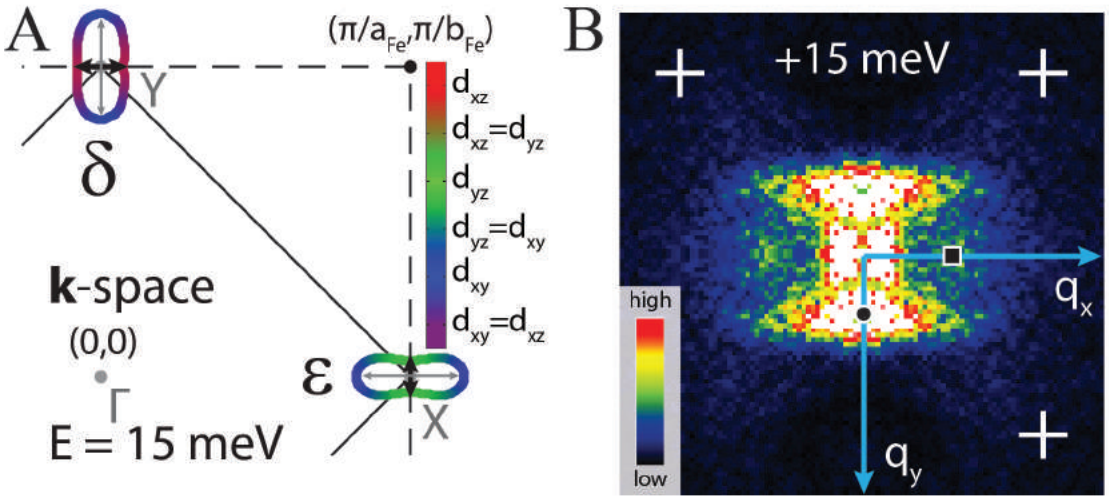

Figure 4.14: Intraband quasiparticle interference for the electron-like bands. **A,** Orbitally resolved constant energy contours at $E = +15$ meV showing the electron-like ε and δ-bands. As always, the d_{xz}, d_{yz} and d_{xy} orbitals are represented by red, green and blue colors respectively. Black double-headed arrows show the detected scattering vectors along q_x and q_y, and gray arrows show the scattering vectors suppressed completely due to the very low d_{xy} quasiparticle weight. **B,** $\left|L(\vec{q}, E = +15 \text{ meV})\right|$ data image. The directions for the line cuts $\left|L^{EXP}(q_x, E)\right|$ and $\left|L^{EXP}(q_y, E)\right|$ are shown as blue lines. Intraband QPI attributed to ε and δ bands are marked by the black circle and the black circle, respectively. The white crossed represent $\frac{3}{16}(\frac{2\pi}{a_{Fe}}, \frac{2\pi}{b_{Fe}})$ points in momentum transfer space. The figure is adapted from [101].

shown in Fig. 4.15A-B, respectively. The dispersion of ε-band is marked in $\left|L^{EXP}(q_y, E)\right|$ plot by the black dots. The location of each dot at the specific energy E', $\tilde{q}_y^{\varepsilon}(E')$ is determined by considering the data plot $\left|L^{EXP}(q_y, E')\right|$ versus q_y and fitting an identifiable QPI peak to the sum of a Gaussian function and a linear background, $f_{fit}(q_y) = A \exp\left(-\frac{(q_y-\tilde{q}_y)^2}{2\sigma^2}\right) + B \cdot q_y + C$. The error bars in the plot represent the width of Gaussians obtained in the corresponding fits. The fits for the q_y direction are shown in Fig. 4.16B. Likewise, the QPI dispersion for the δ-band $\tilde{q}_x^{\delta}(E)$ is marked in $\left|L^{EXP}(q_x, E)\right|$ plot by the black squares whose locations and displayed error bars are determined by the corresponding fits provided in Fig. 4.16A.

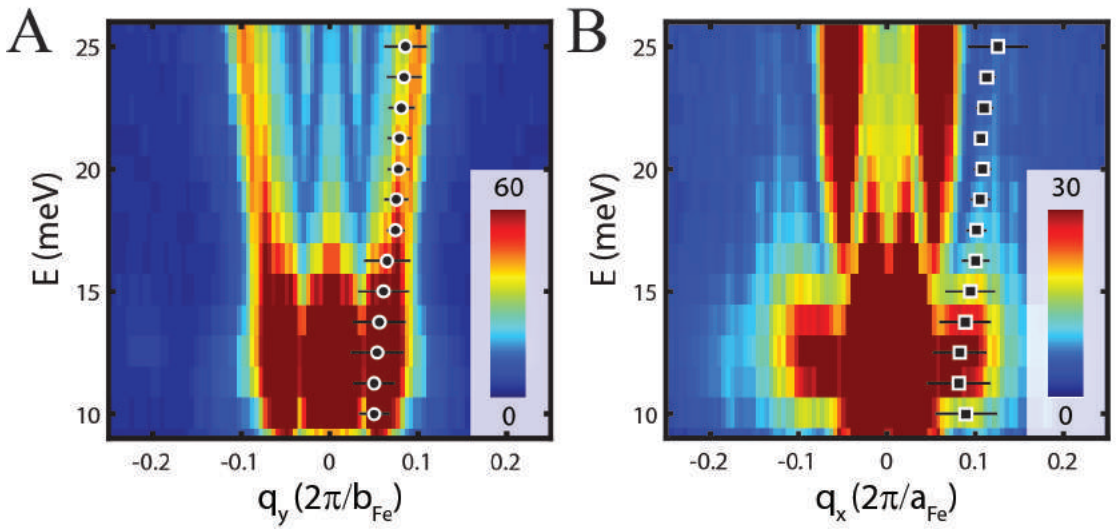

Figure 4.15: Line cuts showing the electron-like dispersions above the chemical potential A, $\left|L^{EXP}(q_y, E)\right|$ line cut. **B,** $\left|L^{EXP}(q_x, E)\right|$ line cut. For each energy in **A** and **B**, the peak due quasiparticle interference was fit to a Gaussian peak, and the extracted peak location and width are shown with the black circles and lines. Note that in order to increase the visibility of $\tilde{q}_x^{\delta}(E)$ dispersion, the maximum intensity in **B** is set to half of the maximum intensity in **A** with respect to the color scale. The figure is adapted from [101].

The peak amplitude parameter extracted from the Fig. 4.16 fits can be used to determine the relative QPI amplitudes for the ε- and δ- bands. Fig. 4.17 shows the QPI peak amplitudes for these bands as a function of energy above the chemical potential. The QPI amplitudes along q_y and attributed to the d_{yz} states of the ε-band are represented by the green circles, and the QPI amplitudes along q_x and attributed to the d_{xz} states of the δ-band are represented by the red squares. There is a clear peak around $E = +12.5$ meV for both signals, which most likely corresponds to a scattering resonance. Recall that the scattering matrix is given by $\hat{T}(E) = V_{imp}\hat{I}\left(\hat{I} - V_{imp}\sum_{\vec{k}}\hat{G}^R(\vec{k}, E)\right)^{-1}$. If $\hat{I} - V_{imp}\sum_{\vec{k}}\hat{G}^R(\vec{k}, E)$ becomes small at some energy, there is an enhanced QPI response given by the usual formula $\delta n(\vec{q}, E) = -1/\pi\,\mathrm{Tr}\,\mathrm{Im}\sum_{\vec{k}}\hat{G}(\vec{k}, E)\hat{T}(E)\hat{G}(\vec{k}+\vec{q}, E)$. It is clear that the quasiparticle interference between the d_{yz} states is much stronger than between the d_{xz} states. Since the Fermi velocities and nesting conditions are similar for

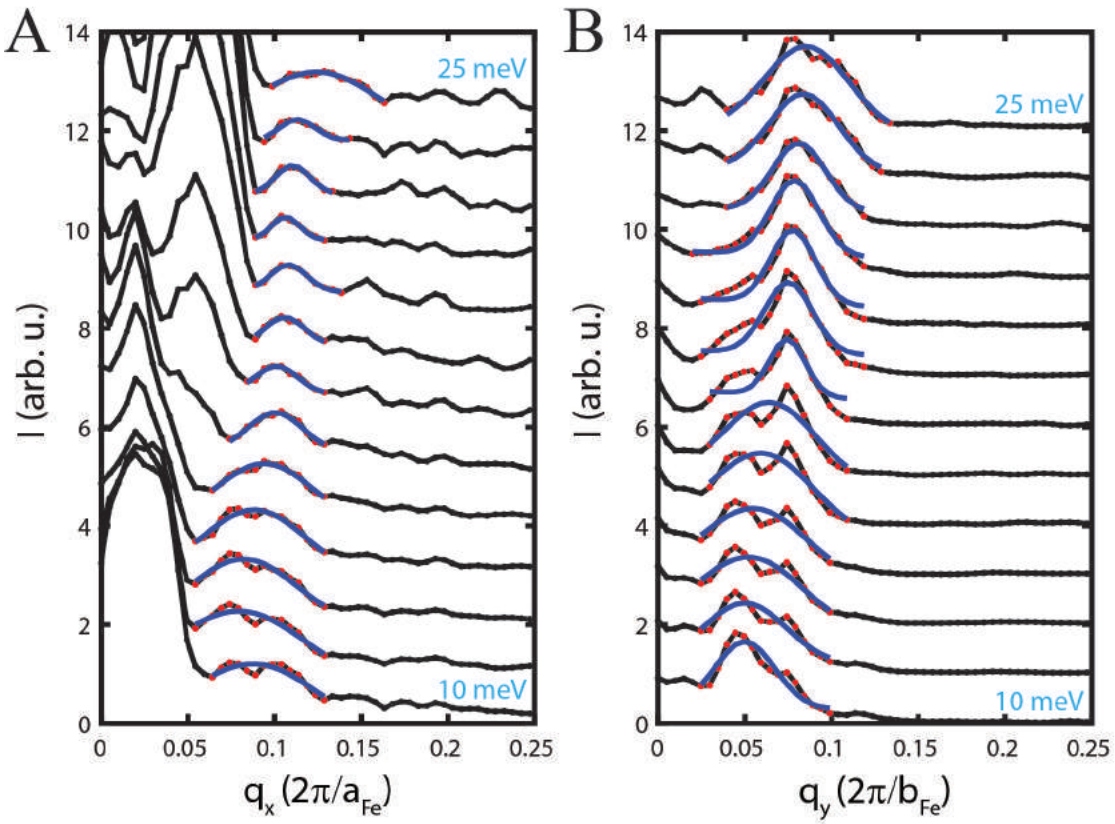

Figure 4.16: Extracting band dispersions A, Line cut fits for the QPI peaks along q_x assigned to the δ-band **B,** Line cut fits for the QPI peaks along q_y assigned to the ε-band. The figure is adapted from [101].

both bands at specified energies and wavevectors, the observed QPI anisotropy further suggests that the d_{xz} orbital is more correlated than the d_{yz} orbital.

To summarize the results of the analysis of the quasiparticle interference patterns above the chemical potential, we conclude that observations of the difference in the scattering response intensity between the d_{xz} and d_{yz} orbitals and the lack of such a response for the d_{xy} orbital is consistent with the hypothesis that the orbital quasiparticle weights follow $Z_{yz} \gg Z_{xz} > Z_{xy}$.

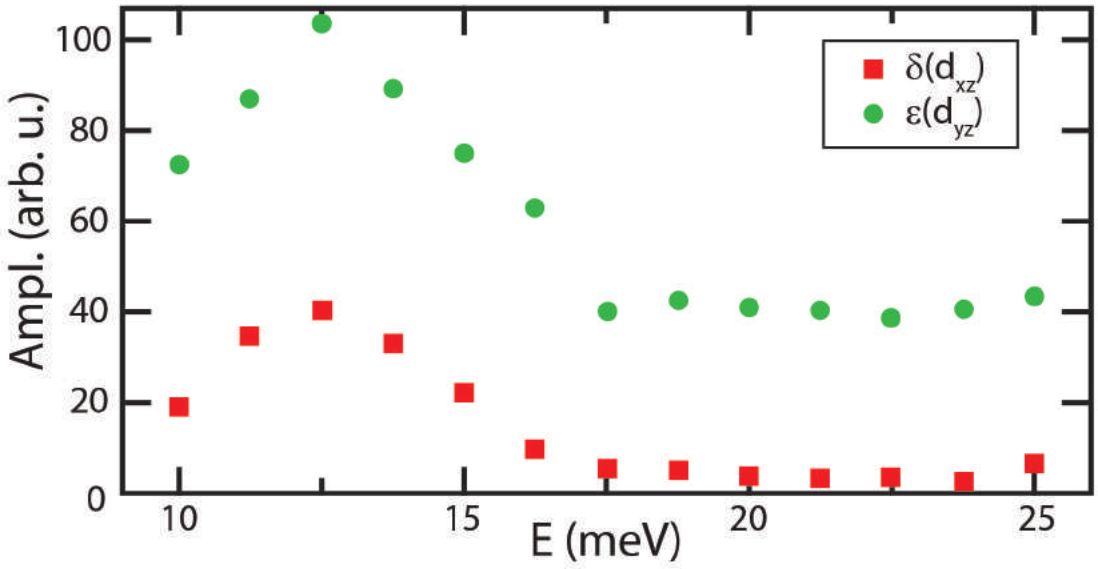

Figure 4.17: Extracted amplitudes for QPI signals for the electron-like bands The figure is adapted from [101].

4.3.5 QPI anisotropy as a function of angle

Finally, I examine the strength of the quasiparticle interference as a function of the $\vec{q}$-space angle and relate it to the evolution of the quasiparticle weight $Z_\mu(\vec{k})$ with the $\vec{k}$-space angle around the constant energy contours of the α- and ε- bands.

As discussed in section 4.3.1, the quasiparticle interference patterns in the nematic phase of FeSe are quite unidirectional. Below $E = +10$ meV, QPI waves are oriented along the longer orthorhombic axis (which is defined to be the x axis). Just above this energy, however, the directionality rotates, and QPI waves are oriented along the shorter orthorhombic axis (i.e. y axis). The degree of this unidirectionally can be quantified by comparing the line cuts of L-maps for all possible directions in $\vec{q}$-space.

Fig. 4.18A shows the symmetrized data image $\left|L^{EXP}(\vec{q}, E = -20 \text{ meV})\right|$ mark-

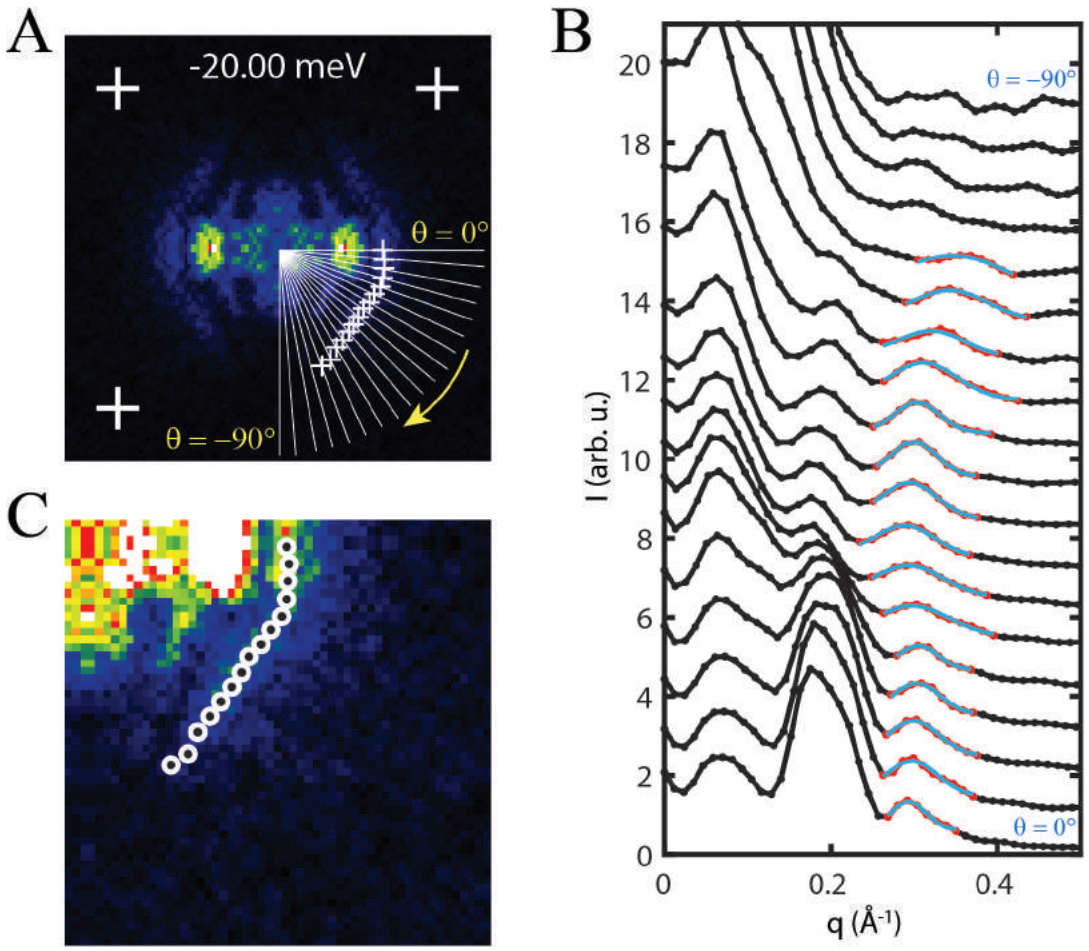

Figure 4.18: Line cuts $\left|L^{EXP}(q_\theta, E = -20\text{ meV})\right|$ for a sequence of angles. A, $\left|L^{EXP}(\vec{q}, E = -20\text{ meV})\right|$ data image symmetrized along the q_x and q_y axis. The white lines indicate the directions of the angular line cuts. The white crosses mark $\frac{3}{16}(\pm\frac{2\pi}{a_{Fe}}, \pm\frac{2\pi}{b_{Fe}})$ points in $\vec{q}$-space. **B,** Line cuts $\left|L^{EXP}(q_\theta, E = -20\text{ meV})\right|$ for a range of angles offset vertically for visibility and normalized (i.e. scaled) by the mean intensity of quasiparticle peak. In the construction of these line cuts, the transverse averaging of 5 pixels (2 pixels on either side) was used (see section 4.2.6). The peaks attributed to intraband scattering within the α-band were fit to $f_{fit}(q_\theta) = A(\theta)\exp\left(-\frac{(q_\theta - q^*_\theta)^2}{2\sigma^2}\right) + B \cdot q_\theta + C$. The fit curves are shown as blue and the fit data range is shown as red. **C,** One of the symmetric "quarters" of $\left|L^{EXP}(\vec{q}, E = -20\text{ meV})\right|$ marking the locations of QPI peaks $q^*_\theta(E = -20\text{ meV})$ extracted from the fits in **B**.

ing the trajectories of the analyzed line cuts $\left|L^{EXP}(q_\theta, E = -20\text{ meV})\right|$ with the white lines. Fig. 4.18B then shows these line cuts for the set of directions de-

fined by the angle $\theta \in \{-90, -85, -80, ..., -5, 0\}^\circ$ with $\theta = 0^\circ$ and $\theta = -90^\circ$ corresponding to the q_x and q_y line cuts, respectively. For presentation purposes, the line cut plots are offset vertically and scaled. For angles $0^\circ \rightarrow -70^\circ$, the line cuts contain discernible peaks that can be attributed to the α-band QPI contour visible in the image of Fig. 4.18A. The relevant regions of the curves are marked as red. Each relevant peak was fit (blue curves) to a Gaussian function with a linear background (i.e. $f_{fit}(q_\theta(E)) = A(\theta, E) \exp\left(-\frac{[q_\theta(E) - q^*_\theta(E)]^2}{2\sigma^2}\right) + B \cdot q_\theta(E) + C$) to determine the set of QPI wavevectors $q^*_\theta(E = -20\,\text{meV})$, marked in Fig. 4.18C, and scattering amplitudes $A(\theta, E = -20\,\text{meV})$. Fig. 4.19A shows unscaled line cuts (red points) in the vicinity of QPI peaks together with corresponding fits (blue curves), and Fig. 4.19B displays the plot of $A(\theta)$ versus θ. The scattering amplitudes are large close to the q_x axis and non-monotonically decrease as the cut direction approaches the q_y axis.

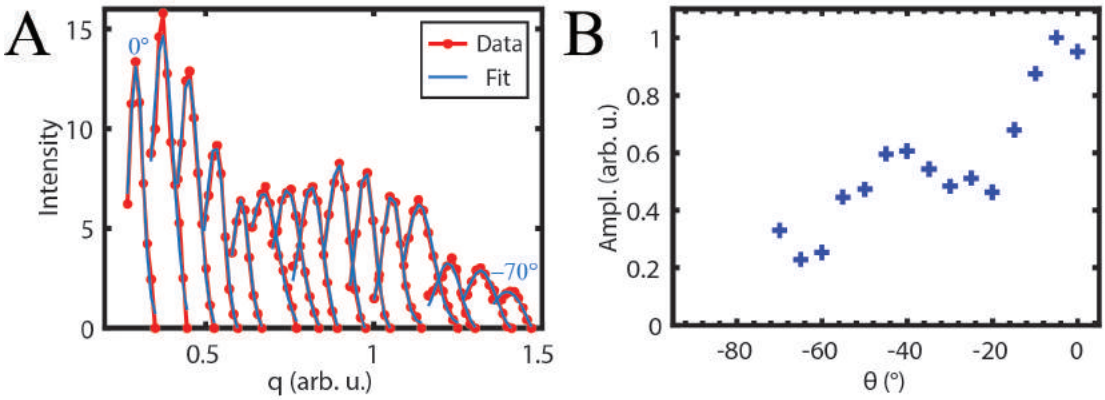

Figure 4.19: Variation of extracted QPI amplitude versus angle at single energy. **A,** Angular dependence of peaks in $\left|L^{EXP}(q_\theta, E = -20\,\text{meV})\right|$ due to intraband scattering of the α-band. The red points with the red line represent the experimental line cuts in the vicinity of QPI peak, and the blue curve is a fit to a Gaussian curve with the linear background. The minimum value of each peak's intensity was subtracted from corresponding data and fit, so that all curves start at zero. Additionally for visibility, the data and fits were shifted horizontally in q. **B,** For a representative energy above the chemical potential, plot of extracted QPI amplitude for the α-band normalized to one, $A_n(\theta, E = -20\,\text{meV}) \equiv \frac{A(\theta, E=-20\,\text{meV})}{\max_\theta A(\theta, E=-20\,\text{meV})}$

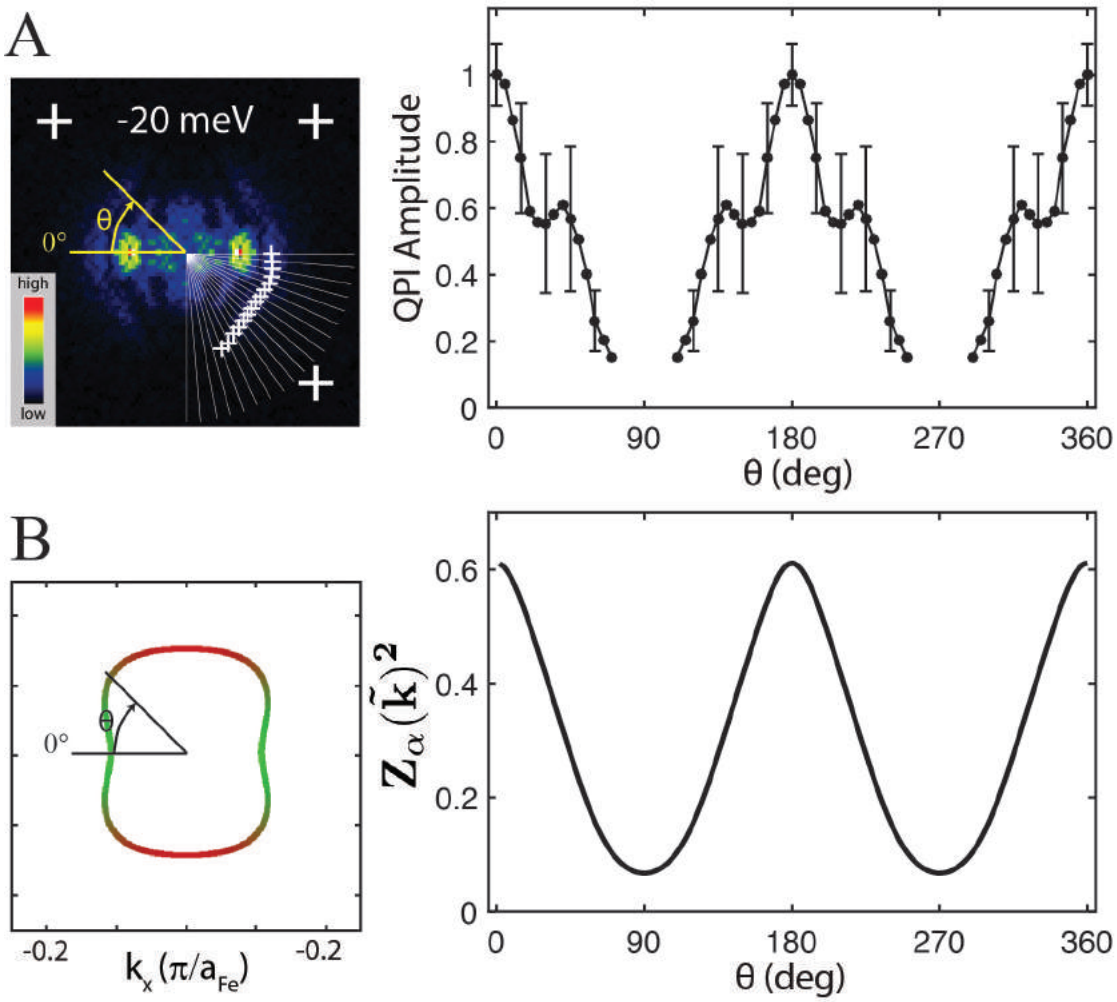

Figure 4.20: Angularly resolved effects of quasiparticle weight Z for α band. **A, Left,** Measured $|L(\vec{q}, E = -20 \text{ meV})|$ image showing the directions of analyzed line cuts, $|L(q_\theta, E)|$. **Right,** Black points show measured QPI intensity as a function of angle for the α band, $A_n(\theta, \bar{E})$. The intensity was averaged over -25 meV to -15 meV energy range and normalized to have maximum value of 1. That is $A_n(\theta, \bar{E}) = \frac{\sum_{E\in[-25,-15] \text{ meV}} A(\theta,E)}{\max_\theta \sum_{E\in[-25,-15] \text{ meV}} A(\theta,E)}$. The vertical bars on the $A_n(\theta, \bar{E})$ data points represent the standard variation of the set $\{ A_n(\theta, E) = \frac{A(\theta,E)}{\max_\theta A(\theta,E)} \mid E \in [-25, -15] \text{ meV} \}$. **B, Left,** Orbitally resolved constant energy contour for α-band at $E = -20$ meV. As usual green and red colors represent d_{yz} and d_{xz}, respectively. **Right,** Square of the quasiparticle weight for the α-band $Z_\alpha(\vec{k})^2$ at $E = -20$ meV as a function $\vec{k}$-space angle.

The analysis above can be repeated for a range of energies defined by $E \in \{-25, -23.75, -22.50, ..., -16.25, -15\}$ meV. Since the results for all these en-

ergies are qualitatively similar with respect to the angular anisotropy of QPI, it makes sense to combine them. For this reason the extracted intraband QPI amplitudes for the α-band are averaged over the mentioned energy range, and the resulting normalized curve $A_n(\theta, \bar{E})$ is plotted as a function of the $\vec{q}$-angle in Fig. 4.20A. The typical energy variations are represented by the error bars on $A_n(\theta, \bar{E})$ points which represent the standard deviation of $A_n(\theta, \bar{E})$ over the set of energies. Fig. 4.20B then shows the orbitally resolved constant energy contour for $E = -20$ meV (i.e. energy in the center of the discussed range) and the square of the associated quasiparticle weights $Z_\alpha(\vec{k}) = \sum_s Z_s |a^s_\alpha(\vec{k})|^2$ as a function of $\vec{k}$-space angle. The quasiparticle weights in orbital space are the same as before, $Z_s = (0.073, 0.94, 0.16, 0.85, 0.36)$. The square of $Z(\vec{k})$ is chosen since in the $\vec{k}$-space integral for the evaluation of QPI patterns, $-\frac{1}{\pi} \operatorname{Im} \operatorname{Tr} \int \hat{G}(\vec{k} + \vec{q}) \hat{T} \hat{G}(\vec{k}) d\vec{k}$, quasiparticle weight appears twice (i.e. once for each Green's function). The strong suppression of intraband scattering for the α band near 90° can be associated with the small quasiparticle weight for the relevant states of predominately d_{xz} character.

Likewise, Fig. 4.21A shows the symmetrized data image $\left|L^{EXP}(\vec{q}, E = +20 \text{ meV})\right|$ marking the trajectories of the analyzed line cuts with the white lines. Fig. 4.21B then shows these line cuts for the set of directions defined above. For angles $-25° \rightarrow -90°$, the line cuts contain discernible peaks that can be attributed to the ε-band QPI contour visible in the image of Fig. 4.21A. The relevant regions of the curves are marked red. Again each relevant peak was fit (blue curves) to a Gaussian peak with a linear background to determine the set of QPI wavevectors $q^*_\theta(E = +20 \text{ meV})$, marked in Fig 4.21C, and the scattering amplitudes $A(\theta, E = +20 \text{ meV})$. Fig. 4.22A shows unscaled line cuts (red points) in the vicinity of QPI peaks together with the corresponding fits (blue curves), and

Fig. 4.22B displays the plot of $A(\theta)$ versus θ. Here the amplitudes are large close to the q_y axis and monotonically decrease as the cut direction approaches the q_x axis.

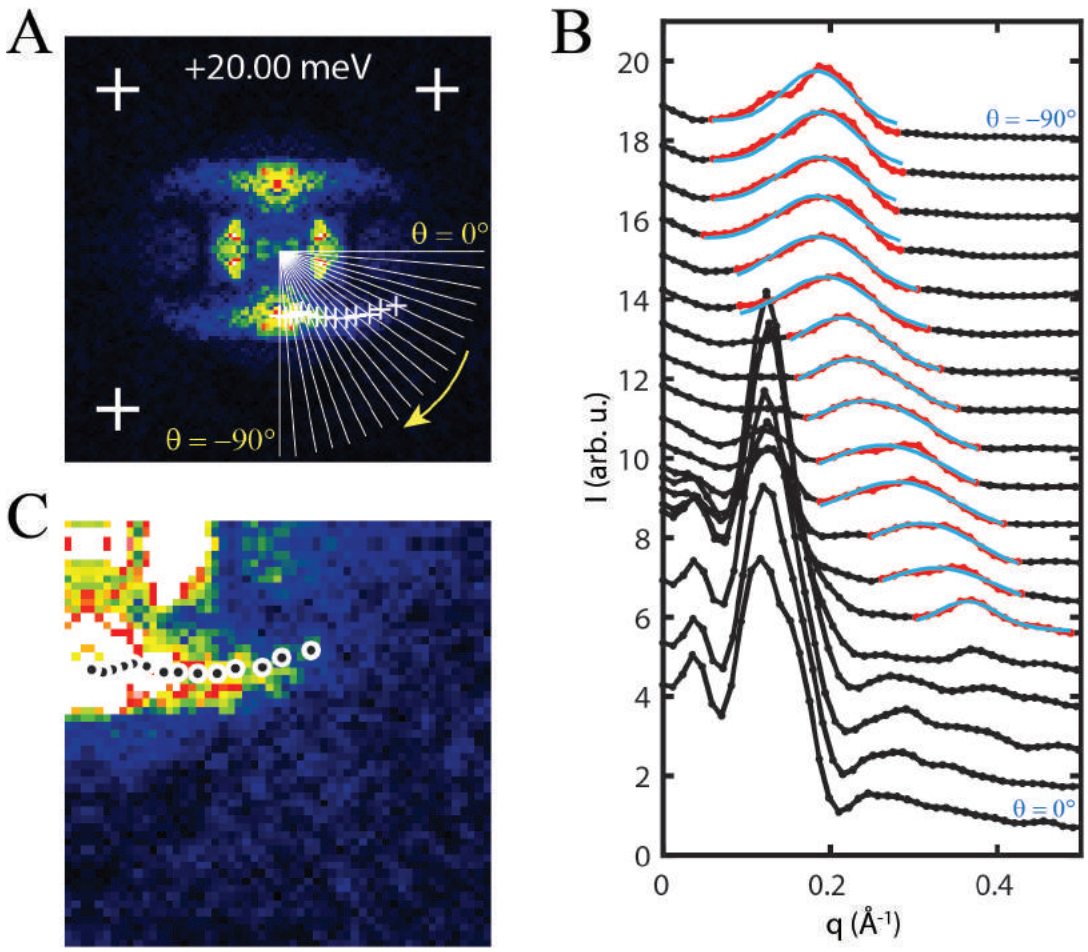

Figure 4.21: Line cuts $L(q_\theta, E = +20\,\text{meV})$ for a sequence of angles. **A,** $\left|L^{EXP}(\vec{q}, E = +20\,\text{meV})\right|$ data image symmetrized along the q_x and q_y axis. The white lines indicate the directions of the angular line cuts. The white crosses mark $\frac{3}{16}(\pm\frac{2\pi}{a_{Fe}}, \pm\frac{2\pi}{b_{Fe}})$ points in $\vec{q}$-space. **B,** Line cuts $\left|L^{EXP}(q_\theta, E = +20\,\text{meV})\right|$ for a range of angles offset vertically for visibility. In the construction of these line cuts, the transverse averaging of 5 pixels was used.The peaks attributed to intraband scattering within ε-band were fit to $f_{fit}(q_\theta) = A(\theta)\exp\left(\frac{(q_\theta - q^*_\theta)^2}{2\sigma^2}\right) + B \cdot q_\theta + C$. The fit curves are shown as blue and the fit data range is shown as red. **C,** One of the symmetric "quarters" of $\left|L^{EXP}(\vec{q}, E = +20\,\text{meV})\right|$ marking the locations of QPI peaks $q^*_\theta(E = +20\,\text{meV})$ extracted from the fits in **B**.

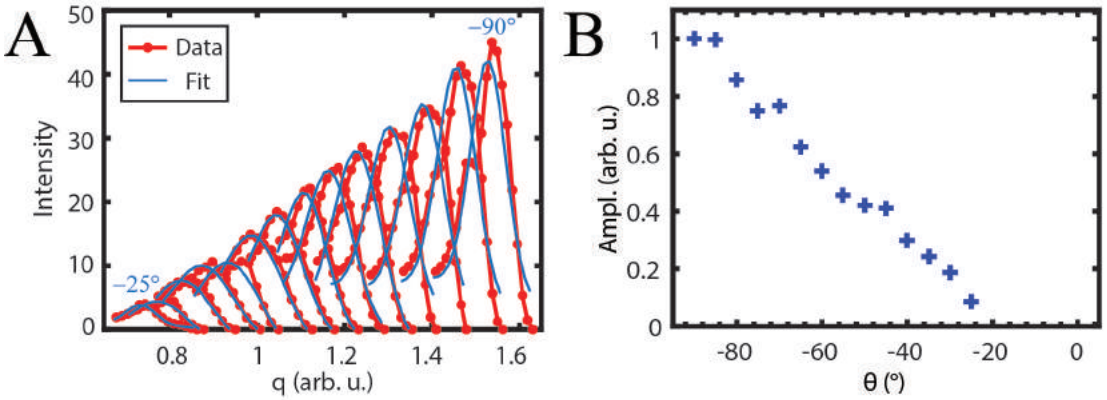

Figure 4.22: Variation of extracted QPI amplitude versus angle at single energy. **A,** Angular dependence of peaks in $\left|L^{EXP}(q_\theta, E = +20\text{ meV})\right|$ due to intraband scattering of the ε-band. The red points with the red line represent the experimental line cuts in the vicinity of QPI peak, and the blue curve is a fit to a Gaussian curve with the linear background. The minimum value of each peak's intensity was subtracted from corresponding data and fit, so that all curves start at zero. Additionally for visibility, the data and fits were shifted horizontally in q. **B,** For a representative energy above the chemical potential, plot of extracted QPI amplitude for the ε-band normalized to one, $A_n(\theta, E = +20\text{ meV}) \equiv \frac{A(\theta, E=+20\text{ meV})}{\max_\theta A(\theta, E=+20\text{ meV})}$

Again I average the extracted QPI amplitudes $A(\theta, E)$ for the ε-band over a range of energies $E \in \{15, 16.25, 17.50, ..., 23.75, 25\}$ meV above the chemical potential. Fig. 4.23A shows the resulting plot $A_n(\theta, \bar{E})$ as a function of the $\vec{q}$-space angle. The typical energy variations are represented by the error bars on $A_n(\theta, \bar{E})$ points which represent the standard deviations of $A_n(\theta, \bar{E})$ over the set of specified energies. Fig. 4.23B then shows the orbitally resolved constant energy contour for $E = +20$ meV (i.e. energy in the center of the discussed range) and the square of the associated quasiparticle weights $Z_\varepsilon(\vec{k}) = \sum_s Z_s |a^s_\varepsilon(\vec{k})|^2$ as a function of the $\vec{k}$-space angle. The quasiparticle weights in orbital space are as listed above. The strong suppression of intraband scattering for the ε band near 0° is associated with small quasiparticle weight for the relevant states of predominately d_{xy} character.

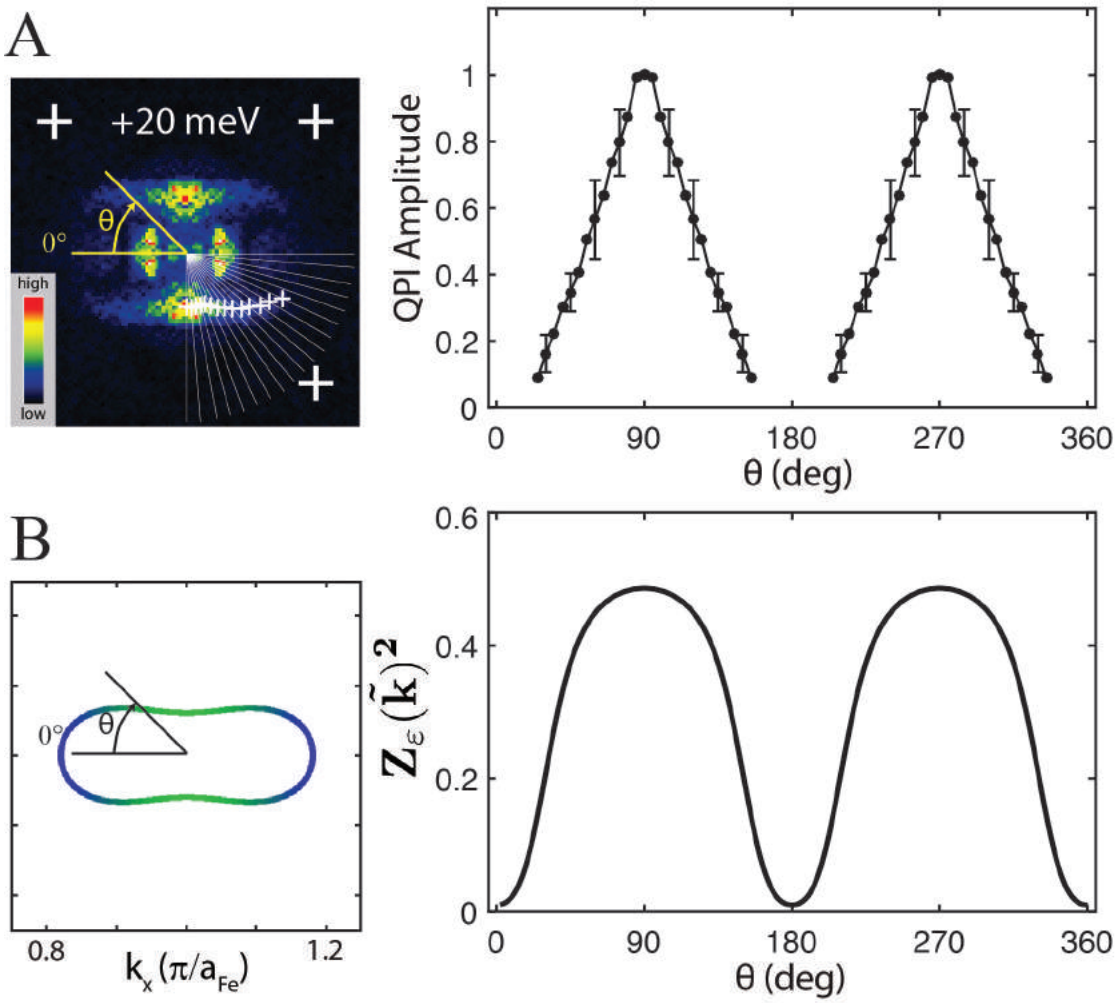

Figure 4.23: Angularly resolved effects of quasiparticle weight Z for ε band. **A, Left,** Measured $|L(\vec{q}, E = +20 \text{ meV})|$ image showing the directions of analyzed line cuts, $|L(q_\theta, E)|$. **Right,** Extracted QPI intensity as a function of angle for the ε band, $A_n(\theta, \bar{E})$. The intensity are averaged over 15 to 25 meV energy range and normalized to 1. **B, Left,** Orbitally resolved constant energy contour for ε-band at $E = +20$ meV. As usual blue and green colors represent d_{xy} and d_{yz}, respectively. **Right,** Square of the quasiparticle weight for the ε-band $Z_\varepsilon(\vec{k})^2$ at $E = +20$ meV as a function $\vec{k}$-space angle.

The data and analysis above demonstrated that in the nematic state of FeSe, the quasiparticle interference patterns on α- and ε-bands close to the chemical potential are strongly anisotropic as a function of $\vec{q}$-space angle. Although some anisotropy can be expected because of nesting within the twofold symmetric

band structure, there is no clear reason why the interference signal should vanish entirely for some scattering directions. Such angular dependence of QPI, however, is expected within the proposed orbital-selective ansatz with the orbital quasiparticle weights obeying $Z_{yz} \gg Z_{xz} > Z_{xy}$. The scattering at the wavevectors connecting $\vec{k}$ states dominated by the d_{xz} and d_{xy} orbitals is suppressed.

4.4 Conclusion and discussion

In this chapter I discussed the effects of interactions on quasiparticle interference patterns. Specifically, I considered interactions in multi-orbital systems, where some orbitals can be more correlated than others. This discussion was then applied to the study of the nematic phase of FeSe.

Low temperature STM measurements of FeSe reveal that the QPI signal is strong only for the states with substantial d_{yz} component. This correlates well with the experimental observation that the superconducting gap magnitude follows the anisotropy of the d_{yz} component of the spectral weight on the Fermi surface [1]. These phenomena are interpreted as evidence of strong orbital anisotropy of the quasiparticle weights. In particular, for the QPI data to be consistent with the T-matrix calculations, the quasiparticle weights should follow $Z_{yz} \gg Z_{xz} > Z_{xy}$.

In FeSCs the small quasiparticle weight for the d_{xy} orbital is expected since this is the most correlated orbital closest to the Mott insulating phase. Additionally, in the nematic phase the quasiparticle weights for the d_{xz} and d_{yz} orbitals can be different. However, the value of the ratio Z_{yz}/Z_{xz} suggested by the QPI [101]

and BQPI [1] experiments is surprisingly large [104, 105] (i.e. $2 < Z_{yz}/Z_{xz} < 4$).

In a recent paper [106] such a high ratio was obtained in a multi-orbital model of the nematic phase of FeSe using $U(1)$ slave-spin theory. Specifically, it was found that the combination of multiple nematic orders was essential for producing this effect. The ARPES and QPI measurements demonstrate that the orbital d_{yz}/d_{xz} splitting is momentum dependent. This is expected if there are multiple nematic orders present. Therefore, the large observed orbital selectivity of quasiparticle weights is likely a consequence of a highly unusual and complex nematic state of FeSe.

CHAPTER 5

INTRA UNIT CELL ROTATIONAL SYMMETRY BREAKING IN NEMATIC FeSe

In the last chapter I discussed long wavelength modulations in local density of states images in the context of orbital-selective quasiparticle scattering. Here I will consider short wavelength atomic LDOS modulations and their structure. In particular, the local density of states STM images with atomic contrast can demonstrate symmetry breaking at the intra unit cell (IUC) level. An example of this phenomena was first reported in a cuprate superconductor $Bi_2Sr_2CaCu_2O_{8+\delta}$ [107, 108] where it was found that the symmetry of the unit cell inside CuO_2 plane in dI/dV images was broken from C_4 down to C_2. In this chapter I will review the techniques introduced in the mentioned studies and apply them to the electronic nematic phase in FeSe [109].

5.1 Extracting the Nematic Order Parameter from STM Images

In the absence of impurities, the local density of states (LDOS) is a function of position that has to be periodic with the lattice. Even though this is trivially true if LDOS is uniform, many STM images have strong atomic contrast. Such images can be described mathematically as a localized function repeated at every lattice site. I will call this function the structure factor. By 'localized', I mean that the structure factor decays to zero over some distance from the origin. The structure factor can be used to probe local symmetries in LDOS images. Specifically in nematic systems, the structure factor distinguishes two otherwise equivalent axes and can be used to define a nematic order parameter. Here I will

use these ideas to introduce an analysis scheme of STM images for visualizing local symmetry breaking.

5.1.1 Structure factor

Let $I(\vec{r})$ represent a typical STM data image of lattice periodicity and introduce the following decomposition mentioned above.

$$\begin{aligned} I(\vec{r}) &= F(\vec{r}) * \sum_{n_1,n_2} \delta(\vec{r} - n_1\vec{a}_1 - n_2\vec{a}_2) \\ &= \int d\vec{r} F(\vec{r} - \vec{r'}) \sum_{n_1,n_2} \delta(\vec{r'} - n_1\vec{a}_1 - n_2\vec{a}_2) \\ &= \sum_{n_1,n_2} F(\vec{r} - n_1\vec{a}_1 - n_2\vec{a}_2) \end{aligned} \tag{5.1}$$

The STM images discussed in this section are assumed to be free of defects. We will identify a function $F(\vec{r})$ as the structure factor of the STM image. This function describes the local structure inside each unit cell, and the entire periodic image is constructed by repeating this structure via convolution (represented by $*$ in the expression above) with the specified lattice of delta functions defined by the primitive lattice vectors $\vec{a}_1$ and $\vec{a}_2$. Since $F(\vec{r})$ should have finite spatial extent, a Gaussian function is an example of an acceptable model for $F(\vec{r})$. This is a reasonable description for the variations of a STM image on the atomic scale.

For illustrative purposes, we can simulate density of states images in a tetragonal lattice with and without intra unit cell rotational symmetry breaking. Fig. 5.1A shows the simulated image using isotropic Gaussian structure factor, and Fig. 5.1B shows the amplitude of its Fourier transform. Fig. 5.1C

then shows the simulated nematic image using an anisotropic Gaussian structure factor, and Fig. 5.1D shows the amplitude of its Fourier transform. Here the unit cells appear to be elongated in a particular direction. By comparing two Fourier transforms, it appears that relative intensities contain the information about the structure factor and its symmetries. This will be shown explicitly in the next section.

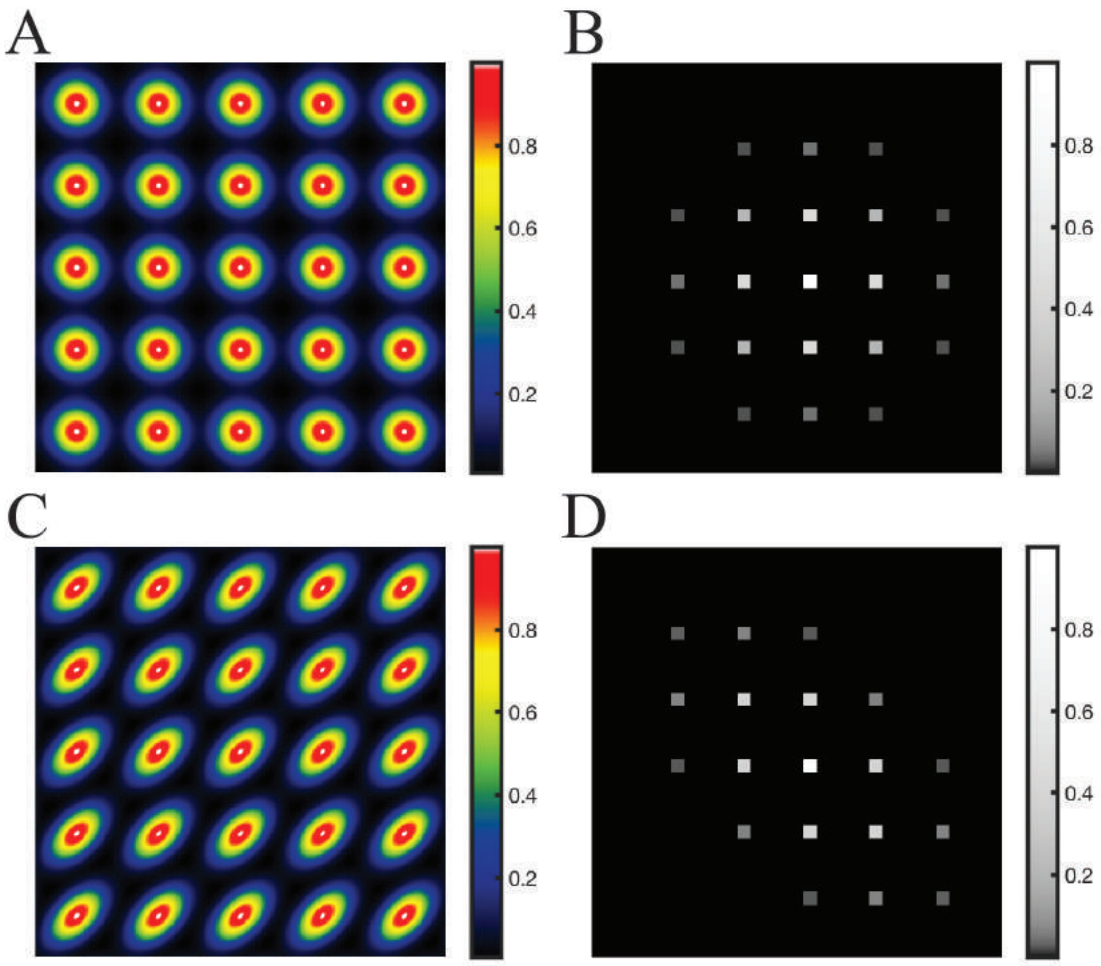

Figure 5.1: Simulated density of states images. A, Tetragonal lattice simulated using isotropic Gaussian structure factor. **B,** Fourier transform of **A**. **C,** Tetragonal lattice simulated using anisotropic Gaussian structure factor. The symmetry breaking is along the direction 45 degrees to the primitive lattice vectors. **D,** Fourier transform of **C**.

To demonstrate that these phenomena are present in real measurements, Fig.

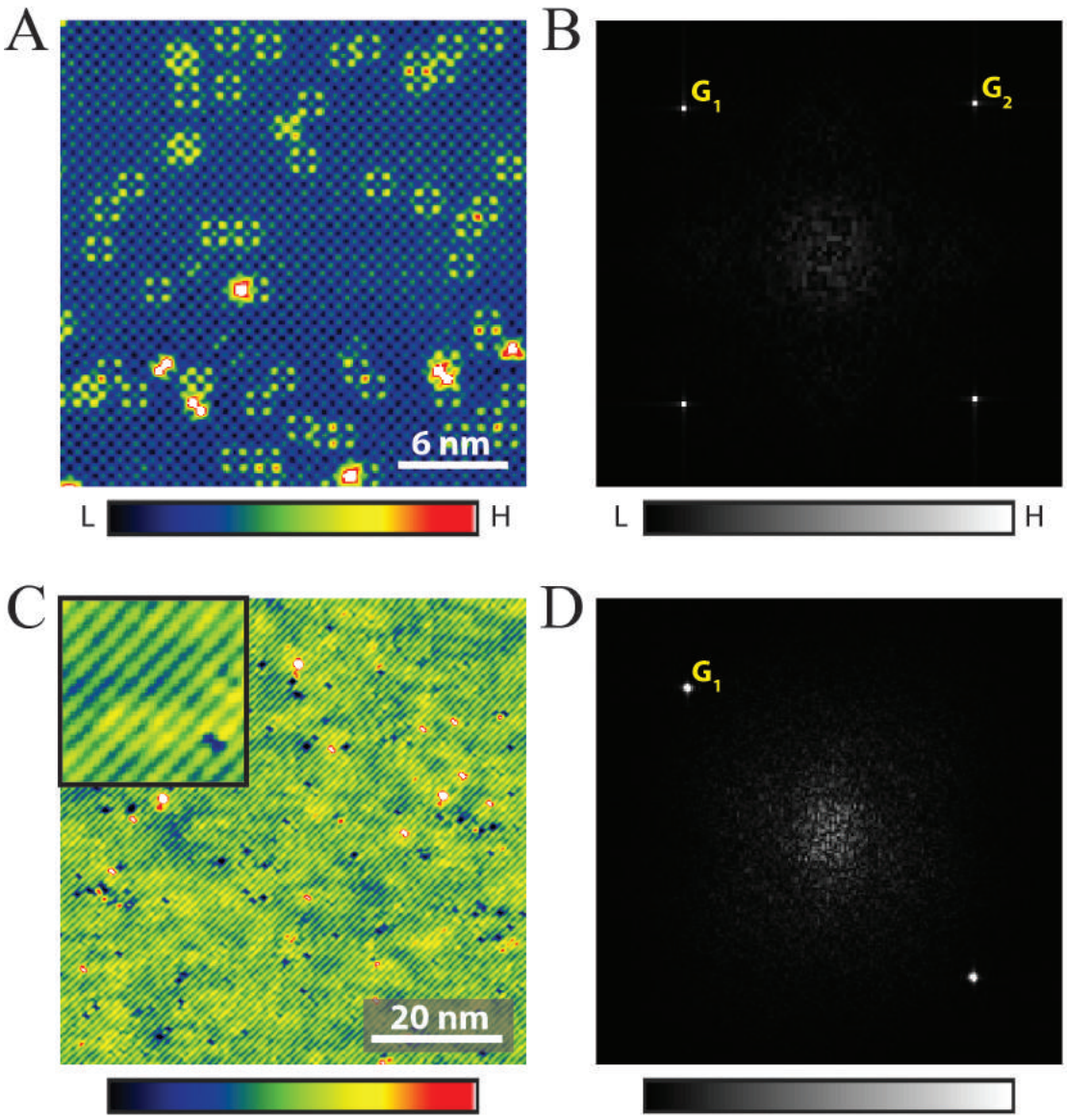

Figure 5.2: Example STM Topographs with atomic contrast. A, Topograph $T(\vec{r})$ of URu_2Si_2 surface. **B,** The amplitude of the Fourier transform $|\tilde{T}(\vec{q})|$ of **A**. The ratio of two Fourier amplitudes at Bragg peaks, $|\frac{\tilde{T}(\vec{G_1})}{\tilde{T}(\vec{G_2})}| = 1.03$, implies that the structure factor maintains the tetragonal symmetry of the crystal. **C,** Topograph of ferropnictide 122 $Ca(Fe_{1-x}Co_x)_2As_2$ with resolution 512 pixels. The atomic contrast is unidirectional due to the 1x2 surface reconstruction [110]. **D,** The amplitude of the Fourier transform of **C**. Only one Bragg peak is visible.

5.2 shows STM topographs acquired on two different materials. Fig. 5.2A and B show a topograph and its Fourier transform acquired on the surface of a tetrag-

onal system, URu_2Si_2 [111]. As expected, the atoms appear symmetric implying that the structure factor of the real space image obeys the tetragonal symmetry. Fig. 5.2C and D show a topograph and its Fourier transform acquired on the surface of $Ca(Fe_{1-x}Co_x)_2As_2$ in its orthorhombic phase [110]. Due to the 1x2 surface reconstruction in this material, the topograph shows modulations commensurate with the lattice along one direction but not the other. In the framework of this chapter, the structure factor associated with this image is highly anisotropic between two orthogonal directions. It is localized along one direction and delocalized along the other.

Now we will consider a representation of a Fourier transform of an atomically resolved STM image and see that the Fourier transform of structure factor takes center stage.

5.1.2 Fourier space

To elucidate the connection between the Bragg peak intensities and the structure factor, we Fourier transform Eq 5.1.

$$\tilde{I}(\vec{q}) = \tilde{F}(\vec{q}) \sum_{n_1,n_2} e^{-i\vec{q}\cdot(n_1\vec{a}_1+n_2\vec{a}_2)} = \tilde{F}(\vec{q}) \sum_i \delta(\vec{q}-\vec{G}_i) \tag{5.2}$$

Here $\vec{G}_i \equiv n_1\vec{b}_1 + n_2\vec{b}_2$ is generic reciprocal lattice vector (also Bragg wavevector) with $\vec{b}_1$ and $\vec{b}_2$ representing the primitive reciprocal vectors. As shown in Eq. 5.2, the Bragg peak amplitudes are modulated by the Fourier transform of the structure factor $\tilde{F}(\vec{q}) \equiv \int d\vec{r} e^{-i\vec{q}\cdot\vec{r}} F(\vec{r})$. Alternatively, we can state that the Fourier transform of the periodic (i.e. free of defects) STM image is the Fourier transform of the corresponding structure factor sampled at the reciprocal lattice

vectors. If the STM image is not free of defects, this discussion still applies to the analysis of its periodic component.

5.1.3 Rotational symmetry breaking

The description of a LDOS STM image can be generalized by allowing the structure factor to vary as a function of position. For example, in a nematic system with a domain boundary, we can expect two different functions $F_{domain\ A}(\vec{r})$ and $F_{domain\ B}(\vec{r})$ to describe the local structure of the image $I(\vec{r})$ far away from the boundary depending on the domain. Here we examine the phenomenon of *nematicity* (rotational symmetry breaking) in STM images in detail.

In context of Eq 5.2, if a rotational symmetry is broken along some two directions corresponding to otherwise equivalent (same order) Bragg wavevectors $\vec{G}_1$ and $\vec{G}_2$, then we have $\tilde{F}(\vec{G}_1) \neq \tilde{F}(\vec{G}_2)$ and $\tilde{I}(\vec{G}_1) \neq \tilde{I}(\vec{G}_2)$. For the moment, we rewrite Eq 5.1 to emphasize just these two particular and inequivalent wavevectors in the image $I(\vec{r})$.

$$I(\vec{r}) = \tilde{F}(\vec{G}_1)\cos(\vec{G}_1 \cdot \vec{r}) + \tilde{F}(\vec{G}_2)\cos(\vec{G}_2 \cdot \vec{r}) + \text{other terms} \tag{5.3}$$

To describe position dependent structure factor, we introduce a spatial variation into the relative magnitudes of two sinusoids and generalize Eq 5.3 as follows.

$$I(\vec{r}) = A_1(\vec{r})\cos(\vec{G}_1 \cdot \vec{r}) + A_2(\vec{r})\cos(\vec{G}_2 \cdot \vec{r}) + ... \tag{5.4}$$

Here $A_1(\vec{r})$ and $A_2(\vec{r})$ are slowly varying functions of position.

By specifying functions $A_1(\vec{r})$ and $A_2(\vec{r})$, a STM image with two nematic domains is simulated and shown in Fig. 5.3. The domain boundary is located on

the diagonal that starts from the lower left corner. Far away from the domain boundary, $A_1(\vec{r})$ and $A_2(\vec{r})$ are nearly constant and equal to 1 and 2 respectively in one domain, but 2 and 1 in the other. Across the boundary, $A_1(\vec{r})$ and $A_2(\vec{r})$ slowly change values. As a result, the atoms are symmetric at the boundary but appear stretched in one direction in one domain and in the other direction in the other domain. In this image with domains the structure factor is nematic and has spatial dependence.

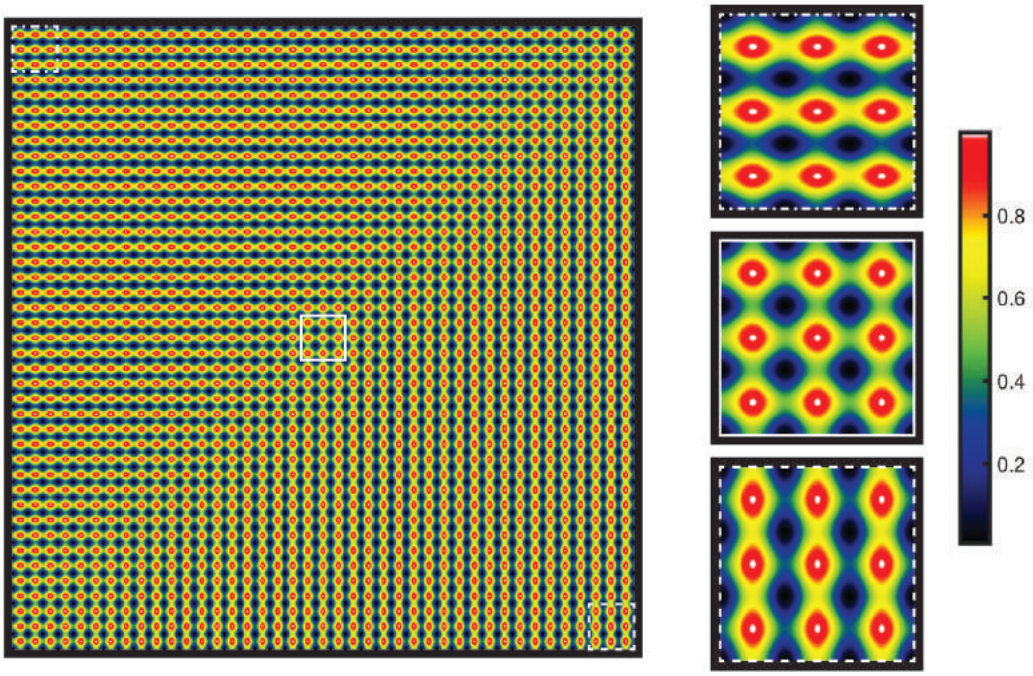

Figure 5.3: Example of a nematic image with the twin boundary. Nematic lattice image given by $I(x,y) = A_1(x,y)\cos(x) + A_2(x,y)\cos(y)$. The ratio $\frac{A_1}{A_2}$ varies going between top left and bottom right corners. The smaller sections of the image are displayed on the right emphasizing the variation of the local structure of the image as a function of position.

In the Fourier space, the spatial dependence of structure factor smears the Bragg peaks. Fig. 5.4 shows the amplitude of Fourier transform of the simulated image $I(x,y)$ shown above. There are four Bragg peaks corresponding to $\cos(x)$ and $\cos(y)$. A set of small wavevectors found around the Bragg peaks is a result

of spatial variations of $A_1(x, y)$ and $A_2(x, y)$.

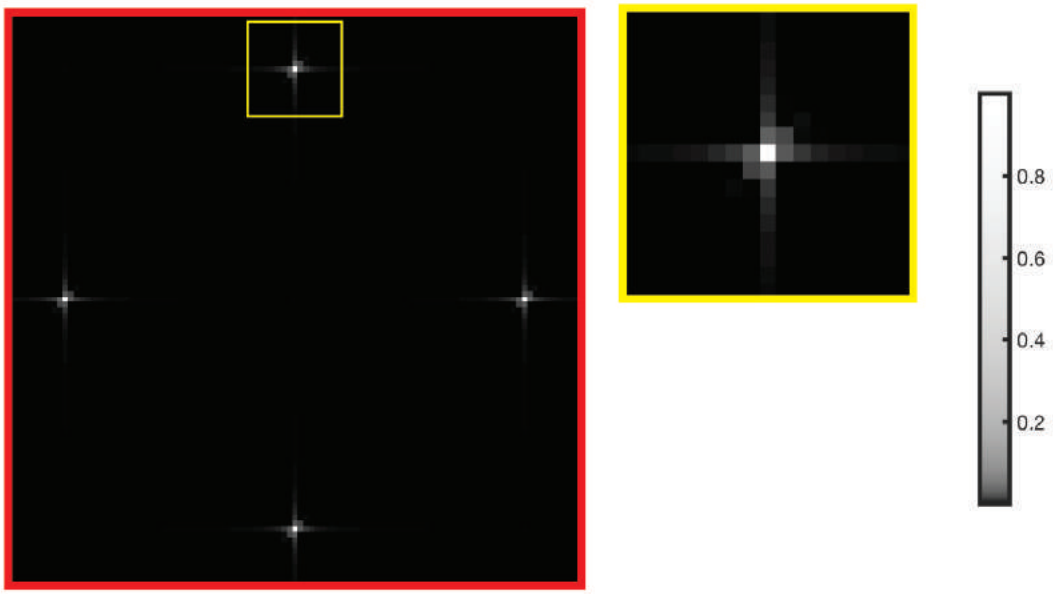

Figure 5.4: Fourier transform of nematic image with the twin boundary. Amplitude of the Fourier transform of the image from Fig. 5.3. The sharp Bragg peaks become blurred due to the spatial variation of the structure factor as described in the text.

We can use this formalism to define a nematic order parameter.

$$N(\vec{r}) = \frac{|A_1(\vec{r})| - |A_2(\vec{r})|}{|A_1(\vec{r})| + |A_2(\vec{r})|} \tag{5.5}$$

Note that $N(\vec{r})$ is spatially dependent. Its magnitude represents the local magnitude of anisotropy of the structure factor relative to the two directions specified by wavevectors $\vec{G}_1$ and $\vec{G}_2$, and its sign identifies the local orientation of the anisotropic structure factor. In context of Fig. 5.3, the nematic order parameter is positive in one domain and negative in the other.

5.1.4 Nematic order parameter

In order to visualize local symmetry breaking in STM data images, an algorithm for extracting the nematic order parameter $N(\vec{r})$ from data needs to be specified. We can start by expressing Eq 5.4 as a formal Fourier series substituting $\sum_{\vec{q'}} c_n(\vec{q'})e^{i\vec{q'}\cdot\vec{r}}$ for $A_n(\vec{r})$.

$$\begin{aligned} I(\vec{r}) &= A_1(\vec{r})\left(\frac{e^{i\vec{G}_1\cdot\vec{r}}+e^{-i\vec{G}_1\cdot\vec{r}}}{2}\right)+A_2(\vec{r})\left(\frac{e^{i\vec{G}_2\cdot\vec{r}}+e^{-i\vec{G}_2\cdot\vec{r}}}{2}\right)+... \\ &= \left(\sum_{\vec{q'}} c_1(\vec{q'})e^{i\vec{q'}\cdot\vec{r}}\right)\left(\frac{e^{i\vec{G}_1\cdot\vec{r}}+e^{-i\vec{G}_1\cdot\vec{r}}}{2}\right)+\left(\sum_{\vec{q'}} c_2(\vec{q'})e^{i\vec{q'}\cdot\vec{r}}\right)\left(\frac{e^{i\vec{G}_2\cdot\vec{r}}+e^{-i\vec{G}_2\cdot\vec{r}}}{2}\right)+... \\ &= \sum_{\vec{q'}} c_1(\vec{q'})e^{i(\vec{q'}+\vec{G}_1)\cdot\vec{r}}+\sum_{\vec{q'}} c_2(\vec{q'})e^{i(\vec{q'}+\vec{G}_2)\cdot\vec{r}}+... \end{aligned} \tag{5.6}$$

Since $A_1(\vec{r})$ and $A_2(\vec{r})$ are slowly varying functions of position, all significant $\vec{q'}$ vectors in their Fourier decompositions are small. Hence, if the structure factor has position dependence, the Bragg peaks at $\pm\vec{G}_1$ and $\pm\vec{G}_2$ are smeared in Fourier space over some region defined by these $\vec{q'}$ wavevectors.

Keeping Eq 5.6 in mind, we consider the Fourier transform of the STM data image $\tilde{I}(\vec{q})$. We can multiply $\tilde{I}(\vec{q})$ by a mask centered around specified Bragg peak $\vec{G}_j$ to selectively pick out the Fourier components associated with $A_j(\vec{r})$.

$$\tilde{I}_{\vec{G}_j}(\vec{q}) = M_{\vec{G}_j}(\vec{q})\tilde{I}(\vec{q}) \tag{5.7}$$

The mask $M_{\vec{G}_n}(\vec{q})$ is 1 in the vicinity of $\vec{G}_n$ and 0 elsewhere. Now if the size of the mask is set appropriately, we can identify $\tilde{I}_{\vec{G}_1}(\vec{q})$ and $\tilde{I}_{\vec{G}_2}(\vec{q})$ with $c_1(\vec{q'}+\vec{G}_1)$ and $c_2(\vec{q'}+\vec{G}_2)$. Then the amplitudes of the inverse Fourier transform of the masked Fourier images $\tilde{I}_{\vec{G}_j}(\vec{q})$ are simply equivalent to the amplitudes of $A_j(\vec{r})$.

$$\left|I_{\vec{G}_j}(\vec{r})\right| \equiv \left|\sum_{\vec{q}} c_j(\vec{q})e^{i(\vec{q}+\vec{G}_j)\cdot\vec{r}}\right| = \left|e^{i\vec{G}_j\cdot\vec{r}}\sum_{\vec{q}} c_j(\vec{q})e^{i\vec{q}\cdot\vec{r}}\right| = \left|\sum_{\vec{q}} c_j(\vec{q})e^{i\vec{q}\cdot\vec{r}}\right| = \left|A_j(\vec{r})\right| \tag{5.8}$$

Finally, we can compute the nematic order parameter using the definition Eq. 5.5.

$$N(\vec{r}) = \frac{\left|I_{\vec{G}_1}(\vec{r})\right| - \left|I_{\vec{G}_2}(\vec{r})\right|}{\left|I_{\vec{G}_1}(\vec{r})\right| + \left|I_{\vec{G}_2}(\vec{r})\right|} \tag{5.9}$$

The discussion above provides a method of generating the nematic order parameter from a STM data image. This method is summarized and illustrated in Fig. 5.4. In the next section, I will apply these techniques to actual STM images of nematic superconductor FeSe.

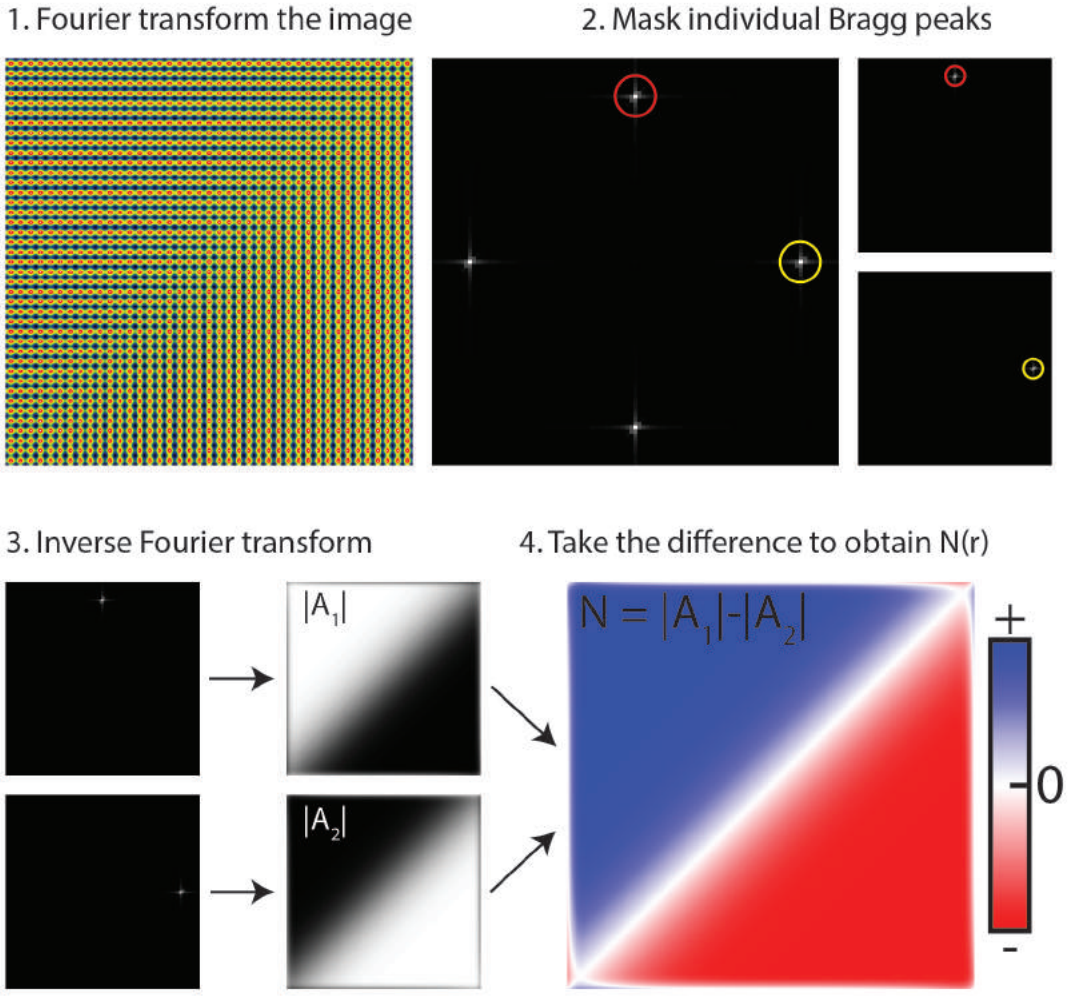

Figure 5.5: Algorithm for extracting nematic order parameter $N(\vec{r})$.

5.2 Intra Unit Cell Studies of FeSe

In this section, I will apply methods of the previous section to the analysis of STM topographs acquired on the surface of FeSe superconductor in the nematic phase.

Fig. 5.6A shows a high resolution STM topograph of a field of view with the domain boundary identifiable by an enhanced density of states. The x and y axes represent the longer and shorter orthorhombic axes respectively, and they naturally rotate by 90 degrees across the boundary. One region free of defects (at least at topmost layer) is selected from each domain. High resolution topographs of these regions are shown in Fig. 5.6B and C. It is evident that the unit cells are not C_4 symmetric. Recall that the topographs are proportional to the logarithm of the integrated density of states (IDOS) (Section 2.2.1). Locally the brighter regions of higher IDOS appear stretched along the x axis, and the darker regions of lower IDOS are stretched along the y axis. The structure factor of IDOS images in the nematic phase breaks the tetragonal symmetry.

Now we examine these IDOS images in the Fourier space. The Fourier transform of a topograph $T(\vec{r})$ will be denoted by $\tilde{T}(\vec{q})$. Fig. 5.7B shows the amplitude of the Fourier transform of the topograph from Fig. 5.6A. We identify two sets of reciprocal lattice vectors (Bragg peaks). The vectors $\vec{G}_a$ and $\vec{G}_b$ are oriented along Se directions, and the vectors $\vec{G}_c$ and $\vec{G}_d$ are oriented along Fe directions. (Fig. 5.7A identifies the Se and Fe directions.) Since the field of view contains both nematic domains in roughly equal proportions, the Bragg peaks for complementary directions have approximately equal intensities. That is $\left|\tilde{T}(\vec{G}_a)\right| \approx \left|\tilde{T}(\vec{G}_b)\right|$ and $\left|\tilde{T}(\vec{G}_c)\right| \approx \left|\tilde{T}(\vec{G}_d)\right|$. Fig. 5.7C then shows the amplitude

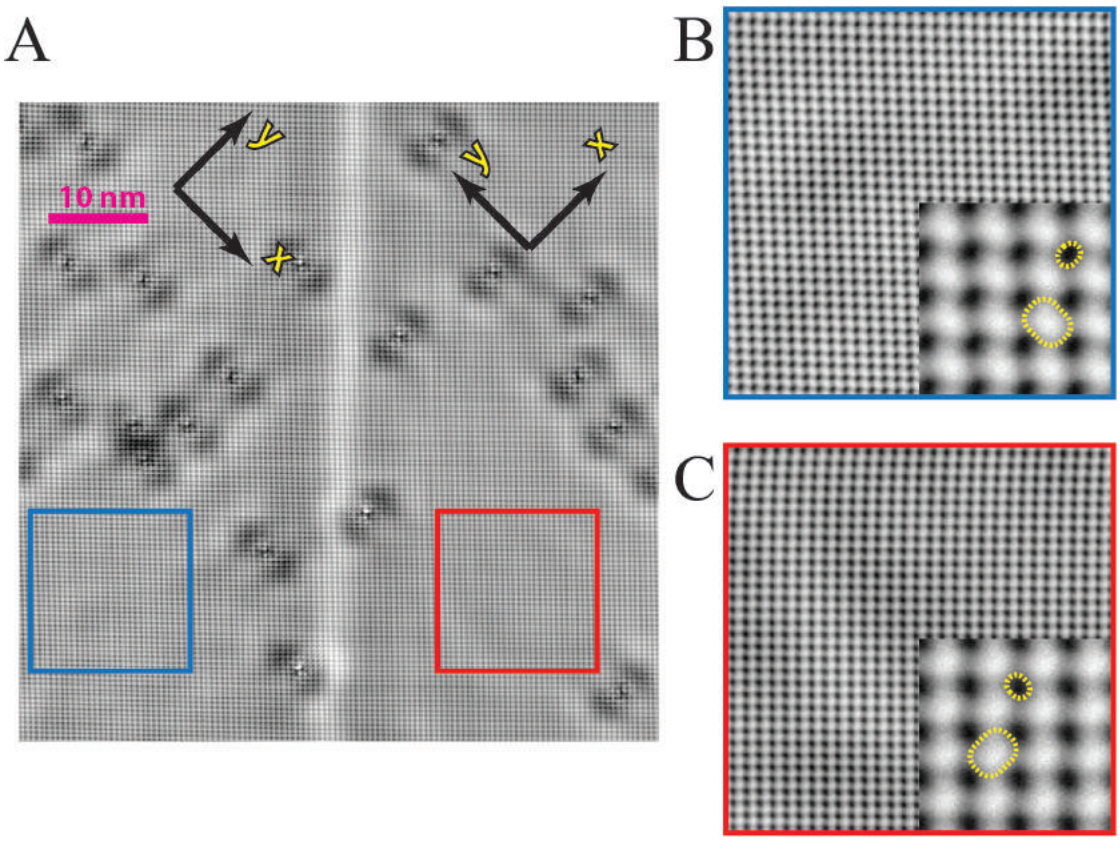

Figure 5.6: Rotational symmetry breaking in FeSe topographs. A, High resolution (1024 by 1024 pixels) topograph of a 64 nm FOV containing nematic domain boundary $T(\vec{r})$. The x and y axes are aligned with the longer and shorter orthorhombic axes, respectively. Two 16 nm single domain regions were selected and marked with blue and red squares. **B,** High resolution (1024 by 1024 pixels) topograph of the 'blue' region $T^B(\vec{r})$. **C,** High resolution (1024 by 1024 pixels) topograph of the 'red' region $T^R(\vec{r})$.

of the Fourier transform of the topograph of a 'blue' region (Fig. 5.6B). In this single domain image, $\left|\tilde{T}^B(\vec{G}_a)\right| \approx \left|\tilde{T}^B(\vec{G}_b)\right|$, but $\left|\tilde{T}^B(\vec{G}_c)\right| > \left|\tilde{T}^B(\vec{G}_d)\right|$. This means that the associated structure factor breaks the tetragonal symmetry and in particular distinguishes the two Fe directions. The Bragg peak along the shorter orthorhombic axis is suppressed. Likewise, Fig. 5.7D then shows the amplitude of the Fourier transform of the topograph of a 'red' region (Fig. 5.6C). Compared to the other domain, the Bragg peak anisotropy along Fe directions is reversed. That is $\left|\tilde{T}^R(\vec{G}_c)\right| < \left|\tilde{T}^R(\vec{G}_d)\right|$. Like in the other domain, the Se Bragg peaks

peaks have equal intensity. Since the directions corresponding to the longer and shorter orthorhombic axes are swapped between the two nematic domains, the Bragg peak suppression is still along the shorter orthorhombic axis as expected.

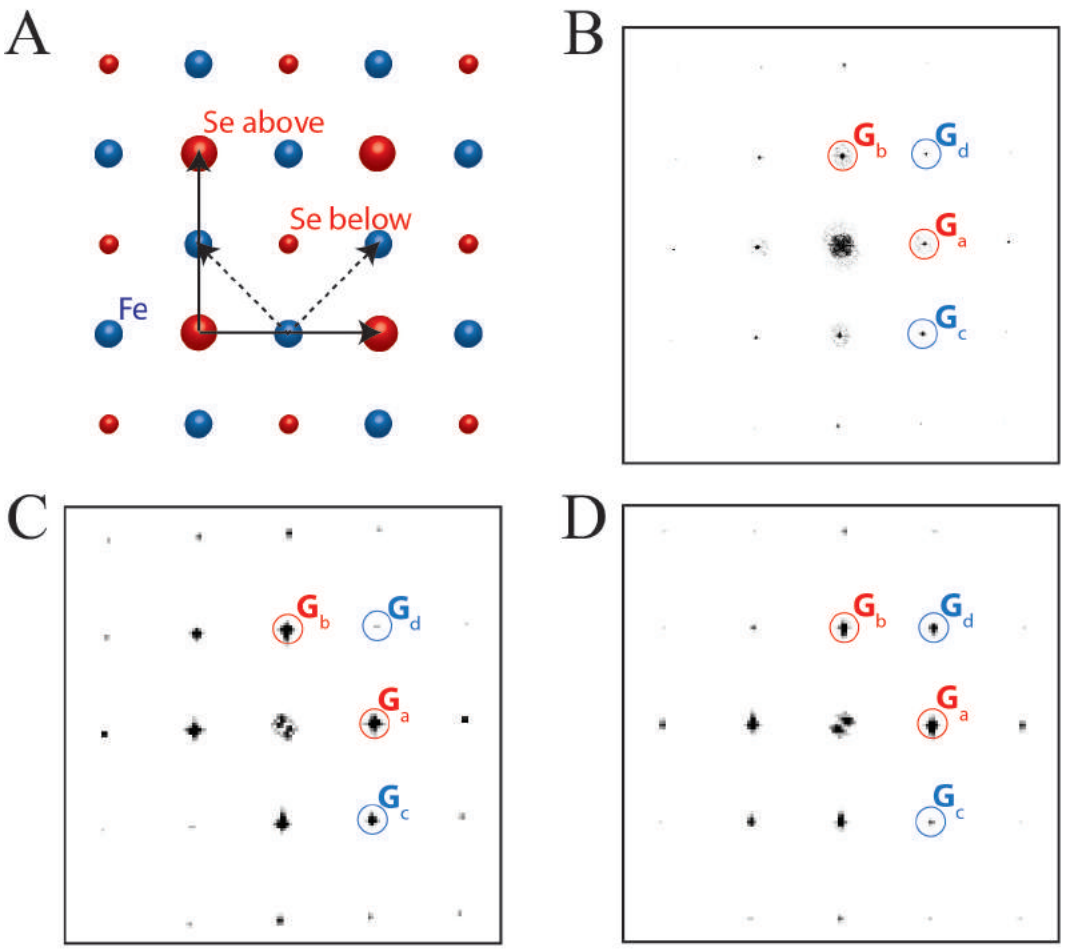

Figure 5.7: Fourier transforms of FeSe topographs. **A,** Planar view of FeSe structure. The solid and dashed arrows axis identify Se and Fe directions, respectively. **B,** Amplitude of the Fourier transform $\left|\tilde{I}(\vec{q})\right|$ corresponding to the topograph shown in Fig. 5.6A. **C,** Amplitude of the Fourier transform of the topograph of the 'blue' region $\left|\tilde{I}^{B}(\vec{q})\right|$. **D,** Amplitude of the Fourier transform of the topograph of the 'red' region' $\left|\tilde{I}^{R}(\vec{q})\right|$. The Fourier transform images in all panels were cropped to focus on lowest order Bragg peaks. The lowest order Bragg peaks $\vec{G}_a$ and $\vec{G}_b$ along Se-Se nearest neighbor directions are marked with red circles. The lowest order Bragg peaks $\vec{G}_c$ and $\vec{G}_d$ along Fe-Fe nearest neighbor directions are marked with blue circles.

After examining the topograph with the domain boundary (Fig. 5.6A) in real and Fourier space, we apply the algorithm for extracting the nematic order parameter (Section 5.1.4) to the same topograph. The Gaussian masks are used to pick out the Fourier components in the vicinity of Bragg peaks. The masked Fourier transform of the topograph with the mask centered around particular reciprocal lattice vector $\vec{G}$ is denoted by $\tilde{T}_{\vec{G}}(\vec{q})$. That is $\tilde{T}_{\vec{G}}(\vec{q}) = \exp\left(-\frac{\left|\vec{q}-\vec{G}\right|^2}{2\sigma^2}\right)\tilde{T}(\vec{q})$. Then $T_{\vec{G}}(\vec{r})$ is the Inverse Fourier transform $\left(\frac{1}{2\pi}\right)^2 \int d\vec{q} e^{i\vec{q}\cdot\vec{r}}\tilde{T}_{\vec{G}}(\vec{q})$. The symmetry breaking along Fe directions is then visualized locally by the following order parameter.

$$N_{Fe}(\vec{r}) = \frac{\left|T_{\vec{G}_c}(\vec{r})\right| - \left|T_{\vec{G}_d}(\vec{r})\right|}{\left|T_{\vec{G}_c}(\vec{r})\right| + \left|T_{\vec{G}_d}(\vec{r})\right|} \tag{5.10}$$

The resulting $N_{Fe}(\vec{r})$ images are shown in Fig. 5.8 for four different values of Fourier mask parameter σ. Bigger values of σ include spatial variations of shorter periodicity into the nematic order parameter, and the used values of 3, 5, 7 and 10 pixels for σ corresponds to cutoff wavelengths 21.3, 12.8, 9.1 and 6.4 nm respectively. All images clearly show that $N_{Fe}(\vec{r})$ abruptly changes sign across the domain boundary. The nematic order parameter images computed using the bigger Fourier masks (larger σ) also pick up quasiparticle interference at the defect sites. Recall from Chapter 3 that impurity scattering between states $|\vec{k}\rangle$ and $|\vec{k}+\vec{q}\rangle$ produces perturbations to local density of states with wavevectors of the form $\vec{q}+\vec{G}$ where $\vec{G}$ is reciprocal lattice vector. Some of these wavevectors are retained in $\tilde{T}_{\vec{G}}(\vec{q})$ if the mask is large enough. Fig. 5.9 shows the histograms of values derived from $N_{Fe}(\vec{r})$ images. They all show two well separated peaks corresponding to data from two different nematic domains. Aside from quasiparticle interference effects, the nematic parameter inside each domain is fairly uniform. Large values of $N_{Fe}(\vec{r})$ (close to ± 1) clearly show that the intra unit cell symmetry is broken along the two Fe directions.

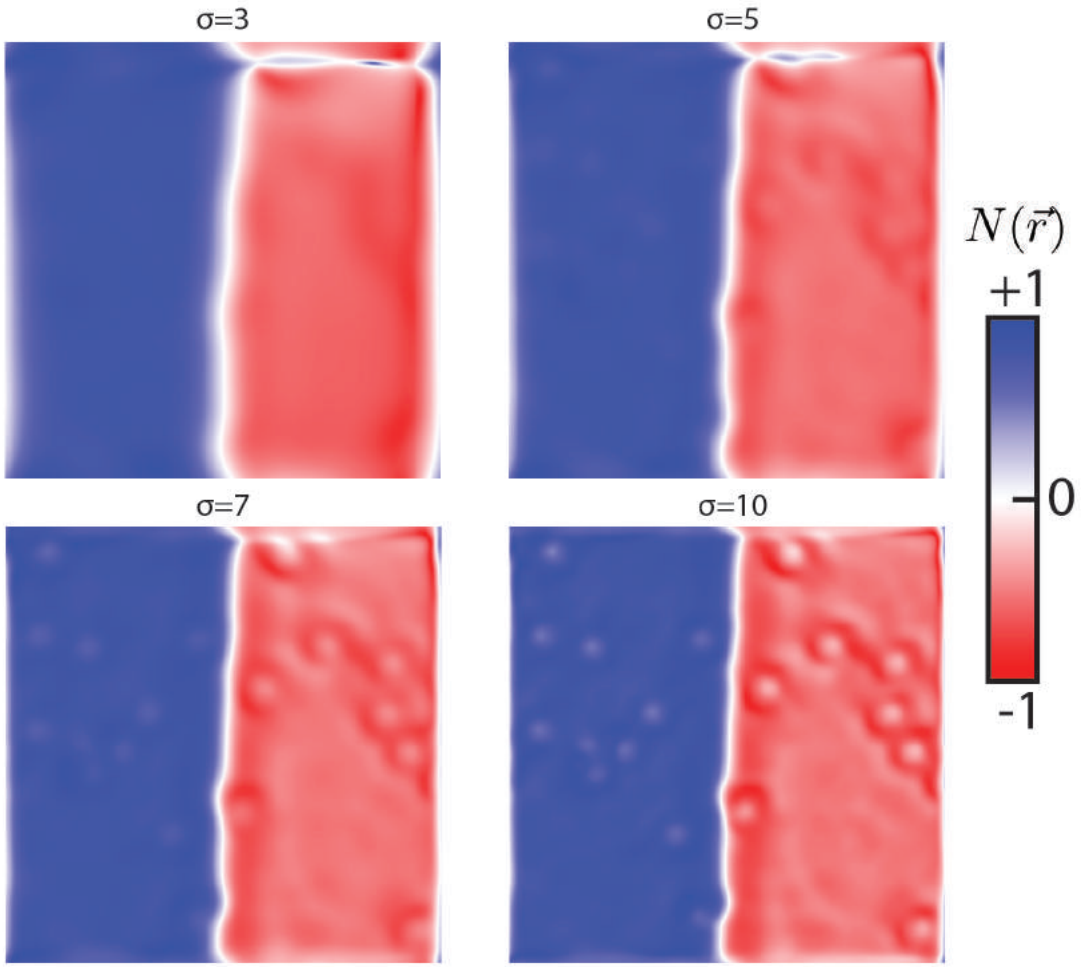

Figure 5.8: Nematic order parameter for Fe directions. The parameter σ is quoted in units of pixels.

Likewise, we can locally probe the symmetry breaking along Se directions and define $N_{Se}(\vec{r})$.

$$N_{Se}(\vec{r}) = \frac{\left|T_{\vec{G}_b}(\vec{r})\right| - \left|T_{\vec{G}_a}(\vec{r})\right|}{\left|T_{\vec{G}_b}(\vec{r})\right| + \left|T_{\vec{G}_a}(\vec{r})\right|} \tag{5.11}$$

The resulting $N_{Se}(\vec{r})$ images are shown in Fig. 5.10 for four different values of Fourier mask parameter σ. There is no sign change in $N_{Se}(\vec{r})$ across the boundary. $N_{Se}(\vec{r})$ is slightly negative everywhere in the field of view which means the Fourier components assigned to $\vec{G}_a$ Bragg peak are slightly larger than the ones assigned to $\vec{G}_b$. Since this anisotropy is in the same direction in both domains, it mostly likely comes from small asymmetry of the wave function at the end of

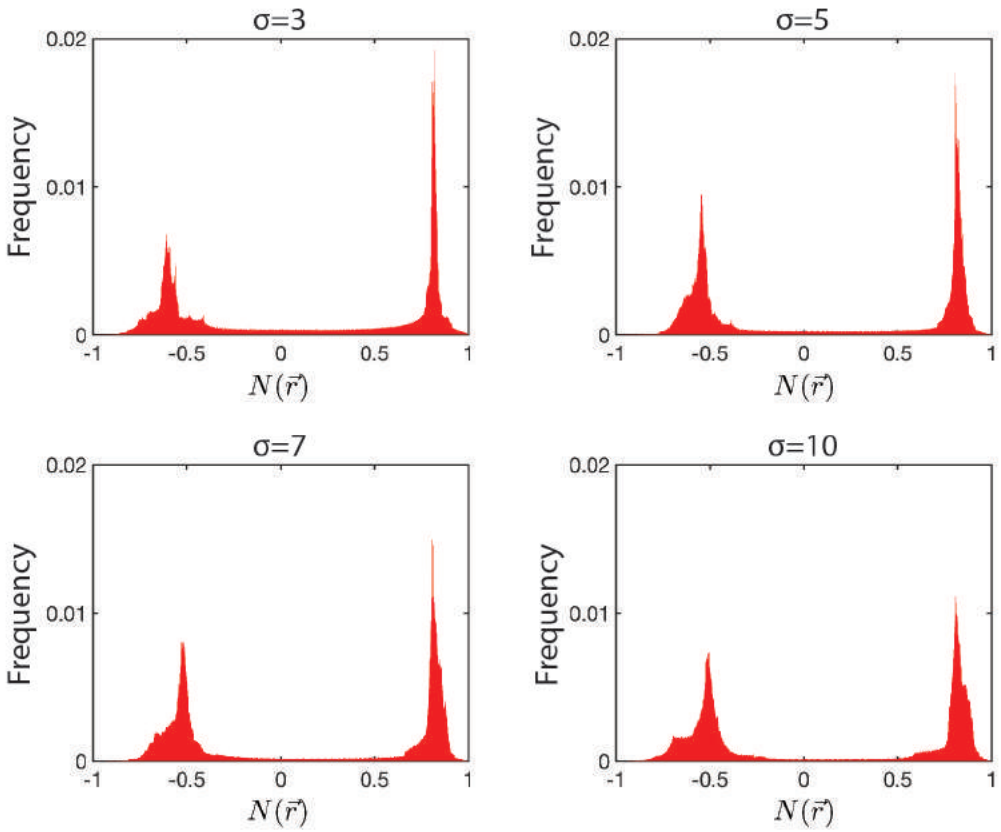

Figure 5.9: Histograms of nematic order parameter for Fe directions.

the STM tip. Again, quasiparticle interference becomes visible in images with bigger masks. Fig. 5.11 shows the histograms derived from $N_{Se}(\vec{r})$ images. The two peaks are visible especially for larger masks but they are not well separated. Overall, there is no symmetry breaking detected along the Se directions aside from the small systematic directionality due mostly likely to a particular slightly anisotropic electronic orbital at the end of STM tip.

The analysis above has revealed that the intra unit cell structure of atomically resolved DOS images in FeSe is very nematic, and the structure factor is anisotropic with respect to two Fe directions. In the next section, this observation will be discussed in context of orbital splitting in the electronic structure inferred from ARPES and QPI.

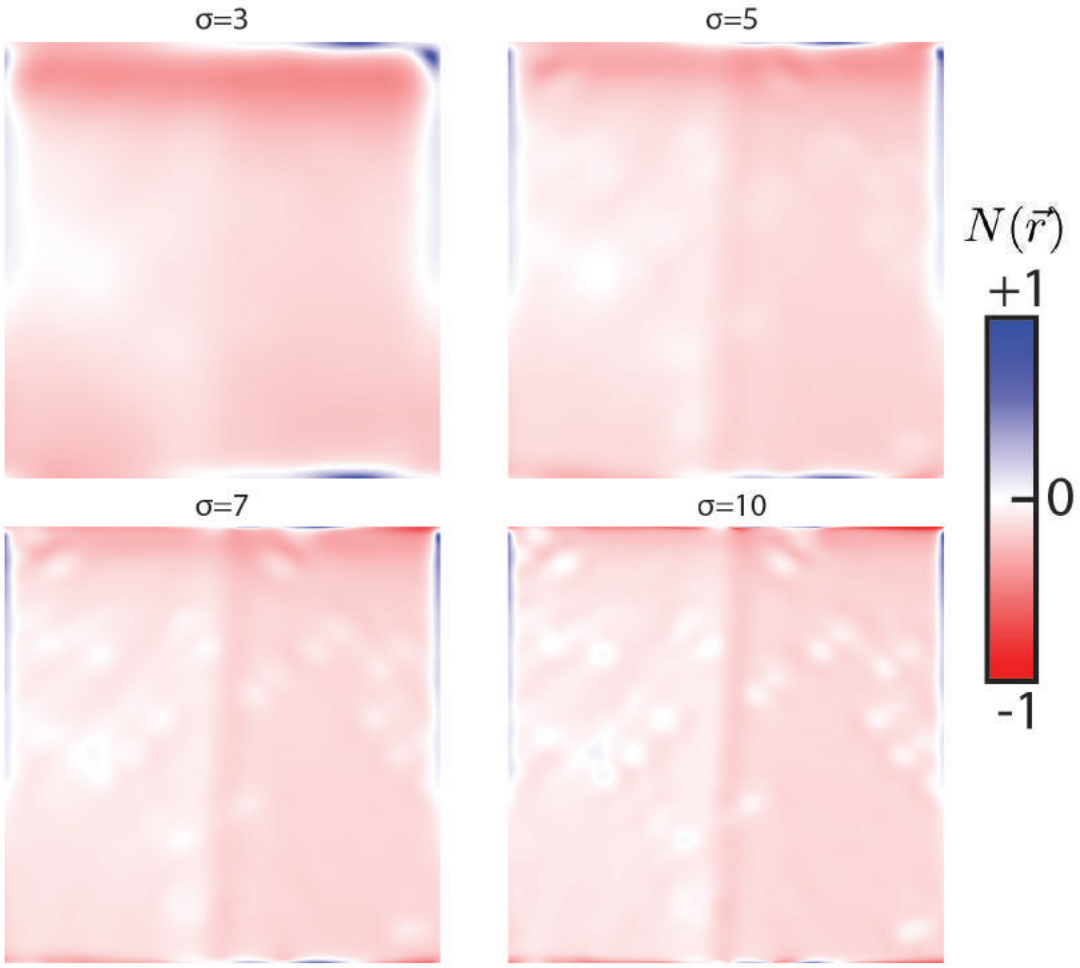

Figure 5.10: Nematic order parameter for Se directions. The parameter σ is quoted in units of pixels.

5.3 Discussion

Even in the nematic phase, the crystal structure of FeSe is almost tetragonal with orthorhombic distortion $\delta = (a - b)/(a + b)$ on order of 10^{-3} [54]. Despite such a small orthorhombic distortion the atoms in the DOS images appear substantially elongated, and the corresponding structure factor clearly breaks C_4 symmetry. This is not unexpected since the experimentally deduced electronic structure of FeSe strongly breaks the tetragonal symmetry in the nematic state. Specifically, previously degenerate d_{xz} and d_{yz} orbitals are split in energy

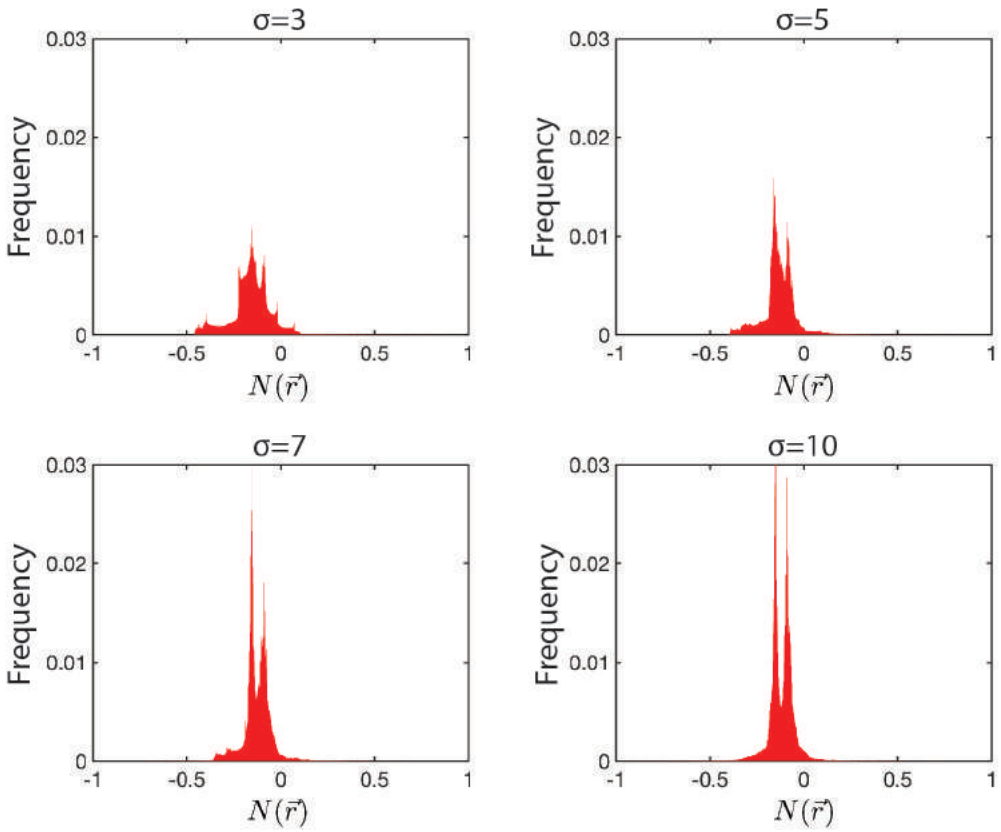

Figure 5.11: Histograms of nematic order parameter for Se directions.

below the structural transition. Moreover, this orbital splitting is momentum dependent [69]. This nematic state can be modeled theoretically by introducing symmetry-allowed bare nematic orders to the tetragonal Hamiltonian (i.e. $\hat{H}_{tot} = \hat{H}_{tetr} + \hat{H}_{nem}$) [106].

$$\begin{aligned}\hat{H}_{nem} = \sum_{\vec{k}} \delta_f \left(n_{xz}(\vec{k}) - n_{yz}(\vec{k})\right) + \delta_d \left(\cos(k_x) - \cos(k_y)\right)\left(n_{xz}(\vec{k}) + n_{yz}(\vec{k})\right) \\ + \delta_s \left(\cos(k_x) + \cos(k_y)\right)\left(n_{xz}(\vec{k}) - n_{yz}(\vec{k})\right)\end{aligned} \tag{5.12}$$

δ_f refers to the momentum independent ferro-orbital order (also called on-site orbital order). δ_d and δ_s refer to a d-wave and s-wave bond nematic orders, respectively. The tight binding parameterization for FeSe introduced in Chapter 1, gives values $(\delta_f, \delta_d, \delta_s) = (9.6, -8.9, 0)$ meV. Note that in particular that positive ferro-orbital order lowers energy and increases occupation of d_{yz} relative to

d_{xz} orbital.

All the relative shifts due to the onsite and bond orders and spin orbit coupling result in the Fermi surface of nematic FeSe having more states of d_{xz} orbital character relative to d_{yz} (see Fig. 1.12). One possible hypothesis is that the local periodic regions of higher density of states inside the LDOS images at low bias inherit the spatial characteristics of the d_{xz} Wannier states. Indeed in Fig 5.6, they point preferentially along the x axis. The highly anisotropic structure factor observed in STM images is likely a manifestation of orbital splitting arising as a consequence of nematic transition.

CHAPTER 6

SUMMARY AND RESEARCH OUTLOOK

6.1 Summary of Results

In almost every iron-based superconductor, the nematic ordering, if present, is followed by collinear antiferromagnetic ordering. The ordering temperature curves closely follow each other as a function of charge doping which suggests that the two orders are linked and have the same microscopic origin. In this context the nematic state of FeSe is unique amongst other iron-based superconductors since it is not accompanied by any magnetic ordering at ambient pressure [55]. ARPES studies on detwinned FeSe crystals indicate that the nematic state is associated with the momentum dependent splitting of the d_{xz} and d_{yz} orbital energies [69,70]. This suggests that the nematic ordering in FeSe is a complex phenomenon associated with several nematic order parameters [106]. Closely related to the question of nematic and magnetic order is if strong correlations are essential to the diverse physics observed in iron-based superconductors [3].

In this thesis, I presented STM studies of the nematic state of FeSe. The measured quasiparticle interference patterns revealed that strong orbital-selective correlations exist in the nematic state, and specifically that the quasiparticle weights follow $Z_{yz} \gg Z_{xz} > Z_{xy}$. Also, using a novel method to visualize nematicity in iron-based superconductors it was shown that, despite very small orthorhombic lattice distortion, the atomic structure of the local density of states in FeSe exhibits a very strong breaking of the tetragonal symmetry of the high temperature phase.

6.2 Possible Directions for Future Research

I conclude this thesis with the brief discussion of the three possible ideas for future work in the use of STM data to further the understanding of the nematic and superconducting states of FeSe.

6.2.1 Quasiparticle Interference and Wannier functions

As discussed in Chapter 3, quasiparticle interference between two equal energy states $|\boldsymbol{k}_1\rangle$ and $|\boldsymbol{k}_2\rangle$ causes an oscillation in the local density of states (LDOS) with the wavevector $\boldsymbol{q} = \boldsymbol{k}_1 - \boldsymbol{k}_2$. Since Bloch wavefunctions are periodic in $\boldsymbol{k}$-space, LDOS oscillations with wavevectors $\boldsymbol{q} = \boldsymbol{k}_1 - \boldsymbol{k}_2 + \boldsymbol{G}$, where $\boldsymbol{G}$ is a reciprocal lattice vector, should also be expected.

Fig. 6.1 shows the amplitude of the Fourier transform of the high resolution dI/dV image at the bias voltage -10 mV. I would like to draw the reader's attention to the three regions marked by solid yellow squares. Close to $\boldsymbol{q} = 0$, there is the anisotropic quasiparticle interference signal due to the intraband scattering assigned to the hole-like α-band. This QPI signal and its anisotropy were discussed in detail in Chapter 4. As expected from the mentioned periodicity of the Bloch states in the reciprocal space, there are also QPI patterns surrounding both Bragg peaks. However, note that they are not perfect replicas of the primary pattern at the origin. Instead, these patterns show substantial left-right asymmetry. To my knowledge, this particular QPI asymmetry is unique to the nematic state of FeSe and have not been explained theoretically thus far.

The calculation of the QPI amplitudes around the Bragg peaks involves the

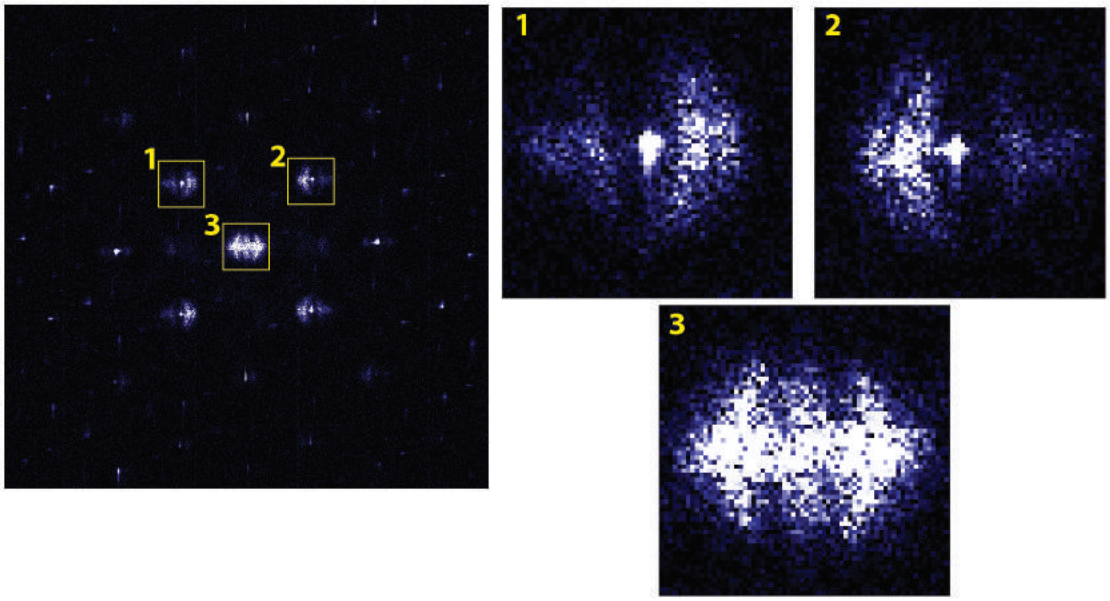

Figure 6.1: Fourier transform of the high resolution single layer dI/dV map. Left, The amplitude of the Fourier transform of high resolution dI/dV map at a single energy $E = -10$ meV. The map resolution is 1000 pixels, and the associated FOV size in real space is 71 nm. **Right,** Magnified regions of interest selected from the full Fourier transform.

continuum Green's function that depends on the Wannier functions describing the electronic states [112]. For a single band system the associated formula for the QPI response in $\boldsymbol{q}$-space is provided below (for derivation, see [113]).

$$n(\boldsymbol{q}, \omega) = i \sum_{\boldsymbol{k}} W(\boldsymbol{k}) W^*(\boldsymbol{k} + \boldsymbol{q}) G_{\overline{\boldsymbol{k}}, \overline{\boldsymbol{k}+\boldsymbol{q}}}(\omega) \tag{6.1}$$

Here $n(\boldsymbol{q}, \omega)$ is the Fourier transform of the LDOS and $W(\boldsymbol{k})$ is the Fourier-transformed Wannier function. The $\boldsymbol{k}$ sum runs over all wavevectors, and the notation $\overline{\boldsymbol{k}} \equiv \boldsymbol{k} \bmod \boldsymbol{G}$ defines $\boldsymbol{k}$-vectors translated to the first Brillouin zone. The retarded lattice Green's function $G_{\boldsymbol{k},\boldsymbol{k}+\boldsymbol{q}}(\omega)$ can be computed from the band-structure within the T-matrix approximation. From the expression above, it is clear that the relative QPI amplitudes depend on how localized the Wannier functions are in real space. In the most extreme limit where the Wannier function is a delta function in real space, its Fourier transform is unity everywhere

in $\boldsymbol{q}$-space, and the calculation reduces to the case of the lattice model for the density of states. The QPI patterns around the Bragg peaks are then the exact replicas of the QPI pattern near $\boldsymbol{q} = 0$. Away from this fully localized limit, the Wannier functions suppress the QPI amplitudes near the Bragg peaks relative to the amplitudes near $\boldsymbol{q} = 0$.

In my opinion, the multi-orbital generalization of the expression above is a promising starting point for theoretically modeling the result of the STM measurement presented in Fig. 6.1. An interesting research question is what is the relationship, if any, between nematicity and the peculiar asymmetric shape of the QPI response in the vicinity of the reciprocal lattice vectors.

6.2.2 Impurity States

Another unsettled problem in STM research of the nematic phase of FeSe is the calculation of dI/dV spectra in the vicinity of the iron-centered defects. Some representative spatially resolved spectra near a defect site are shown in Fig. 6.2.

In the vicinity of the defect, the spectra show two peaks at approximately -20 and +12 meV. Within the experimental resolution, these energies correspond to the tops of the two hole-like bands. The simplest explanation for these peaks is the scattering resonance resulting from the divergence of the T-matrix at some energies. For example, if the matrix describing the impurity is diagonal in orbital space, the T-matrix is given by $\hat{T}(E) = V_0\hat{I}[\hat{I} - V_0 \sum_{\vec{k}} \hat{G}_0(\vec{k}, E)]^{-1}$ where V_0 is the impurity potential. The determinant of $\hat{I} - V_0 \sum_{\vec{k}} \hat{G}_0(\vec{k}, E)$ can approach zero at some energies resulting in the resonant scattering response. In this picture,

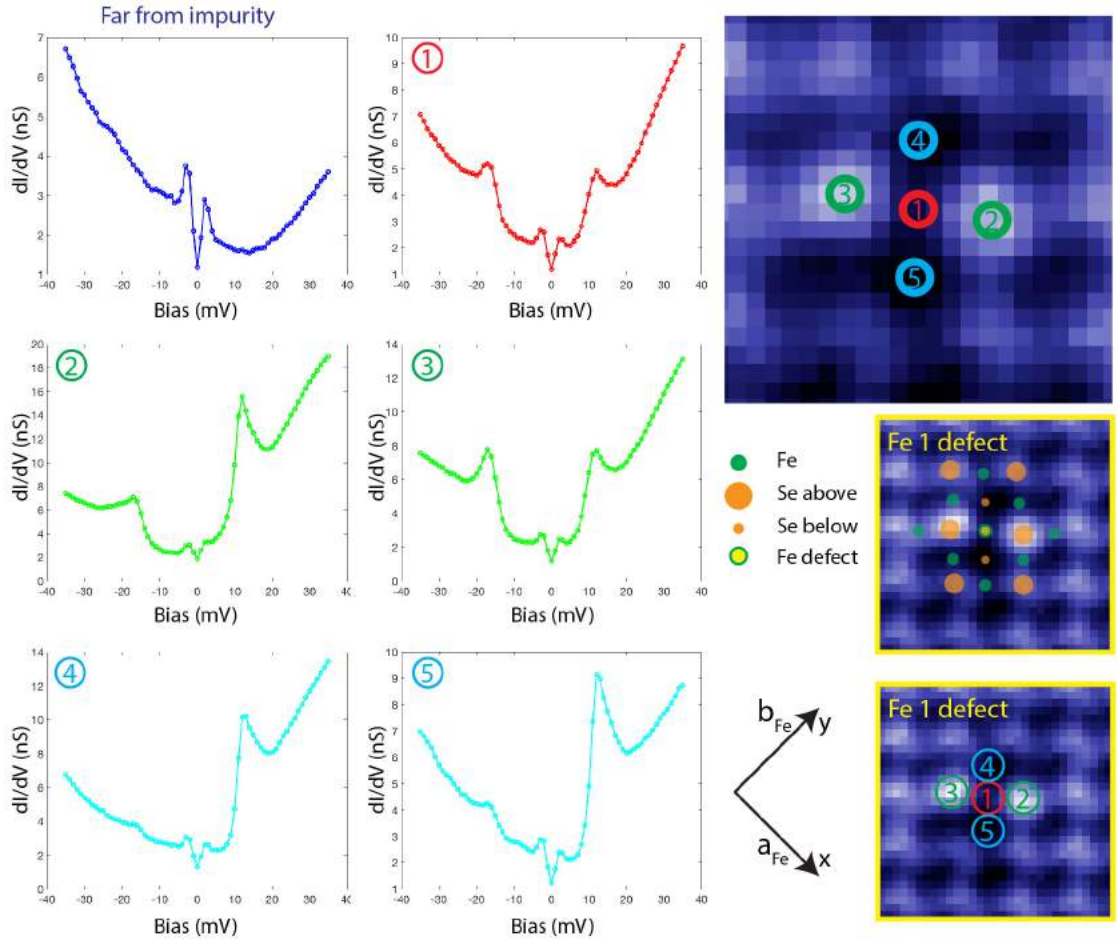

Figure 6.2: Representative dI/dV spectra near an iron defect site. The iron-centered defect is identified by the dimer structure where the two Se atoms in STM topograph closest to the defect appear brighter than the rest.

however, it is not clear why the peaks in the spectrum occur precisely when the bands close.

There is an interesting proposal that the ground state of FeSe is a nematic quantum paramagnet [63]. From the perspective of this theory, FeSe is viewed as a lattice of local spin-1 moments with strongly frustrated exchange interactions which drive the nematic ordering. Now suppose that the iron centered defects observed in STM are in fact iron vacancies. In the localized moments picture, the vacancies correspond to missing moments at the corresponding sites.

It is natural to ask how the density of states should be perturbed at short length scales in the vicinity of such a missing moment. If the local picture is correct, such a prediction should match the STM spectra in Fig. 6.5.

6.2.3 Caroli-deGennes states at the vortices of FeSe

Lastly, recent advances in the characterization of the superconducting state in FeSe [1, 51] naturally motivate a fresh look at the studies of superconducting vortices in FeSe. First STM studies of such vortices in FeSe were done on FeSe thin films [114]. It was found that the vortex cores are twofold symmetric suggesting that the superconducting gap is also twofold symmetric . The elongated direction of vortices is now identified as the longer orthorhombic axis. BQPI experiment recently revealed the structure of the twofold symmetric superconducting gap in $\boldsymbol{k}$-space. It is natural to use this new information as an input to the Bogoliubov-deGennes (BdG) calculation of the spatial structure of the bound Caroli-deGennes states inside the vortices in FeSe.

Fig. 6.3 shows STM measurements of the evolution of the spatial structure of the Caroli-deGennes states as a function of energy. Unidirectional dispersion along the shorter orthorhombic b_{Fe} axis is clear. A theoretical study of the vortices was done for a tetragonal iron based superconductor LiFeAs, and it showed remarkable agreement with experimental data [115]. The nematic version of the vortex problem is more complex, and it would be an important advancement in the understanding of superconductivity inside nematic systems if energy and spatially resolved structure of the nematic vortex states from STM studies can be reproduced theoretically.

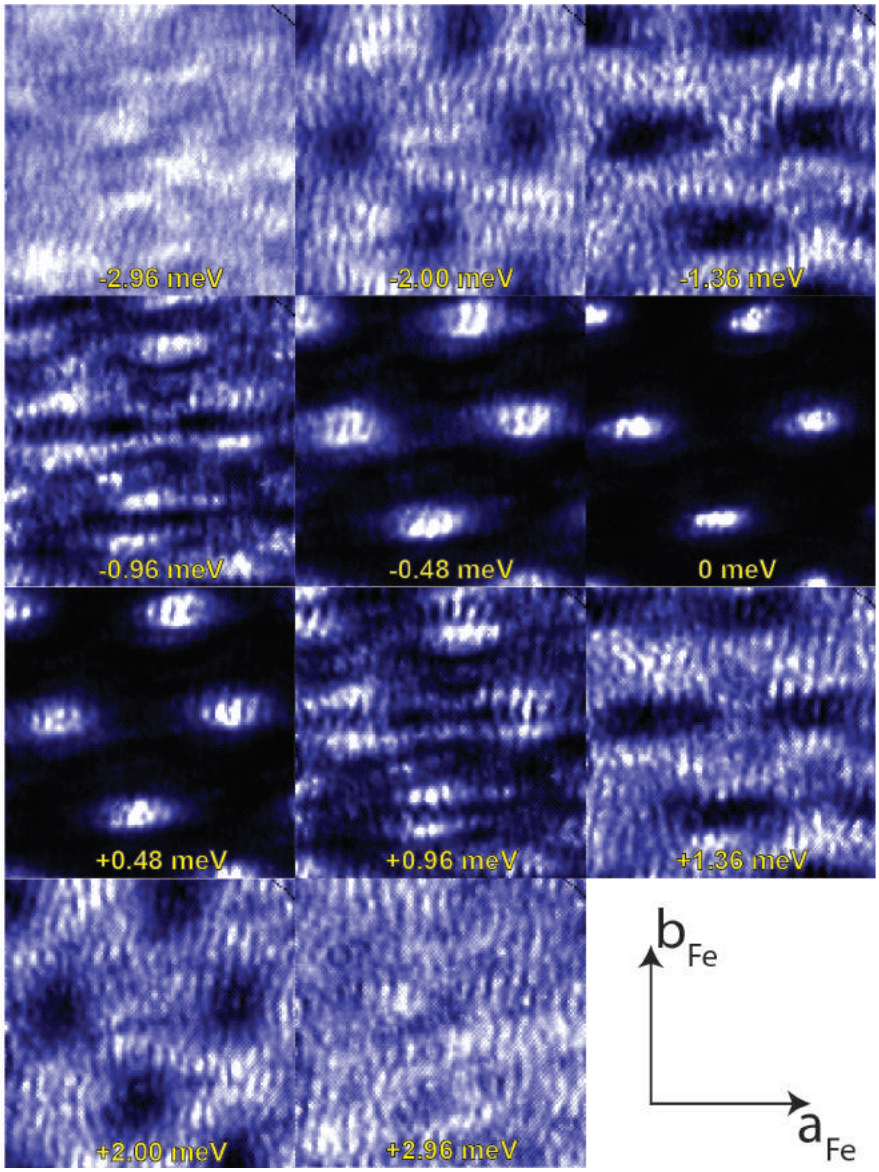

Figure 6.3: dI/dV spectroscopy of FeSe vortices. A sequence of dI/dV images showing several vortices at energies associated with superconductivity in FeSe (the maximum superconducting gap energy is 2.5 meV [1]).

BIBLIOGRAPHY

[1] P. O. Sprau, A. Kostin, A. Kreisel, A. Böhmer, V. Taufour, P. C. Canfield, S. Mukherjee, P. J. Hirschfeld, B. M. Andersen, and J. C. Davis. Discovery of orbitally-selective Cooper pairing in FeSe. *Science*, 357, 6346, 2017.

[2] L. de' Medici. *Iron-based Superconductivity - Weak and Strong Correlations in Fe Superconductors*, volume 211, 409-441 of *Springer Series in Materials Science*. Springer, 2015.

[3] Y.-Z. You and Z.-Y. Weng. *Iron-based Superconductivity - Coexisting itinerant and localized electrons*, volume 211, 377-408 of *Springer Series in Materials Science*. Springer, 2015.

[4] S. Graser, T. A. Maier, P. J. Hirschfeld, and D. J. Scalapino. Near-degeneracy of several pairing channels in multiorbital models for the Fe pnictides. *New Journal of Physics*, 11, 025016, 2009.

[5] P. W. Anderson. The Resonating Valence Bond State in La_2CuO_4 and Superconductivity. *Science*, 235, 1196, 1987.

[6] G. Baskaran. The Resonating Valence Bond Theory of Superconductivity: Beyond Cuprates. *Arxiv Preprint*, 1709.10070, 1987.

[7] Q. Si and E. Abrahams. Strong correlations and magnetic frustration in the high T_c iron pnictides. *Physical Review Letters*, 101, 076401, 2008.

[8] Q. Si, E. Abrahams, J. Dai, and Zhu J.-X. Correlation effects in the iron pnictides. *New Journal of Physics*, 11, 045001, 2009.

[9] I. I. Mazin, D. J. Singh, M. D. Johannes, and M. H. Du. Unconventional superconductivity with a sign reversal in the order parameter of lafeaso$_{1-x}$f$_x$. *Physical Review Letters*, 101, 057003, 2008.

[10] J. Hu and H. Ding. Local antiferromagnetic exchange and collaborative fermi surface as key ingredients of high temperature superconductors. *Nature Scientific Reports*, 2, 381, 2012.

[11] P. J. Hirschfeld. Using gap symmetry and structure to reveal the pairing mechanism in Fe-based superconductors. *Comptes Rendus Physique*, 17, 197–231, 2016.

[12] Y. Kamihara, H. Hiramatsu, M. Hirano, R. Kawamura, H. Yanagi, T. Kamiya, and H. Hosono. Iron-based layered superconductor: LaOFeP. *Journal of the American Chemical Society*, 128, 10012, 2006.

[13] Y. Kamihara, T. Watanabe, T. Hirano, and H. Hosono. Iron-based layered superconductor La[$O_{1-x}F_x$]FeAs (x=0.05-0.12) with T_c = 26 K. *Journal of the American Chemical Society*, 130, 3296–3297, 2008.

[14] Basov D. N. and A. V. Chubukov. Manifesto for higher T_c. *Nature Physics*, 7, 272–276, 2011.

[15] J. Paglione and R. L. Greene. High-temperature superconductivity in iron-based materials. *Nature Physics*, 6, 645–658, 2010.

[16] M. R. Norman. Superconductivity with a twist. *Physics*, 8, 24, 2015.

[17] P. Dai, H. Luo, and M. Wang. *Iron-based Superconductivity - Magnetic Order and Dynamics: Neutron Scattering*, volume 211, 161-186 of *Springer Series in Materials Science*. Springer, 2015.

[18] P. Dai, J. Hu, and E. Dagotto. Magnetism and its microscopic origin in iron-based high-temperature superconductors. *Nature Physics*, 8, 709–718, 2012.

[19] R. M. Fernandes, A. V. Chubukov, and J. Schmalian. What drives nematic order in iron-based superconductors? *Nature Physics*, 10, 97–104, 2014.

[20] P. J. Hirschfeld, M. M. Korshunov, and I. I. Mazin. Gap symmetry and structure of Fe-based superconductors. *Reports on Progress in Physics*, 74, 124508, 2011.

[21] F. Wang and D.-H. Lee. The Electron-Pairing Mechanism of Iron-Based Superconductors. *Science*, 332, 200-204, 2011.

[22] L. de' Medici. Hund's metals, explained. *Arxiv Preprint*, 1707.03282, 2017.

[23] A. Georges, L. de' Medici, and J. Mravlje. Strong correlations from Hund's coupling. *Annual Review of Condensed Matter Physics*, 4, 137–178, 2013.

[24] L. de'Medici, A. Georges, and S. Biermann. Orbital-selective Mott transition in multiband systems: Slave-spin representation and dynamical mean-field theory. *Phys. Rev. B*, 72, 205124, 2005.

[25] L. de' Medici and M. Capone. *Modeling Many-Body Physics with Slave-Spin Mean-Field: Mott and Hund's Physics in Fe-Superconductors*. Springer, 2017.

[26] Maria Chatzieleftheriou. Iron-based superconductors: Electronic correlations and orbital selectivity. Master's thesis, University of Copenhagen, Denmark, 2017.

[27] L. de' Medici. Hund's coupling and its key role in tuning multiorbital correlations. *Physics Review B*, 83, 205112, 2011.

[28] Z. P. Yin, K. Haule, and G. Kotliar. Kinetic frustration and the nature of the magnetic and paramagnetic states in iron pnictides and iron chalcogenides. *Nature Materials*, 10, 932–935, 2011.

[29] N. Lanatá, H. Strand, G. Giovannetti, B. Hellsing, L. de' Medici, and M. Capone. Orbital selectivity in Hund's metals: The iron chalcogenides. *Physical Review B*, 87, 045122, 2013.

[30] L. Fanfarillo and E. Bascones. Electronic correlations in Hund metals. *Physical Review B*, 92, 075136, 2015.

[31] L. de' Medici, G. Giovannetti, and M. Capone. Selective Mott Physics as a Key to Iron Superconductors. *Physics Review Letters*, 112, 177001, 2014.

[32] L. de' Medici. Hund's Induced Fermi-Liquid Instabilities and Enhanced Quasiparticle Interactions. *Physical Review Letters*, 118, 167003, 2017.

[33] A. Koga, N. Kawakami, T. M. Rice, and M. Sigrist. Orbital-Selective Mott Transitions in the Degenerate Hubbard Model. *Physical Review Letters*, 92, 216402, 2004.

[34] P. Werner and A. Millis. High-Spin to Low-Spin and Orbital Polarization Transitions in Multiorbital Mott Systems. *Physical Review Letters*, 99, 126405, 2007.

[35] P. Werner, E. Gull, and A. Millis. Metal-insulator phase diagram and orbital selectivity in three-orbital models with rotationally invariant Hund coupling. *Physical Review B*, 79, 115119, 2009.

[36] L. de' Medici, S. R. Hassan, M. Capone, and X. Dai. Orbital-Selective Mott Transition out of Band Degeneracy Lifting. *Physical Review Letters*, 102, 126401, 2009.

[37] R. Yu and Q. Si. Orbital-Selective Mott Phase in Multiorbital Models for Alkaline Iron Selenides $\mathbf{K}_{1-x}\mathrm{Fe}_{2-y}\mathrm{Se}_2$. *Physical Review Letters*, 110, 146402, 2013.

[38] R. Yu and Q. Si. Orbital-dependent effects of electron correlations in microscopic models for iron-based superconductors. *Current Opinion in Solid State and Materials Science*, 17, 65, 2013.

[39] R. Yu and Q. Si. Orbital-selective Mott phase in multiorbital models for iron pnictides and chalcogenides. *Physical Review B*, 96, 125110, 2017.

[40] M. Yi, D. H. Lu, R. Yu, S. C. Riggs, J. H. Chu, B. Lv, Z. K. Liu, M. Lu, Y. T. Cui, M. Hashimoto, S. K. Mo, Z. Hussain, C. W. Chu, I. R. Fisher, Q. Si, and Z. X. Shen. Observation of temperature-induced crossover to an orbital-selective mott phase in $A_xFe_{2-y}Se_2(A = K, Rb)$ superconductors. *Physical Review Letters*, 110, 067003, 2013.

[41] M. Yi, Z.-K. Liu, Y. Zhang, R. Yu, J.-X. Zhu, J. J. Lee, R. G. Moore, F. T. Schmitt, W. Li, S. C. Riggs, J.-H. Chu, B. Lv, J. Hu, M. Hashimoto, S.-K. Mo, Z. Hussain, Z.-Q. Mao, C. W. Chu, I. R. Fisher, Q. Si, Z.-X. Shen, and D. H. Lu. Observation of universal strong orbital-dependent correlation effects in iron chalcogenides. *Nature Communications*, 6, 7777, 2015.

[42] M. Yi, Y. Zhang, Z.-X. Shen, and D. Lu. Role of the orbital degree of freedom in iron-based superconductors. *npj Quantum Materials*, 2, 57, 2011.

[43] Z. K. Liu, M. Yi, Y. Zhang, J. Hu, R. Yu, J. X. Zhu, R. H. He, Y. L. Chen, M. Hashimoto, R. G. Moore, S. K. Mo, Z. Hussain, Q. Si, Z. Q. Mao, D. H. Lu, and Z. X. Shen. Experimental observation of incoherent-coherent crossover and orbital-dependent band renormalization in iron chalcogenide superconductors. *Physical Review B*, 92, 235138, 2015.

[44] Y. J. Pu, Z. C. Huang, H. C. Xu, D. F. Xu, Q. Song, C. H. P. Wen, R. Peng, and D. L Feng. Temperature-induced orbital selective localization and coherent-incoherent crossover in single-layer FeSe/Nb : $\mathrm{BaTiO_3/KTaO_3}$. *Physical Review B*, 94, 115146, 2016.

[45] Zhe Wang, M. Schmidt, J. Fischer, V. Tsurkan, M. Greger, D. Vollhardt, A. Loidl, and J. Deisenhofer. Orbital-selective metal-insulator transition and gap formation above T_c in superconducting $\mathrm{Rb}_{1-x}\mathrm{Fe}_{2-y}\mathrm{Se}_2$. *Nature Communications*, 5, 3202, 2014.

[46] X. Ding, Yi. Pan, H. Yang, and H.-H. Wen. Strong and nonmonotonic temperature dependence of Hall coefficient in superconducting $K_xFe_{2-y}Se_2$ single crystals. *Physical Review B*, 89, 224515, 2014.

[47] W. Li, C. Zhang, S. Liu, X. Ding, X. Wu, X. Wang, H.-H. Wen, and M. Xiao. Mott behavior in $K_xFe_{2-y}Se_2$ superconductors studied by pump-probe spectroscopy. *Physical Review B*, 89, 134515, 2014.

[48] P. Gao, R. Yu, L. Sun, H. Wang, Z. Wang, Q. Wu, M. Fang, G. Chen, J. Guo, C. Zhang, D. Gu, H. Tian, J. Li, J. Liu, Y. Li, X. Li, S. Jiang, K. Yang, A. Li, Q. Si, and Z. Zhao. Role of the 245 phase in alkaline iron selenide superconductors revealed by high-pressure studies. *Physical Review B*, 89, 094514, 2014.

[49] Q. Si, R. Yu, and E. Abrahams. High-temperature superconductivity in iron pnictides and chalcogenides. *Nature Reviews Materials*, 16017, 1–15, 2016.

[50] H. Bruus and K. Flensberg. *Many-body quantum theory in condensed matter physics - an introduction*. Oxford University Press, 2004.

[51] A. Kreisel, B. M. Andersen, P. O. Sprau, A. Kostin, J. C. Davis, and P. J. Hirschfeld. Orbital selective pairing and gap structures of iron-based superconductors. *Physical Review B*, 95, 174504, 2017.

[52] N. Arakawa and M. Ogata. Orbital-selective superconductivity and the effect of lattice distortion in iron-based superconductors. *Journal of the Physical Society of Japan*, 80, 074704, 2011.

[53] R. Yu, J.X. Zhu, and Q. Si. Orbital-selective superconductivity, gap anisotropy, and spin resonance excitations in a multiorbital $t - J_1 - J_2$-model for iron pnictides. *Physical Review B*, 89, 024509, 2014.

[54] K. Kothapalli, A. E. Böhmer, W. T. Jayasekara, B. G. Ueland, P. Das, A. Sapkota, V. Taufour, Y. Xiao, E. Alp, S. L. Bud'ko, P. C. Canfield, A. I. Kreyssig, and A. Goldman. Strong cooperative coupling of pressure-induced magnetic order and nematicity in FeSe. *Nature Communications*, 7, 12728, 2016.

[55] A. E. Böhmer and A. Kreisel. Nematicity, magnetism and superconductivity in FeSe. *Journal of Physics: Condensed Matter*, 30, 023001, 2017.

[56] S. Margadonna, Y. Takabayashi, M. T. McDonald, K. Kasperkiewicz,

Y. Mizuguchi, Y. Takano, A. N. Fitch, E. Suard, and K. Prassides. Crystal structure of the new $FeSe_{1-x}$ superconductor. *Chemical Communications*, 5607–5609, 2008.

[57] E. Pomjakushina, K. Conder, V. Pomjakushin, M. Bendele, and R. Khasanov. Synthesis, crystal structure, and chemical stability of the superconductor $FeSe_{1-x}$. *Physical Review B*, 80, 024517, 2009.

[58] M. A. Tanatar, A. E. Böhmer, E. I. Timmons, M. Schütt, G. Drachuck, V. Taufour, K. Kothapalli, A. Kreyssig, S. L. Bud'ko, P. C. Canfield, R. M. Fernandes, and R. Prozorov. Origin of the resistivity anisotropy in the nematic phase of FeSe. *Physical Review Letters*, 117, 127001, 2016.

[59] S. Ishida, M. Nakajima, T. Liang, K. Kihou, C. H. Lee, A. Iyo, H. Eisaki, T. Kakeshita, Y. Tomioka, T. Ito, and S. Uchida. Anisotropy of the In-Plane Resistivity of Underdoped $Ba(Fe_{1-x}Co_x)_2As_2$ Superconductors Induced by Impurity Scattering in the Antiferromagnetic Orthorhombic Phase. *Physical Review Letters*, 110, 207001, 2013.

[60] S-H. Baek, D. V. Efremov, J. M. Ok, J. S. Kim, J. van den Brink, and B. Büchner. Orbital-driven nematicity in FeSe. *Nature Materials*, 14, 210–214, 2014.

[61] Q. Wang, Y. Shen, B. Pan, Y. Hao, M. Ma, F. Zhou, P. Steffens, K. Schmalzl, T. R. Forrest, M. Abdel-Hafiez, X. Chen, D. A. Chareev, A. N. Vasiliev, P. Bourges, Y. Sidis, H. Cao, and J. Zhao. Strong interplay between stripe spin fluctuations, nematicity and superconductivity in FeSe. *Nature Materials*, 15, 159–164, 2016.

[62] Q. Wang, Y. Shen, B. Pan, X. Zhang, K. Ikeuchi, K. Iida, A. D. Christianson, H. C. Walker, D. T. Adroja, M. Abdel-Hafiez, X. Chen, D. A. Chareev, A. N. Vasiliev, and J. Zhao. Magnetic ground state of FeSe. *Nature Communications*, 7, 12182, 2016.

[63] F. Wang, S. A. Kivelson, and D.-H. Lee. Nematicity and quantum paramagnetism in FeSe. *Nature Physics*, 11, 959–963, 2015.

[64] J. P. Sun, K. Matsuura, G. Z. Ye, Y. Mizukami, M. Shimozawa, K. Matsubayashi, M. Yamashita, T. Watashige, S. Kasahara, Y. Matsuda, J.-Q. Yan, B. C. Sales, Y. Uwatoko, J.-G. Cheng, and T. Shibauchi. Dome-shaped magnetic order competing with high-temperature superconductivity at high pressures in FeSe. *Nature Communications*, 7, 12146, 2016.

[65] T. Terashima, N. Kikugawa, S. Kasahara, T. Watashige, T. Shibauchi, Y. Matsuda, T. Wolf, A. E. Böhmer, F. Hardy, C. Meingast, H. v. Löhneysen, and S. Uji. Pressure-induced antiferromagnetic transition and phase diagram in FeSe. *Journal of the Physical Society of Japan*, 84, 063701, 2015.

[66] M. D. Watson, T. K. Kim, A. A. Haghighirad, N. R. Davies, A. McCollam, A. Narayanan, S. F. Blake, Y. L. Chen, S. Ghannadzadeh, A. J. Schofield, M. Hoesch, C. Meingast, T. Wolf, and A. I. Coldea. Emergence of the nematic electronic state in FeSe. *Physical Review B*, 91, 155106, 2015.

[67] M. D. Watson, T. K. Kim, L. C. Rhodes, M. Eschrig, M. Hoesch, A. A. Haghighirad, and A. I. Coldea. Evidence for unidirectional nematic bond ordering in FeSe. *Physical Review B*, 94, 201107(R), 2016.

[68] A. I. Coldea and M. D. Watson. The Key Ingredients of the Electronic Structure of FeSe. *Annual Review of Condensed Matter Physics*, 9, 125-146, 2018.

[69] Y. Suzuki, T. Shimojima, T. Sonobe, A. Nakamura, M. Sakano, H. Tsuji, J. Omachi, K. Yoshioka, M. Kuwata-Gonokami, T. Watashige, R. Kobayashi, S. Kasahara, T. Shibauchi, Y. Matsuda, Y. Yamakawa, H. Kontani, and K. Ishizaka. Momentum-dependent sign inversion of orbital order in superconducting FeSe. *Physical Review B*, 92, 205117, 2015.

[70] M. D. Watson, A. A. Haghighirad, L. C. Rhodes, M. Hoesch, and T. K. Kim. Electronic anisotropies revealed by detwinned angle-resolved photoemission spectroscopy measurements of FeSe. *New Journal of Physics*, 19, 103021, 2017.

[71] T. Terashima, N. Kikugawa, A. Kiswandhi, E.-S. Choi, J. S. Brooks, S. Kasahara, T. Watashige, H. Ikeda, T. Shibauchi, Y. Matsuda, T. Wolf, A. E. Böhmer, F. Hardy, C. Meingast, H. v. Löhneysen, M.-T. Suzuki, R. Arita, and S. Uji. Anomalous Fermi surface in FeSe seen by Shubnikov-de Haas oscillation measurements. *Physical Review B*, 90, 144517, 2014.

[72] D. Liu, C. Li, J. Huang, B. Lei, L. Wang, X. Wu, B. Shen, Q. Gao, Y. Zhang, X. Liu, Y. Hu, Y. Xu, A. Liang, J. Liu, P. Ai, L. Zhao, S. He, L. Yu, G. Liu, Y. Mao, X. Dong, X. Jia, F. Zhang, S. Zhang, F. Yang, Z. Wang, Q. Peng, Y. Shi, J. Hu, T. Xiang, X. Chen, Z. Xu, C. Chen, and X.-J. Zhou. Orbital Origin of Extremely Anisotropic Superconducting Gap in Nematic Phase of FeSe Superconductor. *Arxiv Preprint*, 1802.02940, 2018.

[73] Y. S. Kushnirenko, A. V. Fedorov, E. Haubold, S. Thirupathaiah, T. Wolf,

S. Aswartham, I. Morozov, T. K. Kim, B. Büchner, and S. V. Borisenko. 3D superconducting gap in FeSe from ARPES. *Arxiv Preprint*, 1802.08668, 2018.

[74] C. J. Chen. *Introduction to scanning tunneling microscopy*. Oxford series in optical and imaging sciences. Oxford University Press, 1993.

[75] Ø. Fischer, M. Kugler, I. Maggio-Aprile, C. Berthod, and C. Renner. Scanning tunneling spectroscopy of high-temperature superconductors. *Reviews of Modern Physics*, 79, 353–419, 2007.

[76] J. Tersoff and D. R. Hamann. Theory of the scanning tunneling microscope. *Physical Review B*, 31, 805–813, 1985.

[77] J. Bardeen. Tunneling from a many-particle point of view. *Physical Review*, 6, 57–59, 1961.

[78] T. Hanaguri, Y. Kohsaka, J. C. Davis, C. Lupien, M. Yamada, M. Azuma, M. Takano, K. Ohishi, M. Ono, and H. Tagaki. Quasiparticle interference and superconducting gap in $Ca_{2-x}Na_xCuO_2Cl_2$. *Nature Physics*, 3, 865-871, 2007.

[79] K. Fujita, I. Grigorenko, J. Lee, W. Wang, J. X. Zhu, J. C. Davis, H. Eisaki, Uchida S., and A. V Balatsky. Bogoliubov angle and visualization of particle-hole mixture in superconductors. *Physical Review B*, 78, 054510, 2008.

[80] T. Hanaguri, Y. Kohsaka, M. Ono, M. Maltseva, P. Coleman, I. Yamada, M. Azuma, M. Takano, K. Ohishi, and H. Tagaki. Coherence Factors in a High-Tc Cuprate Probed by Quasi-Particle Scattering Off Vortices. *Science*, 323, 5916:923–926, 2009.

[81] M. Maltseva and P. Coleman. Model for nodal quasiparticle scattering in a disordered vortex lattice. *Physical Review B*, 80, 144514, 2009.

[82] R. M. Feenstra. Tunneling spectroscopy of the (110) surface of direct-gap III-IV semiconductors. *Physical Review B*, 50, 4561, 1994.

[83] E. W. Hudson, C. YiLeon, S. Pan, R. W. Simmonds, and J. C. Davis. A very low temperature vibration isolator. *Czechoslovak Journal of Physics*, 46, 2737, 1996.

[84] L. E. Wolf. *Principles of Electron Tunneling Spectroscopy*. Oxford Science Publications. Oxford University Press, 2012.

[85] S. H. Pan, E. W. Hudson, and J. C. Davis. ^{3}*He* Refridgerator Based Very Low Temperature Scanning Tunneling Microscope. *Review of Scientific Instruments*, 46, 2737, 1999.

[86] L. Simon, , Vonau F., and Cranney M. A phenomenological approach of joint density of states for the determination of band structure in the case of a semi-metal studied by FT-STS. *Journal of Physics: Condensed Matter*, 19, 2007.

[87] J. E. Hoffman, K. McElroy, D-H. Lee, K. L Lang, H. Eisaki, S. Uchida, and J. C. Davis. Imaging quasiparticle interference in $Bi_2Sr_2CaCu_2O_{8+\delta}$. *Science*, 297, 2007.

[88] Q. Wang and D-H. Lee. Quasiparticle scattering interference in high temperature superconductors. *Physical Review B*, 67, 020511, 2003.

[89] L. Capriotti, Scalapino D. J., and Sedgewick R. D. Wave-vector power spectrum of the local tunneling density of states: Ripples in a d-wave sea. *Physical Review B*, 68, 014508, 2003.

[90] Lingyin Zhu, W. A. Atkinson, and P. J. Hirschfeld. Power spectrum of many impurities in a d-wave superconductor. *Physical Review B*, 69, 060503, 2004.

[91] N.W. Ashcroft and N.D. Mermin. *Solid State Physics*. Harcourt College Publishers, 1976.

[92] G. D. Mahan. *Many-Particle Physics*. Spring Science+Business Media, LLC, 2000.

[93] A. V. Balatsky, I. Vekhter, and J-X. Zhu. Impurity-induced states in conventional and unconventional superconductors. *Reviews of Modern Physics*, 78, 2006.

[94] L. Simon, Bena C., Vonau F., and Cranney M. Fourier-transform scanning tunneling spectroscopy: the possibility to obtain constant-energy maps and band dispersion using a local measurement. *Journal of Physics D: Applied Physics*, 44, 2011.

[95] Markiewicz R. S. Bringing k and q space in the cuprate: Comparing angle-resolved photoemission and STM results. *Physical Review B*, 69, 2145517, 2004.

[96] P. Roushan, J. Seo, C. V. Parker, Hor Y. S., D. Hsieh, D. Qian, A. Richardella, Z. Hasan, R. J. Cava, and Y. Yazdani. Topological surface states protected from backscattering by chiral spin texture. *Nature*, 460, 1106-1109, 2009.

[97] A. Kreisel, Y. Wang, T. A. Maier, P. J. Hirschfeld, and D. J. Scalapino. Spin fluctuations and superconductivity in $K_xFe_{2-y}Se_2$. *Physical Review B*, 88, 094505, 2013.

[98] I. Lee, C.-K. Kim, J. Lee, S. Billinge, R. Zhong, J. Schneeloch, T. Liu, T. Valla, J. M. Tranquada, G. Gu, and J. C. Davis. Imaging Dirac-mass disorder from magnetic dopant atoms in the ferromagnetic topological insulator $Cr_x(Bi_{0.1}Sb_{0.9})_{2-x}Te_3$. *PNAS*, 112, 1316, 2015.

[99] A. E. Böhmer, V. Taufour, W. E. Straszheim, T. Wolf, and P. C. Canfield. Variation of transition temperatures and residual resistivity ratio in vapor-grown FeSe. *Physical Review B*, 94, 024526, 2016.

[100] U. S. Kaluarachchi, V. Taufour, A. E. Böhmer, M. A. Tanatar, S. L. Bud'ko, V. G. Kogan, R. Prozorov, and P. C. Canfield. Nonmonotonic pressure evolution of the upper critical field in superconducting FeSe. *Physical Review B*, 93, 064503, 2016.

[101] A. Kostin, Sprau. P. O., A. Kreisel, Y. X. Chong, A. E. Böhmer, P. C. Canfield, P. J. Hirschfeld, B. M. Andersen, and J. C. Davis. Visualizing orbital-selective quasiparticle interference in the Hund's Metal State of FeSe. *Arxiv Preprint*, 1802.02266, 2018.

[102] E. Bascones, B. Valenzuela, and M. J. Calderón. Magnetic interactions in iron-based superconductors: A review. *Comptes Rendus Physique*, 17, 36-39, 2016.

[103] R. Yu and Q. Si. U(1) slave-spin theory and its application to Mott transition in a multiorbital model for iron pnictides. *Physical Review B*, 86, 085104, 2012.

[104] J. Kang, R. M. Fernandes, and A. Chubukov. Superconductivity in FeSe: the role of nematic order. *Arxiv Preprint*, 1802.01048, 2018.

[105] L. Fanfarillo, G. Giovannetti, M. Capone, and E. Bascones. Nematicity at the Hund's metal crossover in iron superconductors. *Physical Review B*, 95, 144511, 2017.

[106] R. Yu, J.-X. Zhu, and Q. Si. Orbital selectivity enhanced by nematic order in FeSe. *Arxiv Preprint*, 1803.01733, 2018.

[107] M. J. Lawler, K. Fujita, J. Lee, A. R. Schmidt, Y. Kohsaka, C. K. Kim, H. Eisaki, S Uchida, J. C. Davis, J.P. Sethna, and E.-A. Kim. Intra-unit-cell electronic nematicity of the high-T_c copper-oxide pseudogap states. *Nature*, 466, 347–51, 2010.

[108] A. Mesaros, K. Fujita, H. Eisaki, S. Uchida, J. C. Davis, S. Sachdev, J. Zaanen, M. J. Lawler, and E.-A. Kim. Topological defects coupling smectic modulations to intra-unit cell nematicity in cuprates. *Science*, 333, 426–430, 2011.

[109] A. E. Böhmer, T. Arai, F. Hardy, T. Hattori, T. Iye, T. Wolf, H. v. Löhneysen, K. Ishida, and C. Meingast. Origin of the tetragonal-to-orthorhombic phase transition in FeSe: A combined thermodynamic and NMR study of nematicity. *Physical Review Letters*, 114, 027001, 2015.

[110] T.-M. Chuang, M. P. Allan, J. Lee, Y. Xie, N. Ni, J. C. Bud'ko S. L. Davis, G. S. Boebinger, P. C. Canfield, and J. C. Davis. Nematic Electronic Structure in the "Parent" State of the Iron-Based Superconductor $Ca(Fe_{1-x}Co_x)_2As_2$. *Science*, 327, 181–184, 2010.

[111] A. R. Schmidt, M. H. Hamidian, P. Wahl, F. Meier, A. V. Balatsky, J. D. Garrett, T. J. Williams, G. M Luke, and J. C. Davis. Imaging the Fano lattice to "hidden order" transition in URu_2Si_2. *Nature*, 465, 570–576, 2010.

[112] A. Kreisel, P. Choubey, T. Berlijn, W. Ku, B. M. Andersen, and P. J. Hirschfeld. Interpretation of Scanning Tunneling Quasiparticle Interference and Impurity States in Cuprates. *Physics Review Letters*, 114, 217002, 2015.

[113] E. Torre, Y. He, and E. Demmler. Holographic maps of quasiparticle interference. *Nature Physics*, 12, 1052-1056, 2016.

[114] C.-L. Song, Y.-L. Wang, Y.-P. Jiang, L. Wang, K. He, X. Chen, J. E. Hoffman, X.-C. Ma, and Q.-K. Xue. Suppression of superconductivity by twin boundaries in FeSe. *Physical Review Letters*, 109, 137004, 2012.

[115] B. M. Uranga, M. N. Gastiasoro, and B. M. Andersen. Electronic vortex structure of Fe-based superconductors: Application to LiFeAs. *Physical Review B*, 93, 224503, 2016.